UNIVERSITY OF CALIFORNIA
Santa Barbara

Experimental and Computational Investigations of Organic and Hybrid Solar Cells

A dissertation submitted in partial satisfaction
of the requirements for the degree of

Doctor of Philosophy

in

Materials

by

Nancy D. Eisenmenger

Committee in Charge:

Professor Michael L. Chabinyc, Chair

Professor Glenn H. Fredrickson

Professor Edward J. Kramer

Professor Craig J. Hawker

December 2014

The dissertation of
Nancy D. Eisenmenger is approved:

Professor Glenn H. Fredrickson

Professor Edward J. Kramer

Professor Craig J. Hawker

Professor Michael L. Chabinyc, Committee Chairperson

September 2014

Experimental and Computational Investigations of Organic and Hybrid Solar Cells

by

Nancy D. Eisenmenger

Acknowledgements

I am grateful to my husband, Hendrik, for his support, willingness to navigate our relationship through graduate programs halfway across the country from each other, and occasional help on math-related research. I thank my parents for their encouragement and of course, whatever they did right with parenting to get me this far. I hope I made you proud! I also thank my sister for her frequent visits to sunny Santa Barbara and the outdoor adventures she dragged me on when I needed a break.

I thank my labmates and friends in Santa Barbara, especially Dr. Christopher Liman and his entropy-aura (a.k.a The Liman Effect).

Many thanks to Professor Michael Chabinyc for years of advice and support above and beyond all expectations, and to Professor Glenn Fredrickson in the ChemE department and Professor Venkat Ganesan at UT Austin for welcoming me into their research groups and the world of computational materials.

Curriculum Vitæ

Nancy D. Eisenmenger

Education

2009	Bachelor of Science in Chemistry, Harvey Mudd College.

Experience

2009 – 2014	Graduate Research Assistant, University of California, Santa Barbara.
Winter 2012	Teaching Assistant for Electronic & Atomic Structure of Materials (Materials 200B), University of California, Santa Barbara.
2010 and 2013	Mentor for Summer Interns, University of California, Santa Barbara.
2009 – 2014	ScienceLine Responder for MRL Science Outreach Program, University of California, Santa Barbara.

Awards

2009	National Science Foundation Graduate Research Fellowship
2009	Chancellor's Fellowship, UC Santa Barbara Graduate Fellowship
2011	Outstanding ScienceLine Responder (Dow-MRL Outreach Award)

Selected Publications

- **N. D. Eisenmenger**, K. Delaney, M. L. Chabinyc, V. Ganesan, G. H. Fredrickson. **(2014)** "Improving Relay Dyes for Dye Sensitized Solar Cells by Increasing Donor Homotransfer." *J. Phys. Chem. C.* doi:10.1021/jp5014225

- G. M. Su, T. V. Pho, **N. D. Eisenmenger**, C. Wang, F. Wudl, E. J. Kramer, M. L. Chabinyc. **(2013)** "Linking morphology and performance of organic solar cells based on decacyclene triimide acceptors" *J. Mater. Chem. A*, 2, 1781-1789. doi:10.1039/C3TA14839D

- T. V. Pho, F. M. Toma, B. J. Tremolet de Villers, S. Wang, N. D. Treat, **N. D. Eisenmenger**, G. M. Su, R. C. Coffin, J. D. Douglas, J. M. J. Frechet, G. C. Bazan, F. Wudl, M. L. Chabinyc. **(2013)** "Decacyclene Triimides: Paving the Road to Universal Non-Fullerene Acceptors for Organic Photovoltaics." *Adv. Ener. Mater.*, doi:10.1002/aenm.201301007

- M. J. Robb, D. J. Montarnal, **N. D. Eisenmenger**, S. Y. Ku, M. L. Chabinyc, C. J. Hawker. **(2013)** "A One-Step Strategy for End-Functionalized Donor-Acceptor Conjugated Polymers." *Macromolecules*, 46, 6431-6438. doi:10.1021/ma401255d

- **N. D. Eisenmenger**, G. M. Su, G. C. Welch, C. J. Takacs, G. C. Bazan, E. J. Kramer, and M. L. Chabinyc **(2013)**. "Effect of Bridging Atom Identity on the Morphological Behavior of Solution-Processed Small Molecule Bulk Heterojunction Photovoltaics." *Chem. Mater.*, 25, 1688-1698. doi:10.1021/cm4001416

- R. F. Roskamp, I. K. Vockenroth, **N. D. Eisenmenger**, J. Braunagel, and I. Köper **(2008)**. "Functional Tethered Bilayer Lipid Membranes on Aluminum Oxide." *ChemPhysChem.*, 9, 1920-1924. doi:10.1002/cphc.200800248

Fields of Study

Major Field: Organic Electronics

- Studies in Organic Solar Cells with Professors Chabinyc and Hawker
- Studies in Modeling Excited State Transport with Professors Chabinyc, Fredrickson, and Ganesan

Abstract

Experimental and Computational Investigations of Organic and Hybrid Solar Cells

Nancy D. Eisenmenger

Organic and hybrid solar cells are complex, nanostructured devices, for which an in-depth understanding is required to improve and optimize. Both types of solar cells take advantage of the strong optical absorption of organic chromophores to collect sunlight and have reached maximum efficiencies of around 12% as of the end of 2014. They both also rely on nanostructures and interfaces to balance energy and charge transport. Despite these underlying similarities, organic solar cells and dye sensitized solar cells present different challenges to optimization. We have applied experimental and computational techniques to help explore and understand factors that affect their efficiencies and describe and predict strategies for improving them. We made a comparative study of two isostructural donor molecules and studied the exciton and charge transport in a non-fullerene acceptor molecule in bulk heterojunction organic solar cells. We then wrote a kinetic Monte Carlo simulation to study energy transfer in donor-acceptor systems and applied it to study trapping kinetics in different morphologies, energy relay dyes in dye sensitized solar cells, and energy cascades in bilayer organic solar cells. Based on these simulations, we offer design suggestions for both types of solar cells.

Contents

List of Figures

List of Tables

Chapter 1

Introduction

1.1 Organic Photovoltaics

Organic solar cells were created by Tang nearly 30 years, and the efficiency has made remarkable improvements from 1%[1] to almost 12%[2] since then. These solar cells are composed of two phases made up of a donor material and an acceptor material. Each phase can be either a small molecule/oligomer or a polymer. Materials selection is governed by the interplay of many criteria, including spectral coverage (material bandgap), relative HOMO and LUMO energy level offsets, electron and hole mobility, solubility, and high purity (low trap concentrations).[3,4] In addition, once these criteria are met, the morphology of the resulting film is extremely important. Devices with bulk heterojunction morphologies, where the donor and acceptor materials are intimately mixed with phase separate on a small scale, show high performance, but it is often difficult of obtain the desired mor-

phology. This difficulty is a crippling problem for most organic solar cells: their success relies on finding a processing procedure that results in a kinetically trapped morphology that has the appropriate phase separation and domain sizes. Optimizing processing techniques is time consuming and requires varying donor/acceptor ratios, spincoating and bladecoating parameters, solvents and co-solvents, and controlled drying and thermal annealing.[5,6]

Much is already known about designing a successful morphology. The main design criteria are summarized here:[7]

1. **Exciton Diffusion.** The domains must be about the same size as the exciton diffusion length, L_D. If the domains are too large, then excitons generated within the interior will relax to the ground state before they reach an interface. L_D is material dependent, as it is a function of the exciton lifetime and diffusion constant, $L_D = (D\tau)^{1/2}$, but is generally $\sim$10 nm.

2. **Exciton Dissociation.** The domain interfaces must have substantial surface area in order to facilitate exciton dissociation. Excitons in organics can only overcome their binding energy with the help of the electric field from the donor-acceptor energy level offset so charge generation can only occur at the interfaces. Increasing the probability of exciton dissociation necessitates large interfacial area.

3. **Charge Transport.** The domains must be interconnected and have direct pathways to the electrodes for efficient charge transport. The more tortuous the pathways, the more time the charges will have to be trapped and recombine before they are collected. Islands of donor or acceptor not connected to the electrode or *cul-de-sacs* in the direction of the applied electric field will lead to greater recombination.

Criteria (1) and (2) are best met by a well mixed bulk-heterojunction-type system, but criterion (3) is best met by a bilayer structure. To have an efficient device, a structure must be found that satisfies and balances all three requirements. Using design strategies to overcome one or more of these limitations could help improve organic solar cell efficiencies. For instance using an energy transfer cascade structure can facilitate the movement of excitons, allowing for the use of a bilayer-type structure which is good for charge transport.

1.2 Dye Sensitized Solar Cells

Dye sensitized solar cells were first made in 1991 by O'Reagan and Graetzel with a remarkable efficiency of 7%.[8] Since then they have increased to 12% in efficiency.[2,9] These solar cells are composed of a sensitizing dye, which absorbs sunlight, a nanoporous titania film to which the sensitizing dye molecules are

adsorbed, and an electrolyte - usually a redox couple in liquid solution that fills the nanopores. The sensitizing dye molecules are usually large transition metal complexes or conjugated molecules that absorb broadly across the solar spectrum. They are functionalized with solubilizing groups which allow them to be applied to the titania in solution and some type of acid group which allows them to attach strongly to the titania. The nanoporous titania is a semiconductor which transports electrons from the dyes to the cathode while the electrolyte regenerates the dye molecules that have already injected electrons into the titania. The titania needs to be nanoporous (particles are about 20 nm in diameter) so there is a high surface area where dyes can be attached.

There are currently several limitations in the field of dye sensitized solar cells. First, the liquid electrolyte makes device stability and encapsulation difficult. Solid-state hole transporting materials are available and can be used instead, but lead to lower efficiencies, mostly due to incomplete filling of the nanopores.[10] Another limitation is the absorption of the dye, which needs to absorb strongly from the ultra-violet to the near infrared; unfortunately there is a tradeoff between the oscillator strength of a chromophore and the width of absorption. Dyes with low extinction coefficients mean solar cells must be thicker, which can cause issues with transport. An alternative to using broadly absorbing dyes is to use multiple dyes with complementary absorption. Co-sensitizing is indeed an effective design,

leading to some of the most efficient DSCs.[10] However, further progress with this technique is limited due to the surface area of the nanoporous titania - multiple dyes must compete for a surface on which to adsorb. One way to overcome this problem is to dissolve the second, complementary dye in solution rather than adsorb it to the titania. Then the issue becomes injecting an electron from the second dye which is no longer in close proximity to the titania interface. This can be done by transporting the excited state from the dye in solution to the sensitizing dye via Förster energy transfer. This energy relay dye strategy has been pursued experimentally, but has not yet led to highly efficient DSCs.[11–16]

1.3 Kinetic Monte Carlo Simulations and Energy Transfer

Kinetic Monte Carlo (KMC) simulations can be used to simulate the time-dependent behavior of a system, provided the rates are known for all possible events. The probability of an event occurring in the simulation is proportional to its rate. This type of simulation proves to be quite useful for studying Förster energy transfer because the energy transfer rate can be calculated from the Förster transfer radius and the distance between the molecules. Thus KMC simulations are useful for studying exciton diffusion within one material which occurs by

energy homotransfer as well as exciton movement via Förster transfer from one material to another. As mentioned above, energy transfer is relevant to energy relay dyes in dye sensitized solar cell and to energy transfer cascades in organic photovoltaics. We take advantage of a KMC simulation framework to study both types of solar cells.

1.4 Overview

Chapter 2 discusses a suite of experiments exploring isostructural donor molecules. We investigated why one of the molecules performs well in organic solar cells and a nearly identical molecule does not. We found that although the changing a single atom from carbon to silicon in the structure of the molecule does not significantly affect electronic and optical properties, it does affect thermal properties of the molecules and thus their morphology in the film and how they behave upon annealing. **Appendix A** contains supporting information for this chapter.

Chapter 3 discusses the non-fullerene acceptor molecule, DTI, and photoluminescence studies that that support a mechanism that explains why DTI performs poorly in annealed bulk heterojunction organic solar cells.

Chapter 4 reports the results from kinetic Monte Carlo simulations of energy transfer in different donor acceptor geometries and classifies the trapping kinetics based on morphological parameters. We found that the trapping appears to be controlled by the surface area to volume ratio of the donor domains.

Chapter 5 discusses energy relay dye strategies for dye sensitized solar cells. We used our kinetic Monte Carlo simulations to show that energy relay dyes with strong energy self-transfer can increase the exciton transfer efficiency to the sensitizing dye. We proposed guidelines for a universal energy relay dye.

Chapter 6 discusses strategies for bilayer organic solar cells using energy cascade designs. We evaluated several types of energy cascades and device architectures and made suggestions for designing bilayer solar cells with energy cascades. **Appendix B** contains supporting information for this chapter.

Chapter 2

Effect of Bridging Atom Identity on the Morphological Behavior of Solution-Processed Small Molecule Bulk Heterojunction Photovoltaics

2.1 Introduction

Organic photovoltaics (OPVs) are alternative materials systems to amorphous silicon, CdTe, and CIGS for thin film solar cells.[17] The highest power conversion efficiencies (PCEs) of lab-scale (area $\sim< 0.2$ cm^2) OPVs have been typically obtained with solution-processed polymer:fullerene-based bulk heterojunction (BHJ) devices,[18,19] which have PCEs up to 9.2%.[20] Advances in the performance of BHJ solar cells with solution-processable small molecules[21–31] have led to PCEs up to 7.2%.[32] Photovoltaics with small molecule based active layers possess several po-

tential advantages over polymer systems. Compared to polymers, small molecules do not suffer from the effects of polydispersity, tend to have less batch-to-batch variation, and are easily functionalized and purified via standard techniques.[33]

Several classes of donor small molecules have been successfully utilized in BHJ solar cells, including squaraine dyes,[34–36] diketopyrrolopyrrole based molecules,[25,37] and oligothiophenes.[27,38–40] Due to their ability to crystallize, the morphological characteristics that lead to high PCE may differ from polymers. Here we report here on the characterization of the morphology and optoelectronic characteristics of two low-band gap solution-processable small molecule donors and their use in BHJs with [6,6]-phenyl C_{71}-butyric acid methyl ester ($PC_{71}BM$).

It is well-known that device performance of both polymeric and small molecule BHJs depends critically on the complex three-dimensional morphology of the active layer.[5,41–44] Polymer based BHJs comprise a multiphase blend of pure donor and acceptor and an impure amorphous region.[43,45] Small molecules are likely to crystallize into pure domains, but mixed amorphous domains may also be present. Studies have shown that both vapor and solution-based deposition of small molecules can lead to efficient multilayer or BHJ devices,[21,22,26,44,46–51] suggesting the importance of the final film microstructure, rather than fabrication techniques, on device performance.[52] Because the mobility of charge carriers depends on molecular ordering, and hence degree of crystallinity,[53] small molecules

may have the advantage of higher charge carrier mobilities. Despite recent efforts to characterize the morphology in small molecule BHJs[25,28] knowledge regarding these systems is still lacking.

Here, we investigate two isostructural small molecules, 5,5'-bis7-(4-(5-hexylthiophen-2-yl)thiophen-2-yl)-[1,2,5]-thiadiazolo[3,4-c]pyridine-3,3'-di-2-ethylhexylsilylene-2,2'-bithiophene, (*d*-DTS($PTTh_2$)$_2$) and its carbon-bridged analog (*d*-CDT($PTTh_2$)$_2$), compounds that are based on an electron acceptor/donor/acceptor core with end-capping donor units (Figure 2.1).[54] Changing the identity of the bridging atom from silicon to carbon results in significantly different morphological behavior and PCE. Note that *d*-CDT($PTTh_2$)$_2$[55] is an isomer of *d*-DTS($PTTh_2$)$_2$, which is currently one of the highest-performing donors in BHJs.[23] The effect of bridging atom identity, specifically the difference between carbon and silicon, is already known in polymer based systems. For example, the low bandgap polymer, poly[4,4-bis(2-ethylhexyl)-cyclopenta-(2,1-b;3,4-b')dithiophene]-2,6-diyl-alt-(2,1,3-benzothiadiazole)-4,7-diyl (PCPDTBT), performs well in as-cast BHJs with $PC_{71}BM$.[56] Its silole-containing analog, poly[4,40-bis(2-ethylhexyl)dithieno (3,2-b;20,30-d)silole]-2,6-diyl-alt-(2,1,3-benzothidiazole)-4,7-diyl (PSBTBT), performs comparably in as-cast devices, but unlike PCPDTBT its performance can be increased substantially with thermal annealing.[57]

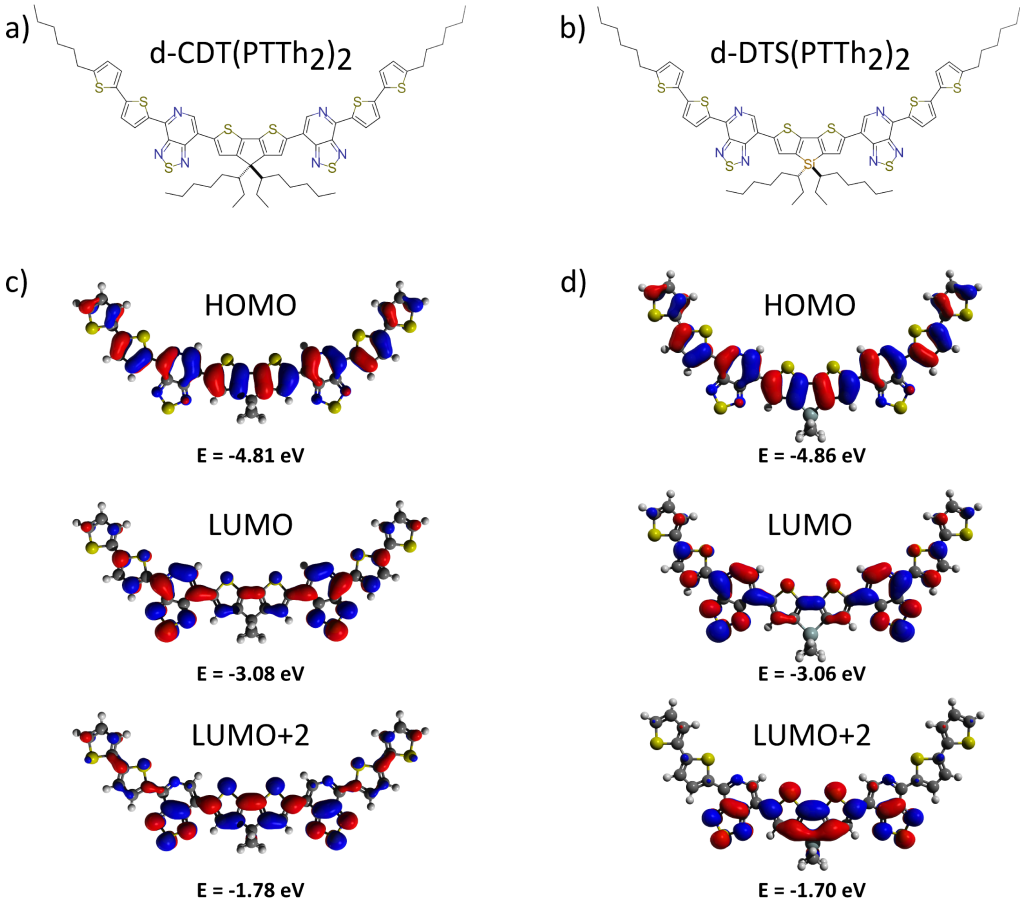

Figure 2.1: The molecular structures of (a) *d*-CDT($PTTh_2$)$_2$ and (b) *d*-DTS-($PTTh_2$)$_2$. They differ by only one atom. One-electron ground state wave functions and calculated orbital energy eigenvalues, E, for the (c) *d*-CDT($PTTh_2$)$_2$ and (d) *d*-DTS($PTTh_2$)$_2$, showing the HOMO, LUMO, and LUMO+2.

To date, the effect of bridging atom identity in small molecule BHJs has not been thoroughly explored. We employ several techniques, including grazing incidence wide-angle X-ray scattering (GIWAXS), transmission electron microscopy (TEM), UV-visible spectroscopy, optical microscopy, and *in situ* current-voltage measurements to elucidate the morphological evolution in *d*-DTS($PTTh_2$)$_2$:-$PC_{71}BM$ and *d*-CDT($PTTh_2$)$_2$:$PC_{71}BM$ BHJs and shed light onto reasons for the difference in photovoltaic performance.

2.2 Experimental

d-DTS($PTTh_2$)$_2$ was synthesized as previously reported,[55] and *d*-CDT-($PTTh_2$)$_2$ was prepared analogously. Devices were fabricated with the glass/ITO (140 nm)/MoO_x (10 nm)/small molecule:$PC_{71}BM$ (3:2 by mass)/Al (90 nm) architecture with a spin-coated active layer and thermally evaporated MoO_x and Al layers. Samples for spectroscopy and X-ray diffraction were identical sans the Al cathode. Blend samples for all measurements contained the same ratio by mass as the films for devices. See the Supporting Information for a detailed description of the synthesis, device fabrication, and measurement techniques used. Calculations for geometry optimization and orbitals were done with

Gaussian 03at the RB3LYP//6-31G(d) level of theory. Orbital were plotted in Avogadro.MarvinSketch was used for drawing structures.

2.3 Results and Discussion

2.3.1 Electrical, Optical, and Thermal Properties.

Despite their similar structures, devices made without solvent additives with *d*-DTS($PTTh_2$)$_2$ have PCEs up to 3.4%, while *d*-CDT($PTTh_2$)$_2$ devices did not attain PCE over 1% *vide infra*. In order to understand the difference in photovoltaic performance between *d*-DTS($PTTh_2$)$_2$ and *d*-CDT($PTTh_2$)$_2$ based devices, it is important to first compare the optical, thermal, and electronic properties of the two compounds. We find that while their electronic properties are similar, their thermal behavior differs substantially.

Electronic Structure.

The energies of the highest occupied molecular orbital (HOMO) and lowest unoccupied molecular orbital (LUMO) of *d*-DTS($PTTh_2$)$_2$ and *d*-CDT($PTTh_2$)$_2$, which were determined by the onsets of the oxidation and reduction peaks in cyclic voltammetry experiments (Supporting Information Figure S1), match closely (Table 2.1).[23] The similarity of the electronic energy levels suggest that there are no

large differences in electronic structure between the two molecules in solution and the maximum attainable open-circuit voltages (V OC) in solar cells should be similar. In related compounds, substitution of silicon for carbon in the bridgehead of the cyclopentadithiophene (CPDT) group in polymers, e.g. PCPDTBT and PSBTBT, also has little effect on the electronic levels.[58,59] Based on DFT calculations, HOMOs for both compounds are well delocalized across the molecular backbone, but the electron density of the LUMOs are moderately localized on the acceptor units (Figure 2.1).

material	HOMO (eV)	LUMO (eV)	abs peak solution (nm (eV))	abs peak (lowest energy) film (nm (eV))	abs edge solution (nm (eV))	abs edge film (nm (eV))	shift in abs edge (eV)
d-CDT($PTTh_2$)$_2$	5.1	3.5	645 (1.9)	747 (1.66)	755 (1.64)	821 (1.51)	0.13
d-DTS($PTTh_2$)$_2$	5.2	3.6	620 (2.0)	715 (1.73)	725 (1.71)	770 (1.61)	0.10
$PC_{71}BM$	5.9	4.2	-	-	-	-	-

Table 2.1: Electronic and Optical Properties of *d*-CDT($PTTh_2$)$_2$ and *d*-DTS($PTTh_2$)$_2$ and Energy Levels of $PC_{71}BM$.

UV-Visible Absorption.

The UV-visible optical absorption spectra of *d*-DTS($PTTh_2$)$_2$ and *d*-CDT-($PTTh_2$)$_2$ are qualitatively similar and exhibit two main features (Supporting Information Figure S2) in chloroform solution. The lowest energy band, seen as a broad, featureless peak from about 500 to 750 nm, is present for both compounds. For *d*-DTS($PTTh_2$)$_2$, the peak wavelength, λ_{max}, of this lowest energy feature occurs at 620 nm, or 2.0 eV and for *d*-CDT($PTTh_2$)$_2$the peak is shifted lower in energy to λ_{max} = 645 nm, or about 1.9 eV. The lower intensity, higher energy peak occurs at 390 nm (3.19 eV) for both molecules.

Calculated absorption spectra for *d*-DTS($PTTh_2$)$_2$ and *d*-CDT($PTTh_2$)$_2$, based on time-dependent density functional theory (TDDFT),[60] show that the absorption spectra are characterized by one dominant, low-energy transition with large oscillator strength and a higher-energy transition with lower oscillator strength. The first ten excited states for each molecule are described in the Supporting Information Tables S1 and S2. For both molecules, the lower energy peak can be attributed to a singlet excited-state (S 0 $\rightarrow$ S 1) HOMO $\rightarrow$ LUMO transition from a highly delocalized HOMO to a LUMO with increased contribution from the electron accepting moieties of the molecule (transition dipole along the long axis of the molecule). For *d*-CDT($PTTh_2$)$_2$, the second, higher-energy band is a transition from the HOMO $\rightarrow$ LUMO+2 (excited state 7). For *d*-DTS-

$(PTTh_2)_2$, the second band is also mainly from the HOMO $\rightarrow$ LUMO+2 transition, with a small contribution from the HOMO-2 $\rightarrow$ LUMO transition (excited state 6). The transitions in both compounds correspond to an orbital localized on the central acceptor/donor/acceptor core of the molecule (transition dipole is also along the long axis of the molecule).

Aggregation into solid-state thin films causes pronounced changes in the experimental absorption spectra (Supporting Information Figure S3) of both compounds and suggests differences in molecular packing. The absorption edges (Table 2.1) of the UV-vis spectra for *d*-DTS$(PTTh_2)_2$ and *d*-CDT$(PTTh_2)_2$ red shift by about 0.10 and 0.13 eV, respectively. The red-shift can be partially attributed to an effective increase in conjugation length due to increased planarity.[61] In the solid-state the low energy band comprises a series of peaks with an energetic splitting of about 0.16 eV, typical of coupling of the electronic excitation with C-C vibronic stretching modes.[59] The lowest energy feature in this band is frequently attributed to $\pi - \pi$ intermolecular interactions of adjacent molecules that occur in the solid-state.[58,61] For both compounds, these peaks can be fit to a Huang-Rhys progression if the lowest energy peak is excluded (Figure 2.2).

The parameter, S, for the fit is larger (1.87 vs 1.47) for *d*-CDT$(PTTh_2)_2$, suggesting greater geometric change upon absorbance relative to *d*-DTS$(PTTh_2)_2$. The lowest energy peak is likely due to a different population of molecules in the

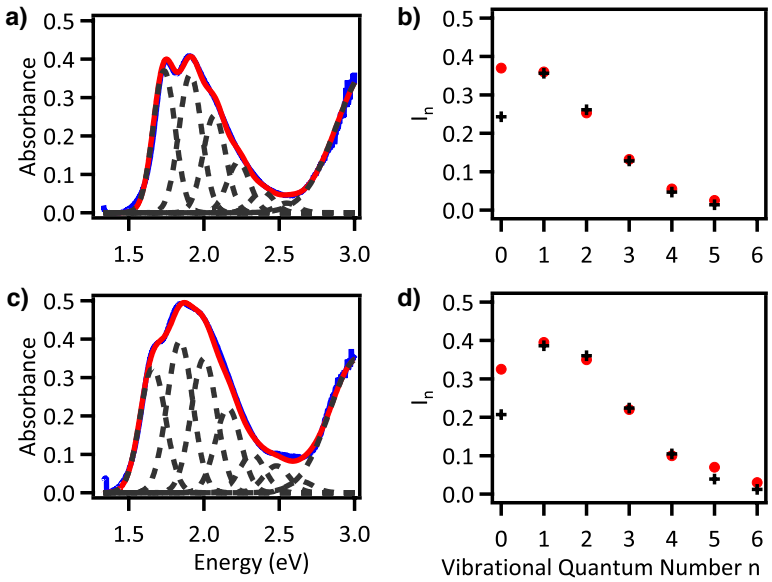

Figure 2.2: UV-vis absorbance of *d*-DTS(PTTh$_2$)$_2$ (a) and *d*-CDT(PTTh$_2$)$_2$ (c) films (in blue) fit with a Huang-Rhys progression (in black and red). The Huang-Rhys intensities are shown for *d*-DTS(PTTh$_2$)$_2$ (b) and *d*-CDT(PTTh$_2$)$_2$ (d), with Huang-Rhys parameter S = 1.47 and 1.87, respectively, suggesting that *d*-CDT-(PTTh$_2$)$_2$ undergoes a larger geometric change with absorption. The red dots show the experimental data and the black crosses show the fit to the Huang-Rhys equation. In each case, the intensity of the lowest energy Gaussian does not fit the progression. The spacing between the Gaussian peaks that obey the Huang-Rhys progression in the ft is 0.16 eV for both *d*-DTS(PTTh$_2$)$_2$ and *d*-CDT(PTTh$_2$)$_2$.

crystal. In the solid-state, the lowest-energy peak in the main absorption band is centered at 715 nm (1.73 eV) for *d*-DTS(PTTh$_2$)$_2$ and 747 nm (1.66 eV) for *d*-CDT(PTTh$_2$)$_2$, and it is more pronounced in *d*-DTS(PTTh$_2$)$_2$. This observation suggests the two compounds have a different molecular packing geometry. As seen for derivatives of sexithiophene,[61] if the transition dipoles are parallel (molecules aligned), then the transition between the ground state and lower crys-

talline excited state is forbidden, leading to the observed single, dominant peak, or suppressed low-energy features. It is possible this type of transition dipole coupling is occurring more in *d*-CDT($PTTh_2$)$_2$compared to *d*-DTS($PTTh_2$)$_2$, but without single crystal structures it is difficult to assign the origin unambiguously. The absorption maximum of the high energy feature (for *d*-DTS($PTTh_2$)$_2$) does not shift noticeably between solution and thin film.[55]

The UV-vis spectra of the BHJ active layers show a reduction in overall intensity compared to pristine films. In addition, in both *d*-DTS($PTTh_2$)$_2$:$PC_{71}BM$ and *d*-CDT($PTTh_2$)$_2$:$PC_{71}BM$blends, the lowest energy peak becomes weaker relative to other features, suggesting that $PC_{71}BM$disrupts molecular ordering. Despite the better performance of *d*-DTS($PTTh_2$)$_2$ based devices (vida infra), the absorption of the *d*-CDT($PTTh_2$)$_2$ active layer extends farther into the near-infrared (NIR), which, based on integrating the absorbance against the solar spectrum (assuming the same thicknesses and 100% IQE), could result in photocurrent up to 20% greater than *d*-DTS($PTTh_2$)$_2$.

Differential Scanning Calorimetry.

The substitution of a silicon bridging-atom has a much stronger impact on the thermal properties than on the electronic structure. The thermal transitions of *d*-DTS($PTTh_2$)$_2$ and *d*-CDT($PTTh_2$)$_2$ in the bulk were characterized with dif-

ferential scanning calorimetry (DSC) and are shown in Figure 2.3. The melting and crystallization temperatures increase for *d*-DTS($PTTh_2$)$_2$ relative to *d*-CDT-($PTTh_2$)$_2$. The main melting endotherm occurs at $\sim$ 220°C for *d*-DTS($PTTh_2$)$_2$ but only $\sim$ 145°C for *d*-CDT($PTTh_2$)$_2$. The melting temperatures of organic crystals[62] are determined by factors including molecular symmetry, electric dipoles, interaction energies, and entropy.[63–65] Considering the similar molecular structures of the two compounds, it is possible that the higher melting temperature is evidence of stronger intermolecular interactions between *d*-DTS($PTTh_2$)$_2$ molecules compared to *d*-CDT($PTTh_2$)$_2$ molecules. The bridgehead bonds at silicon in *d*-DTS($PTTh_2$)$_2$ are longer than those at the carbon bridgehead in *d*-CDT($PTTh_2$)$_2$ which may reduce steric interactions between adjacent molecules allowing closer approach as has been noted for similar model compounds,[58] but without known crystal structures, this cause cannot be confirmed experimentally. The Huang-Rhys fitting and diffraction data (*vide infra*) suggest different molecular packing in the compounds' crystal structures which makes direct comparison of intermolecular interactions problematic and contributes to the large difference we see in the melting point. In addition, *d*-DTS($PTTh_2$)$_2$ has a second, smaller endothermic peak that occurs at around 110°C, which does not appear in *d*-CDT($PTTh_2$)$_2$ samples. Upon cooling, *d*-DTS($PTTh_2$)$_2$ exhibits a major crystallization exotherm at $\sim$ 185° C and a more subtle exothermic peak at around 90°C. The smaller en-

dothermic and exothermic peaks at 110 and 90°C, respectively, are likely due to a solid-solid phase transition between different polymorphs or melting and crystallization of the ethylhexyl side chains.[65] In contrast, when *d*-CDT(PTTh$_2$)$_2$ is heated, a large exothermic peak occurs at around 90°C just before the melting endothermic peak at 145°C, possibly a result of cold crystallization of amorphous molecules before melting. On cooling, no major crystallization peak is seen, unlike in *d*-DTS(PTTh$_2$)$_2$. In addition, the subtle baseline shift that occurs around 50°C is indicative of a glass transition.

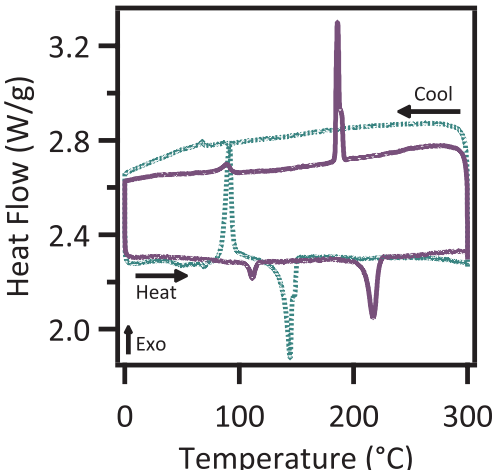

Figure 2.3: DSC traces of *d*-DTS(PTTh$_2$)$_2$ (purple) and *d*-CDT(PTTh$_2$)$_2$ (dotted green). The heating and cooling rate was 2° C/min.

In addition to the DSC data for the neat compounds, the thermal behavior of the blends with PC$_{71}$BM can aid in developing and understanding processing conditions for solar cells. When *d*-DTS(PTTh$_2$)$_2$is blended with PC$_{71}$BM,

the melting temperature is reduced to 195°C, the crystallization temperature to 145°C, and the smaller, more subtle melting and crystallization peaks are no longer present. The *d*-CDT($PTTh_2$)$_2$:$PC_{71}BM$ blend exhibits the same features as the pure material, but the melting temperature decreases to 135° and the cold crystallization peak occurs at 115°C. The DSC traces of the blends are shown in Supporting Information Figure S6.

2.3.2 Morphology of Donors and BHJs.

Grazing Incidence Wide-Angle X-ray Scattering (GIWAXS).

GIWAXS is a powerful technique to characterize molecular order in thin films of semiconducting polymers[66–70] and small molecules.[71,72] Here, we use GIWAXS to determine differences in ordering and orientation in as-cast and annealed films of the small molecules and their blends with $PC_{71}BM$. A previous GIWAXS study of films of *d*-DTS($PTTh_2$)$_2$ and their BHJs with $PC_{71}BM$ cast onto a silicon wafer coated with a polymeric hole injection layer (Plextronics Plexcore OC AQ-1300) showed increasing crystallinity with thermal annealing for both neat films and BHJs but relatively little crystalline order in as-cast BHJs.[55] For comparison, we examined films on glass/ITO/MoO_x substrates processed under different thermal conditions, similar to those used to obtain the highest PCEs in the OPVs

found here, and we focus on blend films with $PC_{71}BM$ that are relevant to device architecture.

Pristine *d*-DTS($PTTh_2$)$_2$ and *d*-CDT($PTTh_2$)$_2$ Films. Two-dimensional GIWAXS patterns of as-cast and annealed *d*-DTS($PTTh_2$)$_2$ and *d*-CDT($PTTh_2$)$_2$ films are provided in the Supporting Information Figure S8. GIWAXS data on as-cast and annealed *d*-DTS($PTTh_2$)$_2$ films reveal d-spacings of the major in-plane and out-of-plane peaks similar to those previously reported by Welch et al.[55] The most intense reflection for *d*-CDT($PTTh_2$)$_2$ reveals a d-spacing of 16.0 Å, less than the 19.1 Åfor *d*-DTS($PTTh_2$)$_2$. Annealing of pristine films tends to increase crystallite correlation length of the ordered domains. These effects are detailed in the Supporting Information.

***d*-DTS($PTTh_2$)$_2$:$PC_{71}BM$.** The scattering from the as-cast *d*-DTS-($PTTh_2$)$_2$:$PC_{71}BM$ blend film (Figure 2.4a) shows similar characteristics to the neat film. Prominent textured features are found at $q_z = 0.34$ Å^{-1}(18.6 Å) and at $q_{xy} = 1.80$ Å^{-1} (3.5 Å) along with a diffuse ring from aggregated $PC_{71}BM$at 1.34 Å^{-1}. Because the bulk single crystal structure of *d*-DTS($PTTh_2$)$_2$ is not known, the assignment of these features is based on a qualitative assessment of molecular models. The reflection at $q_z = 0.34$ Å^{-1} was previously attributed to stacking along the 2-ethylhexyl side chains.[55] Considering the conformation shown in Figure 2.1, half of the length along the conjugated core is relatively similar to the

"height" of the molecule along the 2-ethylhexyl extent, so it is difficult to directly assign this reflection to a molecular direction. The full assignment of a unit cell is beyond the scope of this paper; therefore, we will use the convention of the previous publication[55] and refer to the peak at $q_z = 0.34$ Å^{-1} as the(100) reflection, and the $q_{xy} = 1.8$Å^{-1} as the (010) reflection. Peaks directly along q_z are in the inaccessible region of the Ewald sphere in grazing incidence geometry,[70,73] and it is of interest to note that the in-plane portion of the (100) peak has a d-spacing of about 20.4 Å. This could be a result of the presence of different polymorphs or varying amounts of shrinkage in the out-of-plane vs in-plane directions.

The scattering data reveal the orientation and quality of ordering in the crystalline domains. A sector plot of the as-cast *d*-DTS(PTTh$_2$)$_2$:PC$_{71}$BM film (Supporting Information Figure S9) shows that both the (100) and the (010) reflections have a broad angular distribution but with a dominant texture such that the a* axis is aligned nearly along q_z, where the polar angle is defined to be 0°. Assuming the notation described above, this texture would be consistent with an edge-on orientation of the conjugated core relative to the substrate, which is common for many molecular organic semiconductors.[45,55,74] The crystallite correlation length is about 25 nm (Supporting Information Table S3) estimated with the Scherrer equation and the full-width-at-half-maximum (fwhm) of the scattering peaks.[75] It is important to note that Scherrer analysis assumes that only crystallite size

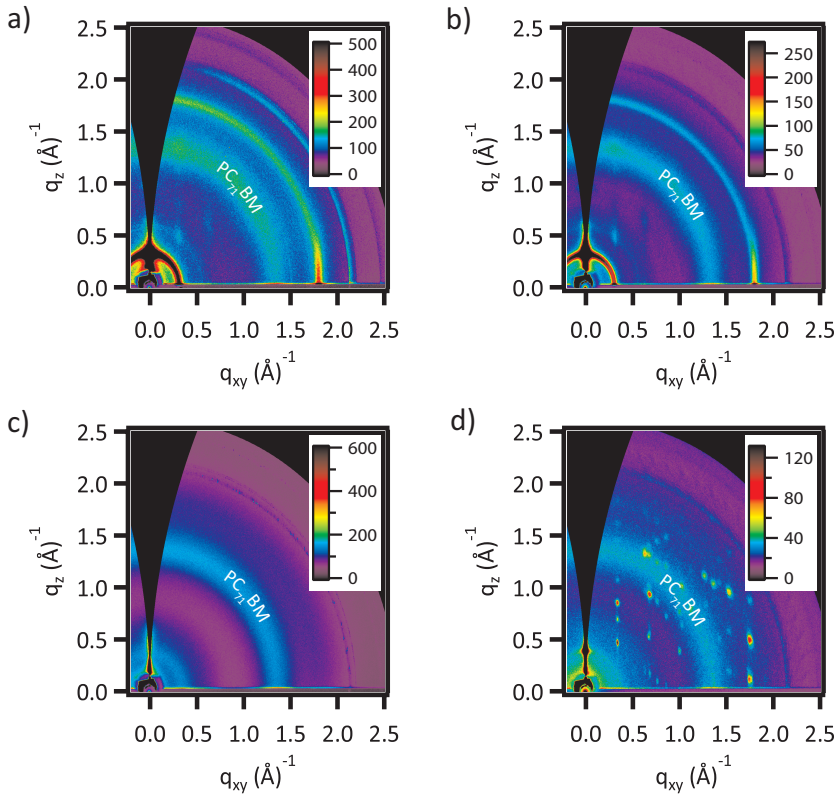

Figure 2.4: Two-dimensional GIWAXS plots of (a) *d*-DTS(PTTh$_2$)$_2$:PC$_{71}$BM film as-cast, (b) *d*-DTS(PTTh$_2$)$_2$:PC$_{71}$BM film annealed at 80°C, (c) *d*-CDT-(PTTh$_2$)$_2$:PC$_{71}$BM film as-cast, and (d) *d*-CDT(PTTh$_2$)$_2$:PC$_{71}$BM film annealed at 80°C. All samples are on glass/ITO/MoO$_x$ substrates.

affects peak breadth. If this were true, then higher order peaks of the same family, e.g. (h00), would have the same fwhm. However, paracrystalline disorder and lattice-parameter fluctuations can significantly contribute to, and even dominate, peak broadening.[76] Because the crystal structure of these materials is not known, and some of the scattering patterns do not show enough reflections we have not performed this type of analysis. Nevertheless, preliminary examination of pris-

tine *d*-DTS($PTTh_2$)$_2$ films suggests that disorder likely contributes to the peak breadth in these systems (Supporting Information Figure S7).

Annealing of *d*-DTS($PTTh_2$)$_2$:$PC_{71}BM$blend films at 80°C (Figure 2.4b) slightly increased the d-spacings for the (100) and (010) reflections. However, the crystallite correlation lengths did not change significantly with annealing (see Table S3 in the Supporting Information). The respective angular distributions of the (100) and (010) peaks still show that the crystals adopt an edge-on orientation; however, there is less amorphous scattering present and mixed order peaks are more defined, suggesting greater ordering.

***d*-CDT($PTTh_2$)$_2$:$PC_{71}BM$ Films.** Despite its chemical similarity to *d*-DTS($PTTh_2$)$_2$, *d*-CDT($PTTh_2$)$_2$ has significantly different crystalline ordering in thin films. For as-cast *d*-CDT($PTTh_2$)$_2$:$PC_{71}BM$ BHJs (Figure 2.4c), the GIWAXS reveals only diffuse, amorphous type rings, making it difficult to determine the molecular spacings. Relative to both as-cast neat *d*-CDT($PTTh_2$)$_2$ (Supporting Information Figure S8) and *d*-DTS($PTTh_2$)$_2$:$PC_{71}BM$ films, these films lose their preferred orientation and the higher order reflection peaks disappear. The presence of $PC_{71}BM$ reduces the degree of order much more in *d*-CDT($PTTh_2$)$_2$:$PC_{71}BM$ films compared to *d*-DTS($PTTh_2$)$_2$:$PC_{71}BM$ films.

The annealed *d*-CDT($PTTh_2$)$_2$:$PC_{71}BM$ (Figure 2.4d) blend film shows well resolved scattering peaks that were also present in the annealed pristine *d*-CDT-

$(PTTh_2)_2$ films (Supporting Information Figure S8). The d-spacing determined from the out-of-plane portion of the (100) reflection is 16.1 Å, noticeably less than *d*-DTS$(PTTh_2)_2$:$PC_{71}BM$ films. This distance supports the assignment of the (100) as stacking along the short axis of the molecule because the bridgehead carbon atom has shorter bond lengths than the silicon bridgehead atom. Almost no angular distribution of the peaks is observed, suggesting that the crystallites probed by the GIWAXS experiment are highly textured (oriented in the same way). Unlike in the as-cast films of *d*-CDT$(PTTh_2)_2$, the addition of $PC_{71}BM$ noticeably increases the degree of preferential orientation of the crystallites in the annealed films. A corresponding increase in preferential orientation was not seen for the addition of $PC_{71}BM$ in annealed *d*-DTS$(PTTh_2)_2$ films. Why this occurs for *d*-CDT$(PTTh_2)_2$ and not for *d*-DTS$(PTTh_2)_2$ is unknown. However, it may provide more insight into the reason for the reduced device performance of *d*-CDT$(PTTh_2)_2$. We expect that excessively large crystallites contribute to the poor performance of *d*-CDT$(PTTh_2)_2$ based devices. The crystallite correlation length in the [010] direction reached the resolution limit for Scherrer analysis ($\sim$190 nm),[77] suggesting very large crystals. In fact, the appearance of a high population of large (in-plane) crystallites in annealed *d*-CDT$(PTTh_2)_2$:$PC_{71}BM$ films is clearly visible in polarized optical microscopy (Supporting Information Figure S11) and also in selected-area electron diffraction where large crystals are

much more prevalent in annealed *d*-CDT($PTTh_2$)$_2$:$PC_{71}BM$ films compared to annealed *d*-DTS($PTTh_2$)$_2$:$PC_{71}BM$ films. The positions of the reflections match those of the pristine film, and no crystallization of $PC_{71}BM$ is observed (Supporting Information Table S4).

Selected-Area Electron Diffraction.

Electron diffraction measures the in-plane scattering distribution over areas of micrometers and is a useful complement to GIWAXS. Typical electron diffraction patterns of *d*-DTS($PTTh_2$)$_2$ and *d*-CDT($PTTh_2$)$_2$ using a 2 μm beam diameter are shown in the Supporting Information Figure S12. The as-cast *d*-DTS($PTTh_2$)$_2$ BHJ shows a narrow, continuous ring corresponding to the 1.80 $Å^{-1}$ peak of the donor along with a broad ring corresponding to the fullerene is observed. The isotropic, continuous ring implies a large degree of scattering either from small discrete crystals or a liquid crystalline-like structure. Annealing the film at 80°C narrows the ring at 1.80 $Å^{-1}$. A number of new, discrete spots begin to emerge suggesting the crystals are either rare and/or large in size; however, we do not observe any crystallization of the fullerene. Several new spots appear at q values slightly less than that of the 1.80 $Å^{-1}$ ring, a few others within the broad fullerene ring, and some at q values larger than 1.80 $Å^{-1}$. The *d*-CDT($PTTh_2$)$_2$ BHJ film shows a high degree of crystallinity in both the as-cast and annealed films. The

selected area electron diffraction appears as a set of discrete spots with a number of closely spaced q values suggesting the presence of polymorphs in the film. Relating this to the broad peaks observed in the GIWAXS data, the superposition of the narrow peaks likely blur together; alternatively, the scattering from the large crystallites in-plane may effectively be missed due to the small fraction of the crystals with the correct in-plane orientation that obey the Bragg condition. The SAED of *d*-CDT($PTTh_2$)$_2$ BHJ samples annealed at 80°C shows similar patterns, again suggesting a high degree of order in agreement with the optical microscopy and GIWAXS results. The SAED results again illustrate the sensitivity of the morphology upon processing and chemical changes.

HR-TEM and STEM.

The morphology of the silicon- and carbon-bridged BHJ materials was further characterized using HR-TEM and STEM. As shown in previous studies,[23,54] HR-TEM allows for the direct imaging and mapping of the regions giving rise to the peaks observed in other scattering experiments. Selected regions of as-cast and annealed *d*-DTS($PTTh_2$)$_2$ BHJ films appear in Figure 2.5. Additional image processing was performed to highlight regions showing lattice planes with q $\approx$ 0.31 $Å^{-1}$ (2.0 nm), i.e. regions with crystalline *d*-DTS($PTTh_2$)$_2$. In the as-cast samples, the size of the donor crystallites appears to be small. Annealing at 80° C

increases the size of the crystallites; some have dimensions in excess of 50 nm. The large structural changes observed on annealing at 80°C highlight the complexity of small molecule solar cells and their sensitivity to processing conditions.

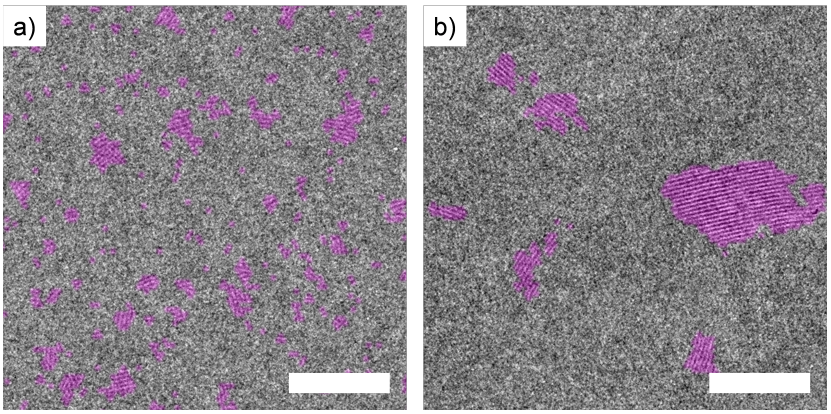

Figure 2.5: HRTEM image of the a) as-cast and b) annealed *d*-DTS-$(PTTh_2)_2$:$PC_{71}BM$ BHJ. Lattice planes showing lattice planes with d∼2 nm are highlighted in magenta. The as-cast film shows small randomly oriented crystals. Upon thermal annealing the size of the crystals increases dramatically. Scale bars are 50 nm.

The structure of the as-cast *d*-CDT$(PTTh_2)_2$ BHJ film shows a high degree of crystallinity with clearly resolvable crystallites and large length scales on the order of micrometers (Supporting Information). Unlike the crystals in the *d*-DTS-$(PTTh_2)_2$ BHJ, analysis of the data shows a number of close d-spacings in the range of 1 to 3.6 nm. HR-TEM and STEM measurements show that the carbon- and silicon- bridged small molecules display large differences in their nanostructure in the thin- film devices. Overall, films with the carbon-bridged molecule are more ordered and have larger crystals.

2.3.3 Characteristics of Solar Cells.

***In Situ* Current-Voltage Measurements.**

Due to the significant morphological changes that occurred during thermal annealing for the neat and BHJ films for the two compounds, it is difficult to decide *a priori* what processing conditions might lead to the best power conversion efficiency in solar cells. We have employed an *in situ* current-voltage (J-V) annealing setup that tracks the current-voltage characteristics in the dark and under illumination with time and temperature changes,[43] the results from which allow us to correlate morphological development during annealing with device performance. Two types of *in situ* J-V annealing measurements were done: a temperature ramp study in which J-V measurements were taken while the device temperature (hot plate) was increased from room temperature at a constant rate (200°C/h or 3.3°C/min), and an isothermal time study where devices were held at approximately the temperature which gave the highest J_{SC} for an extended period of time to monitor their stability.

For all of the *in situ* J-V studies, device characteristics were obtained by illumination from a 620 nm red LED array. We measured the UV-visible absorption *in situ* as the films were heated and generally observed that the overall intensity of the absorption maxima (500-800 nm) increased with annealing

(Supporting Information Figures S4 and S5). *d*-DTS($PTTh_2$)$_2$:$PC_{71}BM$ and *d*-CDT($PTTh_2$)$_2$:$PC_{71}BM$, however, showed very little change around 620 nm at the relevant annealing temperatures, suggesting that significant changes in J_{SC} are not due to large changes in the absorbance. Note that when temperature is increasing, the V_{OC} decreases as predicted by the conventional circuit model of a solar cell (a diode in parallel with a current generator).[43]

The *d*-DTS($PTTh_2$)$_2$:$PC_{71}BM$ devices subjected to the temperature ramp study undergo an increase in current with temperature from room temperature to 50°C, possibly due to thermal activation of the current as seen in Figure 2.6a. Continued heating results in a sharp increase in J_{SC} and a distinct peak at 90°C, well below the blend melting temperature of 193°C. While this peak is partially due to the thermally activated transport, our physical characterization shows that changes in morphology of the active layer must also significantly contribute to J_{SC}. As temperature increases beyond the peak at 90° C, the J_{SC} decreases rapidly. At these higher temperatures, the drop off in J_{SC} is dominated by further changes in the blend microstructure as *d*-DTS($PTTh_2$)$_2$ crystallites grow to a size that is expected to be much too large for efficient charge extraction. GIWAXS and polarized optical microscopy images of *d*-DTS($PTTh_2$)$_2$:$PC_{71}BM$ films annealed at 145°C show evidence for preferential orientation of large crystallites, which should negatively affect device performance. A similar peak in J_{SC} has been ob-

served during *in situ* J-V measurements of P3HT:PCBM; however, the J_{SC} does not begin to decrease until a much higher temperature (150°C) when large scale PCBM crystallites form.[43] In P3HT:PCBM, the J_{SC} does not decrease rapidly and remains at an elevated value for an extended temperature range suggests that, unlike the small molecule system, the improved morphology that is attained during heating is more stable and does not quickly evolve to an undesired microstructure. Previously, *d*-DTS($PTTh_2$)$_2$ devices were annealed at 110°C (100°C) for 2 min (10 min) to obtain the best PCE.[55,78] This annealing procedure is likely one of many that would lead to a reasonable morphology and thus a good efficiency. However, based on the rapid decline in current during the temperature ramp at temperatures above 90°C, we expect that the devices are unstable at annealing times beyond 2 min at this temperature.

It is of interest to understand the changes in photocurrent as a function of temperature. The observed peak in J_{SC} is likely a result of the interplay between two major factors: irreversible changes due to morphological evolution upon heating and improved charge generation and extraction with increasing temperature. Interestingly, while the small molecule OPVs in this study show thermally activated current, *in situ* thermal annealing studies of P3HT:PCBM did not show noticeable thermally activated behavior up to the maximum temperatures studied (200°C).[43] To probe the contribution from thermally activated transport, a *d*-DTS($PTTh_2$)$_2$

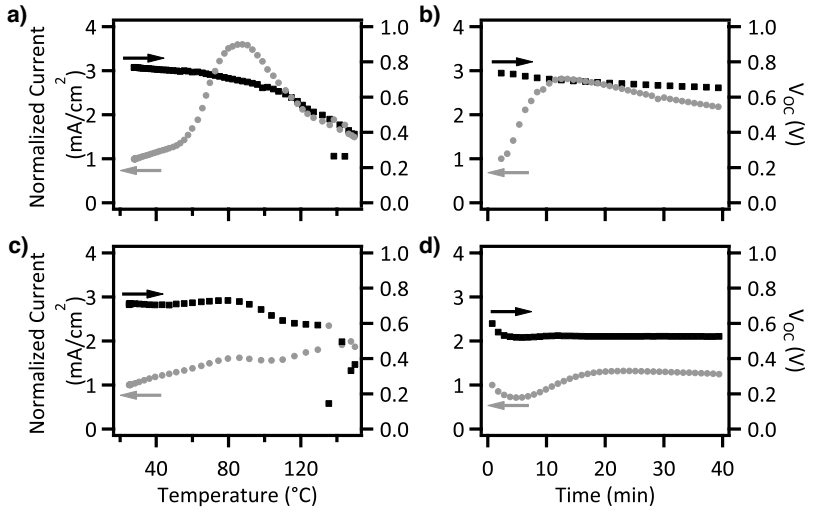

Figure 2.6: *In situ* annealing: temperature ramp and isothermal studies for *d*-DTS(PTTh$_2$)$_2$ (a and b) and *d*-CDT(PTTh$_2$)$_2$ (c and d) OPVs with J_{SC} shown with gray circles and V_{OC} shown with black squares. The temperature was ramped at $\sim$ 2.5°C/min for (a) and (c). For (b) the temperature was held constant at $\sim$ 80°C and for (d) the temperature was held constant at $\sim$ 97°C.

device was subjected to a constant temperature anneal, slowly cooled to room temperature, heated back to the same temperature, and so on. It is found that the J_{SC} steadily decreases during the cooling step. When the temperature is set to increase again, the J_{SC} tracks the temperature increase, but this second peak in J_{SC} occurs at a lower value than during the first heating cycle, and the peak value continues to drop with successive heating cycles. The repeated peaks in J_{SC} suggest that thermally activated transport plays a noticeable role but overall is outweighed by irreversible cycle-by-cycle morphological development that reduces performance with extended annealing. In the isothermal (80°C) annealing test

the results of which are shown in Figure 2.6b, the J_{SC} initially increases, peaks in 10 min, and then degrades steadily. Because the temperature is constant in these experiments, thermally activated transport is not expected to play a major role in the current change after the first few minutes. The slow decrease in J_{SC} once again suggests that extended annealing allows deleterious changes in the morphology.

The change in photocurrent with temperature provides information about the recombination mechanism in these devices. One expects reversible thermally activated transport in organic semiconductors from thermally activated detrapping as long as no substantial changes in structure occur.[79] Temperature-dependent transient photocurrent measurements[80] on annealed *d*-DTS($PTTh_2$)$_2$ devices (Figure 2.7) show that the amount of charge extracted increases with temperature, while the exponential time constant remains relatively unchanged, suggesting that thermally activated detrapping cannot account for the entirety of the thermally activated current. Instead, the increased concentration of charge indicates an improvement in generation as a function of temperature suggesting either a reduction in geminate recombination or thermally activated exciton diffusion.[81] This proposition is consistent with the lack of thermally activated photocurrent in P3HT:PCBM which does not exhibit significant geminate recombination or issues with exciton diffusion in efficient devices.

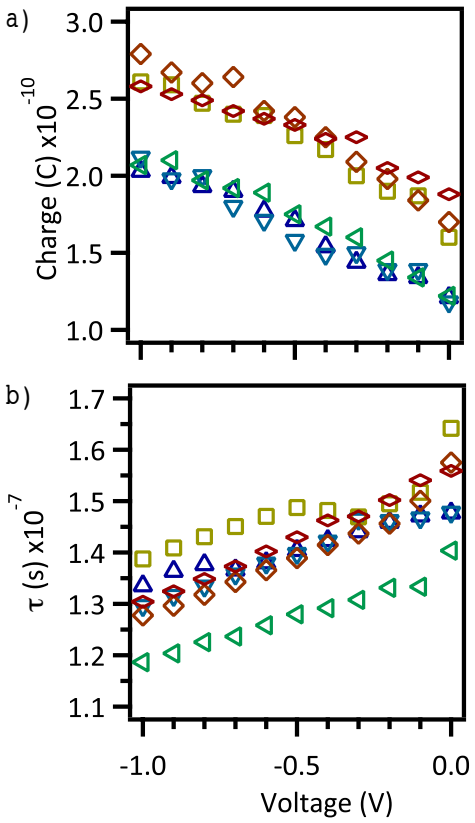

Figure 2.7: Integrated charge and time constant, τ, from transient photocurrent measurements for an annealed *d*-DTS($PTTh_2$)$_2$ based device at 27°C (dark and medium blue triangles), heated to 40°C (yellow squares), 53°C (orange diamonds), 68°C (red sideways diamonds), and then cooled to 28°C (green sideways triangles).

The *d*-CDT($PTTh_2$)$_2$:$PC_{71}BM$ devices behave very differently from the *d*-DTS($PTTh_2$)$_2$ based devices during the temperature ramp study as shown in Figure 2.6c. From room temperature to 50°C, the current in the *d*-CDT-($PTTh_2$)$_2$:$PC_{71}BM$ devices increases in a manner similar to that in the *d*-DTS-($PTTh_2$)$_2$ ones, which again is likely due to thermally activated current. Rather than peaking sharply, the current continues to increase slowly and reaches a sub-

tle peak around 86°C after which it starts to drop off. However, the current density increases again at higher temperatures (110°C - 147°C) until the film melts and shorts the device. During the isothermal (97°C) annealing study, *d*-CDT($PTTh_2$)$_2$:$PC_{71}BM$ devices exhibit a J_{SC} that initially decreases but then increases to peak slightly above the initial value after which it steadily decreases with extended annealing time as shown in Figure 2.6d. The increases in J_{SC} observed in the *d*-CDT($PTTh_2$)$_2$ based devices during annealing are much lower (75% increase vs 350% in the temperature ramp and 25% increase vs 300% in the constant temperature study) than for *d*-DTS($PTTh_2$)$_2$ devices. The smaller increases in J_{SC} during the temperature ramp and the decrease in J_{SC} during the constant temperature study suggest that charge generation and extraction is significantly less efficient at all temperatures than in the silicon-bridged compound. The poor performance of these devices is consistent with the morphological data from GIWAXS and TEM experiments which show that *d*-CDT($PTTh_2$)$_2$ crystallizes readily with annealing and forms large crystals up to micrometers in size, which are much too large to form an optimal BHJ morphology.

In situ current-voltage measurements provide additional insight into the processes that influence device characteristics during annealing and support the picture that irreversible morphological development can result in efficient morpholo-

gies that are difficult to maintain in small molecule BHJs at elevated temperatures, especially in *d*-CDT(PTTh$_2$)$_2$:PC$_{71}$BM devices.

Current-Voltage Characteristics.

As observed in other systems, the devices made with the silicon based analog have a higher PCE than the carbon-based compounds processed without additives and using conditions from the *in situ* thermal annealing experiments. The J-V curves are shown in Figure 2.8 along with EQE spectra in Figure 2.9a and 9b for annealed and as-cast devices with the device characteristics summarized in Table 2.2. The as-cast *d*-DTS(PTTh$_2$)$_2$:PC$_{71}$BM device starts out with poor efficiencies of 0.7% and improves with annealing (80° C for 5 min) to 3.4%, mostly due to large improvements in J_{SC} and fill factor. On the other hand, as-cast *d*-CDT-(PTTh$_2$)$_2$:PC$_{71}$BM starts out with a poor efficiency of 0.2% and only gets worse with annealing, due to losses in the J_{SC} and V_{OC}. We attribute the poor efficiency for *d*-CDT(PTTh$_2$)$_2$:PC$_{71}$BM to the larger domain sizes of *d*-CDT(PTTh$_2$)$_2$ observed in GIWAXS and TEM even in the as-cast state. The performance of the devices is very sensitive to processing conditions, as can be seen from the J-V data measured *in situ* during heating, resulting in variation in PCE from substrate to substrate. The performance among solar cells on the same substrate is consis-

tent; however, and the values reported in Table 2.2 are the average of all working devices on the best performing film of each type and annealing condition.

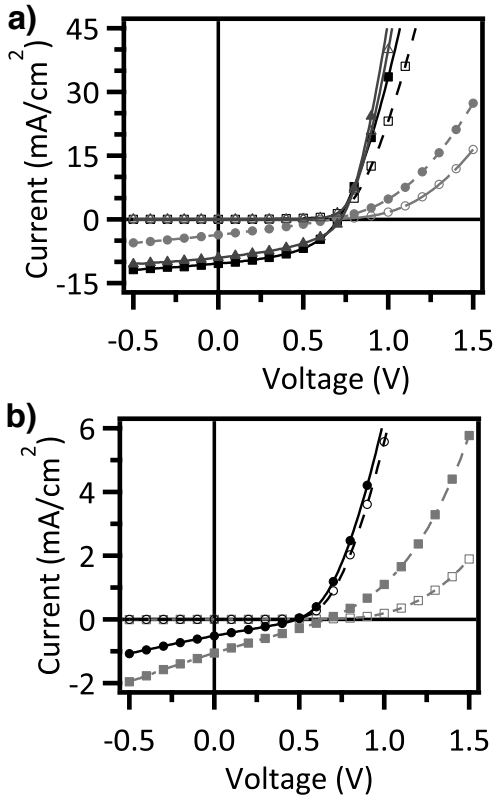

Figure 2.8: J-V characteristics for (a) *d*-DTS($PTTh_2$)$_2$:$PC_{71}BM$ and (b) *d*-CDT-($PTTh_2$)$_2$:$PC_{71}BM$ OPVs. The light (filled) and dark (open) current are shown for as-cast (gray circles) devices and devices annealed pre (black squares) and post top contact evaporation (dark gray triangles). The *d*-DTS($PTTh_2$)$_2$ OPVs improve with annealing, while the *d*-CDT($PTTh_2$)$_2$ OPVs actually lose performance with annealing (80°C for 5 min).

	condition	J_{SC} (mA/cm^2)	V_{OC} (V)	FF	PCE (%)
d-CDT(PTTh$_2$)$_2$	as-cast	1.0 (0.1)	0.66 (0.01)	0.26 (0.01)	0.2 (0.1)
	annealed	0.6 (0.1)	0.50 (0.3)	0.28 (0.1)	0.09 (0.02)
d-DTS(PTTh$_2$)$_2$	as-cast	3.6 (0.2)	0.67 (0.1)	0.29 (0.1)	0.7 (0.1)
	annealed (precontact)	9.9 (0.4)	0.70 (0.01)	0.47 (0.01)	3.3 (0.1)
	annealed (postcontact)	8.9 (0.2)	0.70 (0.02)	0.43 (0.02)	2.7 (0.2)

[a]The values reported are averages (standard deviations) of all working device pixels on the best performing film.

Table 2.2: OPV Device Characteristics for As-Cast and Annealed *d*-CDT(PTTh$_2$)$_2$:PC$_{71}$BM and *d*-DTS-(PTTh$_2$)$_2$:PC$_{71}$BM Blends[a].

Charge Transfer States in External Quantum Efficiency Measurements.

To further understand how the changes in ordering upon annealing influence the optoelectronic characteristics, we examined the low-energy tail of the EQE. The tail provides information about sub-bandgap states in the blend.[82,83] For example, charge transfer excitations (CTEs) have been suggested to be important intermediates in generation and recombination processes. The EQE data for both BHJs show a tail extending to ∼1.1 eV for *d*-DTS($PTTh_2$)$_2$ and ∼1.2 eV for *d*-CDT($PTTh_2$)$_2$, which are values close to the offsets of the HOMO and LUMO of the separated donor and acceptor. We were not able to extend the lower range of the EQE data further due to the limitations of our measurement system. We fit the tail with a combination of two Gaussians, one for the main absorption due to the donor and one for a relatively sharp subgap feature, and an exponential that describes the energetic disorder of CTE (Figure 2.9c and 9d).[82] The feature centered at ∼1.48 eV is likely a donor transition due to its proximity to the absorption edge.

Our morphological characterization suggests the presence of polymorphic packing motifs, and this peak is likely due to an alternate arrangement of the donor units than in the main absorption feature of the donor. Interestingly, the fits for the tails were identical for as-cast and annealed devices suggesting that the tail is not strongly impacted by increases in crystalline ordering. The tail assigned

to CTE states is much narrower than the tail found in the P3HT:PCBM system studied by Presselt et al.[82] A comparison of the band tails of the small molecules to P3HT:PCBM and PCDTBT:$PC_{71}BM$ devices are shown in Figure 2.10. Both small molecule blends have sharper tails than the P3HT blends and the *d*-CDT-$(PTTh_2)_2$ blend has a sharper tail than the related polymer PCDTBT.[83] The steeper slope for the exponential tail suggests that the energetic distribution of CT states is less broad than in polymer BHJs; a possible origin is the relative purity of the domains compared to polymers where molecular mixing of fullerenes in the polymer have been observed in many systems.[43–45,65,84] Whether it could prove to be a key advantage for small molecule OPVs leading to higher open circuit voltages is still unknown.

2.4 Conclusion

We have performed a systematic study of the optoelectronic characteristics of two promising small molecule donors for solution processed small molecule OPVs that differ by only the bridgehead atom (carbon for *d*-CDT$(PTTh_2)_2$ and silicon for *d*-DTS$(PTTh_2)_2$). The largest difference between the compounds is their thermal behavior with higher thermal transition temperatures observed for the silicon compound. Both compounds have crystalline phases and thermal anneal-

ing at temperatures below the melt increases the size of the crystalline domains. Despite the simple change of bridgehead atom, the observed scattering patterns suggest differing crystal structures in *d*-CDT($PTTh_2$)$_2$ and *d*-DTS($PTTh_2$)$_2$.

The larger crystalline domains for *d*-CDT($PTTh_2$)$_2$ lead to lower performance in BHJ OPVs. BHJs with both *d*-CDT($PTTh_2$)$_2$ and *d*-DTS($PTTh_2$)$_2$had sharper tails in the EQE spectra than polymer:fullerene BHJs. This feature suggests that the crystallinity due to small molecules has the potential to improve the V_{OC} in OPVs due to a reduction in electronic tail states. The results here show that to gain these benefits, improvements in control of the domain sizes of crystallization are essential.

No attempt was made here to use processing additives that have successfully increased the power conversion efficiency of similar small molecule BHJ OPVs.[23,24,85] It is known that using 0.25% 1,8-diiodooctane as an additive boosts the efficiency of *d*-DTS($PTTh_2$)$_2$ to 5.6%.[85] In these cases, the domain sizes are kept small during the casting process. The results here suggest that such structures in as-cast films should be examined to determine if cold crystallization can limit the morphological stability at operational temperatures in practical solar cells.

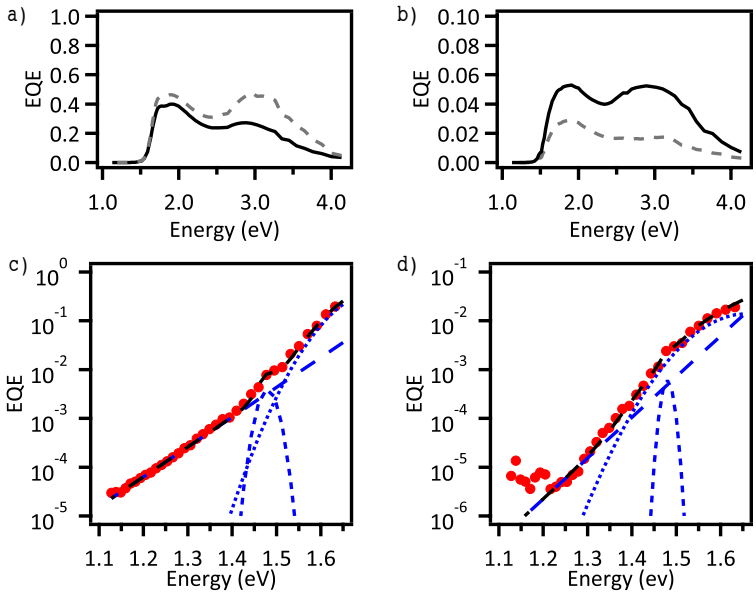

Figure 2.9: The EQE (as fractions) of (a) *d*-DTS(PTTh$_2$)$_2$:PC$_{71}$BM and (b) *d*-CDT(PTTh$_2$)$_2$:PC$_{71}$BM OPVs with as-cast (black) and annealed (gray dashed) lines. EQE of the low energy tail of annealed *d*-DTS(PTTh$_2$)$_2$:PC$_{71}$BM (c) and *d*-CDT(PTTh$_2$)$_2$:PC$_{71}$BM (d) OPV devices plotted on a log scale vs energy. The red circles show the experimental data, and the black dashed line shows the fit with two Gaussians and an exponential. The broader Gaussians centered at higher energy (blue dotted line) are from the small molecule absorption (E_c = 1.73 eV, σ = 0.23 for *d*-DTS(PTTh$_2$)$_2$ and E_c = 1.66 eV, σ = 0.24 for *d*-CDT(PTTh$_2$)$_2$. The Gaussians at lower energy (blue dashed line) are both centered at 1.48 eV. The exponentials (blue long-dashed line) have slopes of 14.1 for *d*-DTS(PTTh$_2$)$_2$ and 19.2 for *d*-CDT(PTTh$_2$)$_2$.

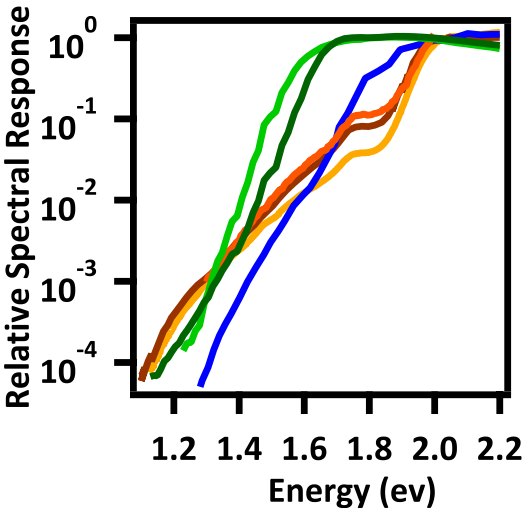

Figure 2.10: The low energy tail of the relative spectral response for *d*-DTS(PTTh$_2$)$_2$:PC$_{71}$BM (dark green), *d*-CDT(PTTh$_2$)$_2$:PC$_{71}$BM (light green), P3HT:PCBM (yellow, orange (Presselt)[82] and brown (Street)[83]), and PCDTBT:PC$_{71}$BM (blue (Street)[83]). The slopes of the exponential tails are 10.1, 10.1, 10.7, 17.8, 25.5, and 17.8 eV^{-1}, respectively.

Chapter 3

Studies of a Non-Fullerene Acceptor: DTI

3.1 Introduction to DTI

Fullerene derivatives are the most common acceptors used in organic solar cells because they tend to accept electrons efficiently from nearly all donor materials; however, they have poor absorption in the visible range of the solar spectrum.[86] Therefore it is desirable to design non-fullerene acceptor molecules that retain the good electron-accepting properties but also have a strong absorption in the visible so that they can more effectively contribute to the photocurrent of the solar cell. DTI, a decacyclene triimide derivative is one such non-fullerene small molecule acceptor.[87] It has been found that DTI performs better in as-cast than in annealed solar cells and morphological studies suggest that DTI forms π-stacked columns that run in the plane of the film.[88] We performed photoluminescence quenching

studies to elucidate the difference in performance of as-cast and annealed solar cells made with DTI.

3.2 Photoluminescence Quenching

We used fluorescence quenching studies to better understand the behavior of excitons and the formation of charges in the DTI blend films. By selectively exciting at wavelengths where absorption is dominated by DTI (430 nm) or P3HT (570 nm), we can detect changes in the charge transfer behavior of the donor and acceptor in the film. For the as-cast film, the fluorescence is quenched 60% for the P3HT and 76% for the DTI. When the film is annealed, the DTI quenching increases to 90%, while the P3HT quenching decreases slightly to 53% (Figure 3.1).

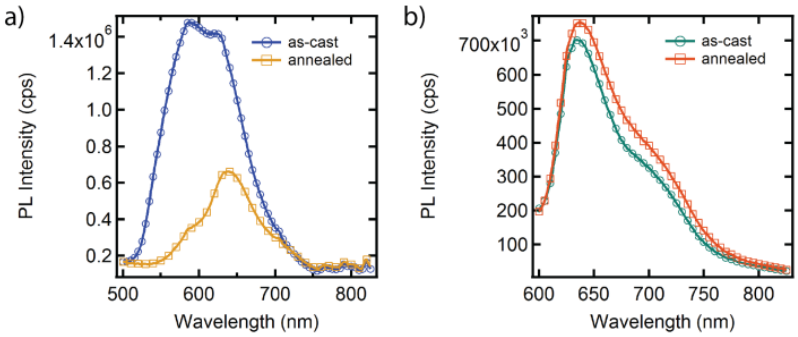

Figure 3.1: Fluorescence emission from as-cast and annealed P3HT:DTI blends excited at (a) 430 nm (in the DTI absorbance) and at (b) 570 nm (in the P3HT absorbance).

The small decrease in P3HT quenching (increase in PL intensity) suggests that charge transfer from P3HT to DTI decreases in efficiency with annealing. This is consistent with larger P3HT domains forming upon annealing,[88] which would decrease the efficiency with which excitons reach the domain interfaces; therefore, decreasing charge formation and fluorescence quenching. The increase in DTI quenching (decrease in PL intensity) suggests that charge transfer from DTI to P3HT becomes more efficient with annealing. This result is not consistent with the increase in DTI crystallite size observed;[88] however the increased order in the DTI columns could lead to a higher exciton diffusion length along the columns, allowing excitons to reach interfaces and form charges more efficiently than in the more disordered case. Exciton diffusion lengths of up to 60 nm have been demonstrated for ordered columnar liquid crystals.[89]

With only a small loss in charge formation from P3HT excitons and a sizable increase in charge formation from DTI excitons, one would expect the solar cells to improve with annealing. Instead, the efficiency decreases rapidly,[88] suggesting that the morphological changes caused by annealing lead to poorer charge extraction.

3.3 Conclusion

While DTI is a promising non-fullerene, small-molecule acceptor, it does not out-perform PCBM in solar cells, especially after the films are annealed. Based on the knowledge of the morphology of the DTI in films and our photoluminescence studies, we conclude that the DTI columns lying in the plane of the film are efficient at transporting excitons and charges along the length of the column (in the plane of the film), but not between columns (across the film) as is necessary for good transport in organic solar cells. As the film is annealed, the columns grow and become more ordered thus increasing charge formation from DTI excitons due to good exciton transport, but decreasing electron collection because of the inability of the DTI columns to transport electrons across the film.

Chapter 4

A Kinetic Monte-Carlo Study of Energy Transfer and Trapping in Systems with Restricted Geometries

4.1 Introduction

Förster energy transfer is an important physical process where an excited state (exciton) is transferred from a donor molecule to an acceptor molecule via a dipole interaction. The donor molecule has higher energy electronic transitions than the acceptor; thus its excited state has sufficient energy to excite the acceptor. One of the oldest and most common uses of Förster resonant energy transfer (FRET) is in biological applications for imaging and characterizing distances.[90] The time-dependent fluorescence intensity, $I(t)$, of the donor and trap yield information about the proximity, spatial orientation, and geometry of the donors and traps.

By monitoring $I(t)$ of molecules tagged with chromophores, the distance between the donors and traps can be deduced. Such an approach has been widely used to study protein folding and conformation and interactions between biomolecules.[90] In other contexts, FRET on 2D and surfaces has proved to be useful for studying membranes and interfaces.[91–93] FRET has also been useful for characterizing interfaces of polymer nano-domains, such as those formed by block-copolymers, micelles, and polymer nanoparticles.[94–96]

Despite its ubiquity, energy transfer of excited states is not well understood in complex geometries containing inhomogeneous distributions of donors and traps. Analytical solutions exist for homogeneous systems[97,98] and special cases of confined systems,[99–103] and almost always only consider either the high trap limit case or situations using only donor-trap transfer, in conjunction with high symmetry geometries[95] like planar,[104] spherical,[105] or cylindrical[106] symmetries. However in systems with concentrated donor domains with non-negligible donor self-transfer, the self-transfer becomes a relevant mechanism in exciton movement. Accounting for the donor self-transfer increases the complexity of the energy transfer processes and makes analytical solutions prohibitively difficult.

In this work we are interested by issues and morphologies relevant for nanostructured solar cells such as organic photovoltaics (OPVs) and dye sensitized solar cells (DSSCs). OPVs and DSSCs are emerging as a promising technology for in-

expensive solar applications.[17] OPV devices, which use a donor and acceptor organic semiconductor material to convert photons to electricity, are generally engineered to have nanostructured bulk heterojunction (BHJ) morphologies.[107,108] Controlling the morphology is crucial to the performance of the OPV because it must be optimized for the transport of both excitons (bound excited states) and charges, which have conflicting criteria. By their nature as organic chromophores, OPV donors and acceptors also have the potential for FRET to occur between them,[109–112] thus FRET is a mechanism for exciton transport within and between domains of such materials. Moreover, understanding Förster energy transfer in OPVs has recently gained interest, because FRET offers a way to enhance the OPV performance.[112–117] DSSCs also use organic chromophores to absorb sunlight and have a nanostructured morphology based on a nano-porous titania (or other wide gap semiconductor) film. New designs for DSSCs incorporate energy relay dyes,[10,12–16,118–123] which are energy donors that serve to enhance the absorption across the solar spectrum. The relay dyes energy transfer to the sensitizing dyes which are adsorbed to nanostructured titania. Thus, just as for the OPVs, energy transfer is important in exciton transfer among relay dyes[124] and from relay dyes to sensitizing dyes.

In this work, we wish to understand FRET in morphologies relevant to OPV, especially those generated by block copolymers of donors and acceptors. We

are specifically interested in situations for which donors and acceptors are phase separated in bicontinuous, nanostructured domains. However, increasing the complexity of the system makes analytical solutions prohibitively difficult. Therefore in this work we use a kinetic Monte-Carlo simulation approach to study energy transfer in model geometries. Given the complexity of the systems, finding simple measures to classify these morphologies based on the behavior of exciton trapping within them would simplify our understanding of energy transfer as a mechanism in realistic OPV morphologies. Hence, we analyze our results in terms of simple morphological measures to probe the quantitative utility of such characteristics.

The article is arranged as follows: first we validate our simulation for homogeneous donor-acceptor mixtures using known results from Förster's original solution as well as several other analytical solutions. We demonstrate that our simulation exactly reproduces the result from Förster's solution, and provides good agreement with approximate analytical solutions proposed in the literature. Subsequently, we simulate energy transfer in standard block-copolymer morphologies such as lamellae, cylinders, spheres, and gyroids (Figure 4.1a-d). We consider a range of domain sizes and two different concentrations of chromophores. We also look at the effect of diffuse interfaces on the energy transfer behavior by examining the effect of hyperbolic tangent interfaces on the exciton trapping behavior in lamellae. Additionally we simulate energy transfer in a microemulsion morphol-

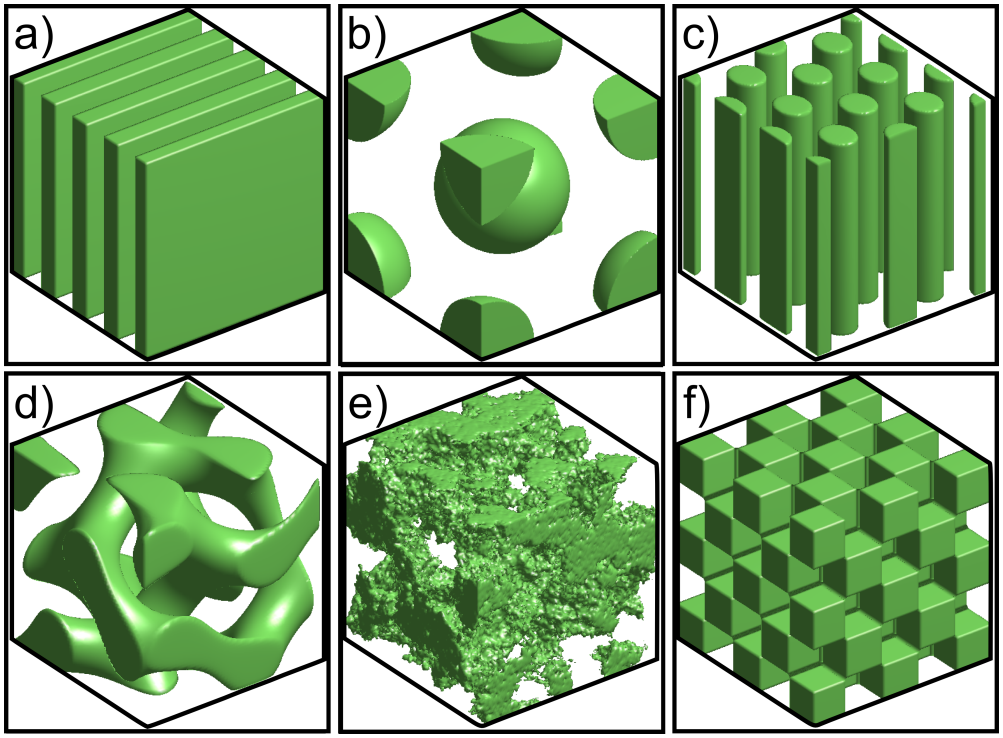

Figure 4.1: Morphologies used in the simulations showing the volume occupied by donor (or trap) chromophores for (a) lamellae, (b) BCC spheres, (c) hexagonally packed cylinders, (d) gyroid, (e) microemulsion, and (f) 3D-checkerboard.

ogy calculated for a polymer blend of A and B homopolymer and an AB diblock (Figure 4.1e). By fitting all data sets and characterizing their length scales, we are able to collapse the fitting parameters onto a single curve when considered with respect to the ratio of surface area to donor domain volume.

4.2 Kinetic Monte-Carlo Simulation Methodology

We used a a rejection free Kinetic Monte-Carlo (KMC) algorithm as described by Chatterjee and Vlachos[125] to simulate resonant energy transfer. The simulation comprises two exciton transfer processes: (1) transfer of an exciton from a donor chromophore to another donor chromophore and (2) transfer from a donor chromophore to a trap chromophore. In addition, (3) the exciton is assumed to decay through a first order process. In an OPV, Process 1 (donor-to-donor transfer) would correspond to energy transfer within one material and would lead to transport of the exciton among donor chromophores (exciton diffusion) and Process 2 (donor-to-trap transfer) would correspond to energy transfer from a chromophore with a wider energy gap to a chromophore with a smaller energy gap. In a polymer, each chromophore could be composed of a 6 to 20 monomer section. In a DSSC, Process 1 would correspond to energy transfer amongst relay

dyes and Process 2 would correspond to energy transfer from the energy relay dye to the sensitizing dye.

The above three processes give the possible simulation events:

1. $D_i^* + D_j \rightarrow D_i + D_j^*$ with Förster transfer radius R_0^{DD};

2. $D_i^* + T_j \rightarrow D_i + T_j^*$ with Förster transfer radius R_0^{DT};

3. $D_i^* \rightarrow D_i$ with donor exciton lifetime, τ_D

where D_i^* is the position of the current exciton on a donor, D_j or T_j are donors or traps at position j, and D_j^* or T_j^* are the donors or traps after the exciton has transferred to them. We do not include events for exciton transfer between traps or from traps to donors. The probability of each process occurring is proportional to its rate. Each resonant energy transfer process has the rate,

$$rate = \frac{1}{\tau_D}\left(\frac{R_0}{r_{ij}}\right)^6 \tag{4.1}$$

where R_0 is the Förster transfer radius and τ_D is the lifetime of the exciton. The characteristic distance for energy transfer is the Förster transfer radius, R_0, which depends on the dipole alignment of the molecules and the spectral overlap of the donor's emission and the trap's absorption spectra. Each process has its own

Förster transfer radius, denoted by the superscripts (R_0^{DD} and R_0^{DT}) for transfer from donors to donors and to traps.

Using the rates described above, results were generated as follows. Each simulation was run for one exciton at a time and continued until the specified time was reached or until the exciton was trapped. For each simulation, a new, randomly generated distribution of donors and traps was created according to the specified morphology and the donor on which the exciton begins was also randomly selected. We averaged the results of 10^4 to 10^6 simulations to collect statistics regarding exciton motion and the survival probability. In the results presented below, exciton decay was neglected in the simulations to simplify data analysis. However, to account for exciton decay in the $G^D(t)$, one would simply multiply by the decaying exponential function $exp(-t/\tau_D)$, which describes how excitons on donors decay on the time scale of the exciton lifetime τ_D in the absence of energy transfer.[98]

In the simulations, all distances are normalized by R_0^{DD} and all times are normalized by τ_D, the donor exciton lifetime. Concentrations within the total volume are given in terms of the the dimensionless donor concentration, $C_D = (4\pi(R_0^{DD})^3/3)\rho_D$, and the dimensionless trap concentration, $C_T = (4\pi(R_0^{DT})^3/3)\rho_T$, where ρ_D and ρ_T are the donor and trap number densities, respectively. The mean square displacement (MSD) and $G^D(t)$, the probability

that the exciton is still on a donor at time t, are calculated for each data set (The experimentally observed fluorescence intensity of donors, $I(t)$, is proportional to $G^D(t)$). Additional details of the simulation are given in Section 4.7, Simulation Notes.

Our simulation model makes several simplifying assumptions that may not necessarily apply to certain experimental systems. Firstly, due to the Förster rate expression that we use, our model is applicable when dipoles can rotate rapidly on the timescale of hopping (such as in solution media). In the solid state, the dipoles are fixed and one should in principle account for rates that depend on the relative orientations of the dipoles. For randomly oriented, fixed dipoles the Förster transfer radius would be adjusted by a factor of $(0.8452)^{1/3}$ due to changes in the orientational factor[126] compared to the rapidly rotating dipoles. However, for a given Förster radius the rate equation remains the same. On the other hand, if the dipoles have a preferential orientation as is often the case for molecular solids, then movement of the excited states would become anisotropic. Either way, experimentally one does not generally have control over dipole orientations in donors and traps, so simulating randomly oriented dipoles gives the most informative results. In addition, due to the point dipole approximation underlying its derivation, our rate expressions are most accurate for chromophores with spacings larger than the size of the molecules. This requires spacings larger than $\sim$ 4.0 nm for

reasonably large chromophores. Thus, the rate expression becomes less accurate for characterizing transfer in systems with small intermolecular spacings, e.g. in a molecular crystal. In such cases the Förster transfer could be enhanced for nearest neighbor molecules depending on the intermolecular distance and orientation of dipoles.[127] Furthermore, even with properly calculated small-distance-dependent rates, Förster transfer does not capture the entirety of the physics for length scales smaller than ~ 0.5 nm because of additional quantum effects that become relevant at short length scales.[128] For example an alternative mechanism for energy transfer is Dexter transfer, which occurs through coupling between overlapping molecular orbitals rather than through-space dipole interactions.[128,129] In our model, the chromophores are treated as rapidly-rotating, point-dipoles, and Dexter transfer is not treated in the simulation. The average spacing between chromophores in our simulations is greater than 1.0 nm for $C_D \lesssim 10$ and $R_0^{DD} \gtrsim$1.5 nm. Thus for all cases explored in this study Dexter transfer is not a relevant mechanism.

4.3 Comparison with Analytical Models

In this section, we present results which demonstrate that our simulation approach successfully reproduces the analytical solutions proposed for systems with uniformly distributed donors and traps.

The simplest case to study is energy transfer in the high trap limit. In this configuration, a single donor, on which the exciton starts, is placed in a sea of uniformly, but randomly placed traps. The analytical solution for this situation was provided by Förster:[130,131]

$$G^D(t) = \begin{cases} exp\left(-C_T\left[\frac{\pi t}{\tau_D}\right]^{\frac{1}{2}}\right) & \text{without exciton decay} \\ exp\left(-C_T\left[\frac{\pi t}{\tau_D}\right]^{\frac{1}{2}}\right) exp\left(\frac{-t}{\tau_D}\right) & \text{with exciton decay} \end{cases} \tag{4.2}$$

where τ_D is the exciton lifetime of a donor, and C_T is the normalized trap concentration. The trap concentration is given by $C_T = 4/3\pi(R_0^{DT})^3\rho_T$, where R_0^{DT} is the Förster radius for donor to trap exciton transfer and ρ_T is the number density of traps. In our simulations, we produced such a limit by creating a homogeneous distribution of traps surrounding a single donor on which the exciton begins. In Figure 4.2 we display our simulation results which are seen to match the analytical results, both for the cases with and without exciton decay.

Approximate analytical solutions for FRET were expanded in work by Gochanour, Andersen, and Fayer (GAF)[97] and Loring, Andersen, and Fayer (LAF),[98] for the more general cases of uniformly distributed donors and traps at arbitrary concentrations. GAF and LAF used a self-consistent diagrammatic

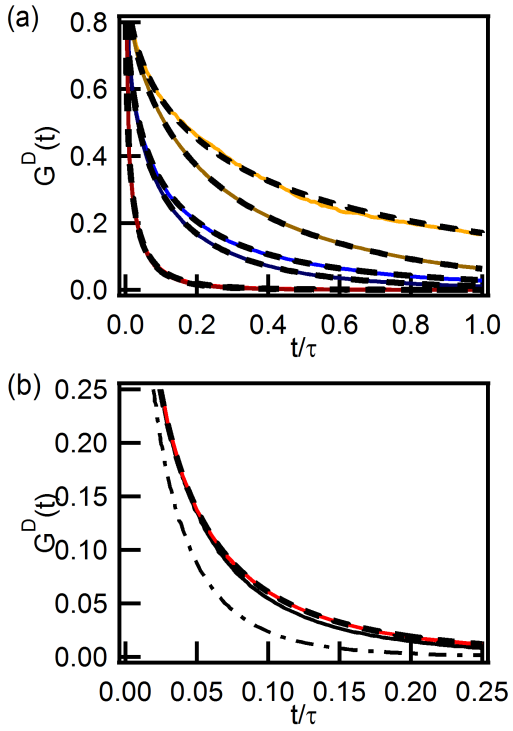

Figure 4.2: (a) The function $G^D(t)$ in the high trap limit. The dashed black lines show the analytical solution.[131] The solid colored lines show the results from the KMC simulation. Data are plotted for three different concentrations, $C_T = 1$ (yellow), $C_T = 2$ (blue), $C_T = 5$ (red) for cases of Förster transfer with (light lines) and without (dark lines) exciton decay. (b) The simulation results for $G^D(t)$ (red) in the high trap limit compared with the LAF approximate 2-body (black dash-dotted) and 3-body (black solid) results along with the exact solution (black dashed lines).

approach to the many-body transport problem in order to obtain numerical approximations for $G^D(t)$ and the mean-squared displacement of an excitation.

As another test case, we simulated several homogeneous donor-trap systems studied in the work of LAF.[98] A comparison of their results with our simulations for the high trap limit corresponding to the analytical Förster result is shown in Figure 4.2b. While there are discrepancies between the approximate analytical solutions of LAF and the exact one of Förster the data from our KMC simulation are nearly indistinguishable from the exact analytical solution. These differences between KMC simulations and LAF results in comparison to the analytical solution should be kept in mind with regard to other comparisons presented below.

We examined the effect of varying the concentrations of donors and traps, where we find that our work reproduces $G^D(t)$ and shows similar behavior to the MSD from the LAF results. The LAF work examines two sets of donor-trap concentrations corresponding to $C_D = 1.5$, $C_T = 0.5$ and $C_D = 0.5$, $C_T = 1.5$ (Figure 4.3a and c). In both cases, $R_0^{DD} = R_0^{DT}$. The KMC simulations are seen to reproduce the essential features of the LAF mean square displacement but do not asymptote to the same long-time values as the LAF results do. The mean square displacements from the KMC simulations are seen to exhibit a dependence on the simulation cell size, but it converges for large enough systems. However, the KMC simulation matches the LAF results very closely for $G^D(t)$ (Figure 4.3a),

even for small cell sizes. The simulation cell size dependence is exaggerated in the mean square displacements because the rare but large jumps disproportionately affect the mean square displacement. In contrast, the donor survival probability, $G^D(t)$, does not depend on the distance jumped, but depends primarily on the proximity of traps, and hence exhibits much weaker cell size dependence.

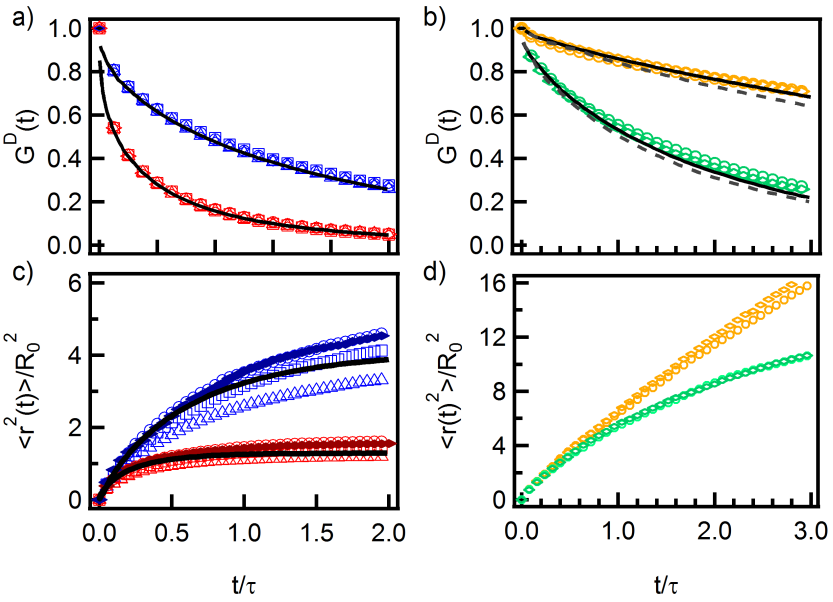

Figure 4.3: The (a) mean square displacement and (c) $G^D(t)$ of excitons in homogeneously distributed donor-trap systems. Results for $C_D = 1.5$, $C_T = 0.5$ are shown in blue and results for $C_D = 0.5$, $C_T = 1.5$ are shown in red. The (b) mean square displacement and (d) $G^D(t)$ of excitons in homogeneously distributed donor-trap systems in the low trap/trap concentration regime. Data for two concentrations are shown: $C_D = 2$, $C_T = 0.2$ (green) and $C_D = 2$, $C_T = 0.05$ (yellow). The markers show the results from the KMC simulation for different simulation cell sizes from 10 (triangles), 10 (squares), 20 (circles) and $40R_0$ (diamonds). The solid black lines show the solution from the LAF work and the dashed grey lines show the Huber results.[98]

Simulations at low trap concentrations (Figure 4.3b and d) corresponding to $C_D = 2$, $C_T = 0.2$ and $C_D = 2$, $C_T = 0.05$ are seen to closely reproduce results from LAF. The LAF 3-body solution and the Huber solution which comes from a less sophisticated approximation are compared with our results. The $G^D(t)$ from the simulation matches well with the 3-body solution, whereas the Huber solution is seen to underestimate the results. The mean square displacement is also shown in Figure 4.3d, although the LAF paper does not provide corresponding results for comparison. Increasing the trap concentration causes a faster decay in $G^D(t)$ and a slower increase in mean square displacement that plateaus to a smaller value. The cell size dependence is most noticeable in the system with the lowest trap concentration.

Overall, the simulation reproduces results from Förster, LAF, and also GAF (see Supporting Information) with high accuracy. The simulation cell size dependence has a significant affect on MSD, but very little affect on $G^D(t)$. Given the simulation's success at reproducing these results, we applied it to understand exciton trapping in ensembles with separate donor and trap domains.

4.4 KMC Simulations of Restricted Morphologies with Interfaces

Studying resonant energy transfer in scientifically relevant systems requires moving beyond homogeneous donor-trap ensembles. However, finding analytical solutions for energy transfer in inhomogeneous systems with both donor-to-trap and donor-to-donor transfer becomes intractable. In this context, the KMC simulation approach gives us a unique opportunity to examine energy transfer in heterogeneously distributed donor-trap systems. Here we present energy transfer in morphologies relevant to block copolymers where the donors and traps are separated into distinct domains.

Unless otherwise specified, results are shown and discussed for simulations with $C_D = C_T = 1$, $R_0^{DT} = R_0^{DD}$, and cell sizes of $10R_0^{DD}$. The simulations had a time step size of no larger than 0.01 τ, ran for at least 3τ, and at least 10^4 runs were averaged. Given these parameters and a reasonable value of R_0^{DD} =2 to 5 nm, the simulation cell corresponds to a sample of material 20 to 50 nm on a side with the number density of chromophores (donors and traps) ranging from 0.06 to 0.004 chromophores/nm^3, respectively.

4.4.1 Lamellar Morphology and the Effect Broadened Interfaces

Lamellae offer a simple model with flat, sharp interfaces and a single length scale to study how dividing donors and traps into domains affects the trapping kinetics. The length-scale of the lamellae (their width) affects the exciton movement and trapping. The width of the lamellae within the box are varied from one pair of D-T lamellae per simulation cell up to 10 pairs of lamellae per cell, with widths of $d = 5R_0^{DD}$ down to $d = 0.5R_0^{DD}$, respectively. These simulations were run for two different concentrations, $C_D = C_T = 1$ and $C_D = C_T = 10$. The morphologies were generated by placing randomly, uniformly distributed donors and traps in alternating regions of defined width, d, in the simulation cells.

The $G^D(t)$ and the MSD in the direction normal to the lamellae ($\text{MSD}_\perp$) are shown in Figure 4.4 for both concentrations. As the lamellar width decreases, $G^D(t)$ decays more quickly and the $\text{MSD}_\perp$ is smaller, which indicates that excitons are trapped more quickly and closer to their starting position. When the concentration is increased from $C_D = C_T = 1$ to 10, $G^D(t)$ decays much more quickly (note different time scales) meaning that the overall trapping rate increases with increases concentration. The $\text{MSD}_\perp$ is also seen to increase rapidly, but plateaus at a smaller square distance than for the lower concentration case. For example, for

lamellae of $0.5R_0^{DD}$, the higher concentration $\text{MSD}_\perp$ has plateaued at $0.24(R_0^{DD})^2$ at a time of $<< \tau_D$, but for the lower concentration, $\text{MSD}_\perp$ plateaus around $0.77(R_0^{DD})^2$ well after $3\tau_D$. The smaller $\text{MSD}_\perp$ in the high concentration lamellae is a result of increased trapping near the interface due to the increased trap concentration and the high slope prior to trapping (at short times) is consistent with faster transport within the donor domains resulting from the concentration-dependent transport behavior discussed by GAF.[97]

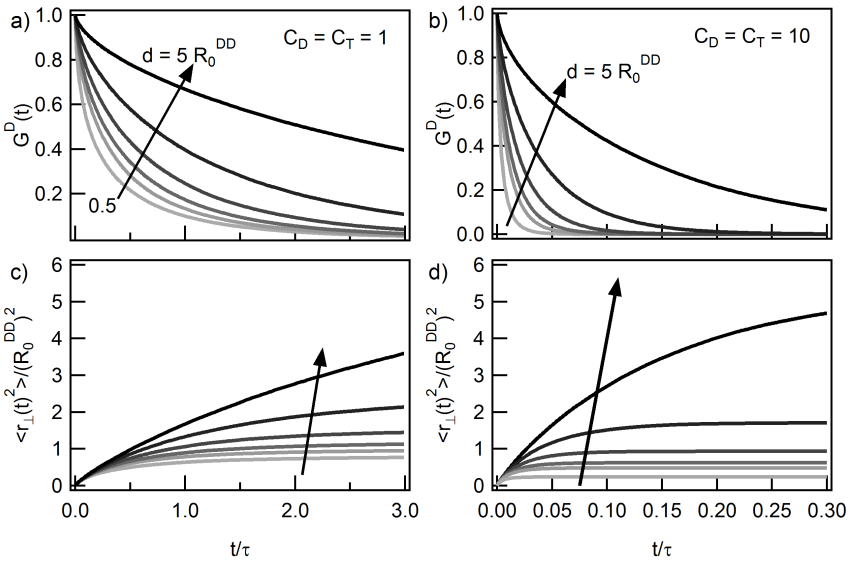

Figure 4.4: The function $G^D(t)$ and mean square displacement normal to the lamellae of the excitons for each lamellar width for $C_D = C_T = 1$ on the left and $C_D = C_T = 10$ on the right. Note different time scales.

An alternative approach to characterize the exciton trapping is to consider the position of the excitons after one exciton lifetime, τ_D. The free and trapped exciton distributions at τ_D for lamellae of several widths with $C_D = C_T = 1$

are shown in Figure 4.5. The excitons are preferentially trapped at the interface with the trap lamellae. The trapping follows an exponential function decaying away from the interface into the trap domain. The free excitons remaining in the donor region have a hill-shaped profile, which is highest at the center of each donor lamella and decreases toward the edges with negative concavity. As the lamellar width decreases, more excitons are seen to reach to the trap domain within τ_D and as a consequence fewer free excitons remain in the donor domain, in agreement with the behavior of $G^D(t)$. For comparison, an exciton distribution for the higher concentration case ($C_D = C_T = 10$) is shown in Figure 4.5b. The shape of the trapped exciton distribution is very similar, but is 50 times higher. The free excitons distribution is nonexistent at $t = \tau$ because $G_D(t)$ has decayed nearly to zero, meaning that essentially all excitons have been trapped.

While lamellae with sharp interfaces give insight into how donor and trap domain sizes affect energy transfer, they are not necessarily a realistic model for an experimental materials system with a donor-trap interface. Realistic donor-trap lamellae formed by block-copolymers will have slightly mixed, broadened interface well approximated by a hyperbolic tangent ($tanh$) function. The donor and trap regions considered in our simulations ranged from pure domains with perfectly sharp step function interfaces to finite interfaces with varying widths, L, to uniformly mixed systems (Figure 4.6a). The donor distribution is given

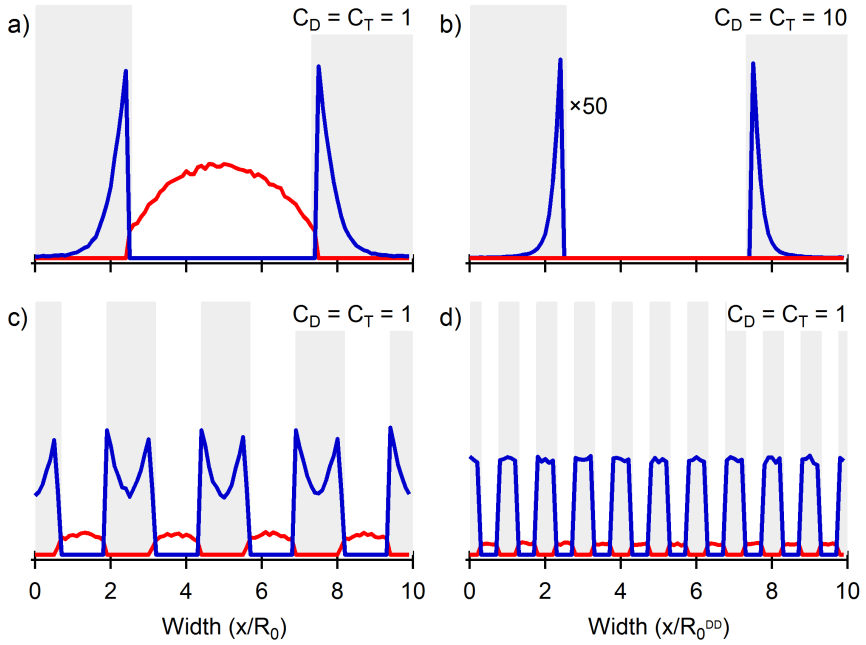

Figure 4.5: The exciton distributions for systems with different lamellar widths at one exciton lifetime. The blue lines show the trapped excitons and the red lines show the free excitons for a) $C_D = C_T = 1$ and d $= 5.0R_0^{DD}$, b) the high concentration case with $C_D = C_T = 10$ and d $= 5.0R_0^{DD}$, and the cases with narrower lamellae c) $C_D = C_T = 1$ and d $= 1.25R_0^{DD}$ and d) $C_D = C_T = 1$ and d $= 0.5R_0^{DD}$. The the distributions correspond selected widths from the data shown in Figure 4.4 at $t = \tau$. Trap and donor domains are highlighted in grey and white, respectively. For the high concentration case in b), the height is scaled down by a factor of 50 to fit on the same vertical scale.

by, $P_D(x) = 1/2(1 + tanh(x/L))$, where L controls the width of the interface, whereas the trap distributions, $P_T(x)$, are given by $1-P_D(x)$. We randomly placed donors and traps based on the probability $P_D(x)$ and $P_T(x)$(see Section 4.7). The simulations were run analogously as with the low-concentration lamellae.

Broadening the interface of the lamellae is seen to increased trapping, especially within the donor domain where traps are introduced by the broadening. The the $G^D(t)$ and the MSD in the direction perpendicular to the interface are shown in Figure 4.6b and c. As expected, $G^D(t)$ decays more quickly as the interface broadens. The $MSD_\perp$ decreases as the interface broadens, meaning that the exciton is not able to travel as far perpendicular to the interface before it is trapped. The data for the sharp interface (purple line labeled Step) in figure Figure 4.6b and c corresponds to the previously described sharp interface for the low concentration system with $d = 5R_0^{DD}$ (purple line) in Figure 4.5a and c. Introducing even a slight mixing at the interface (L=0.25) is enough to produce a noticeable difference although a much more diffuse interface (L=1.25) was necessary to have as strong an effect on $G^D(t)$ and MSD as halving the domain width did in Figure 4.5. Although the GDt for the two have look similar, the half-width LAM actually decays faster initially, but then the GDt lines cross and the trap domains.

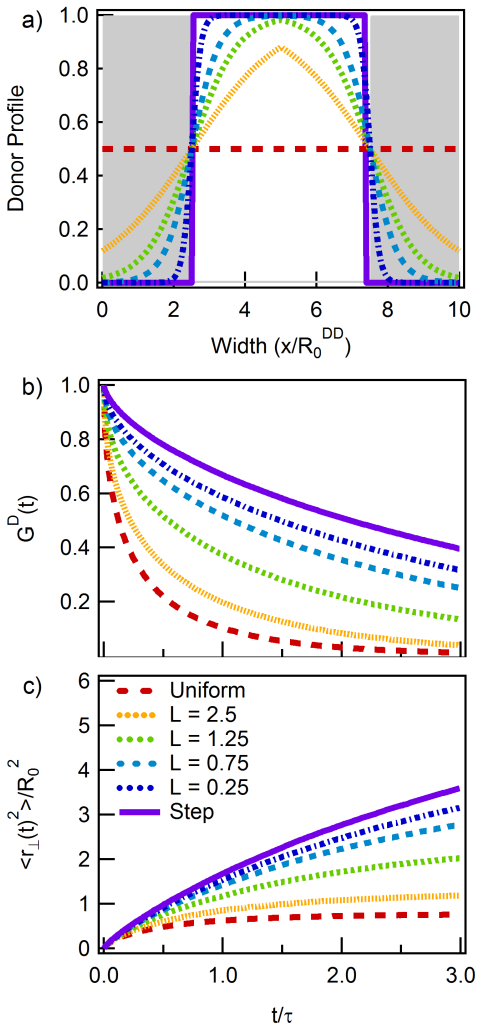

Figure 4.6: The (a) Tanh distributions of the donor density profile, ranging from a step function to a uniformly mixed system. The majority trap region is shown in grey and the majority donor region in white. The (b) function $G^D(t)$ and (c) normal component of the mean square displacement of the excitons in each interfacial system of varying L, where L controls the distribution of donors $P_D(x) = 1/2(1 + tanh(x/L))$.

The broadened *tanh* interface also affects the shape of the exciton distributions at τ_D (Figure 4.7). In the system with a sharp interface, the majority of excitons are trapped directly on the trap-side of the interface, with a rapidly decaying exponential profile away from the interface. As the interface broadens, so does the trapped exciton peak at the interface, which begins to extend into the donor domain due to the increased number of traps in that region, and also to a lesser extent, further into the trap domain due to the increased number of donors in that region. The free excitons become concentrated at the center of the donor phase with a hill-shaped profile that flattens as the interface broadens. Fewer free excitons remain for systems with broader interfaces because the traps penetrate farther into the donor domain.

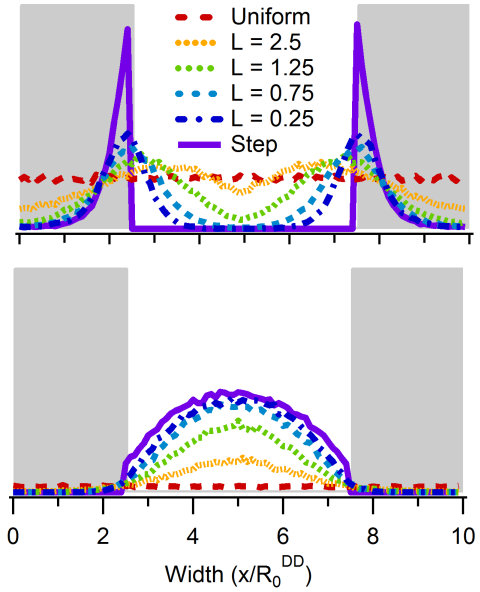

Figure 4.7: The distributions of trapped (top) and free (bottom) excitons at one exciton lifetime. The line colors correspond to the data shown in Figure 4.6. The grey and white regions show where the trap and donor domains exist, respectively, in the system with the sharp interface.

4.4.2 Body Centered Cubic Spheres and Hexagonally Packed Cylinders

Body centered cubic (BCC) spheres and hexagonally packed (HEX) cylinders are additional high-symmetry geometries that are experimentally accessible with block copolymers and easily studied with our simulation. In our simulations, all BCC and HEX morphologies were assumed to posses sharp interfaces. We explored situations in which the donors were surrounded by traps and *vice versa*. The

morphologies were generated by placing randomly, uniformly distributed donors and traps according to the defined radii on a BCC or HEX lattice.

We simulated BCC sphere morphologies with two concentrations of traps and donors corresponding to $C_T = C_D = 1$ and $C_T = C_D = 10$, respectively. Unit cell sizes were adjusted such that volume fractions of donors and traps were equal, $\phi_D = \phi_T$. Donor were placed inside spheres with traps in the inter-sphere domains (black lines) and vice versa (red lines). Thus donor and trap domain sizes both increase with increasing sphere radius. The dependence $G_D(t)$ and MSD on the sphere size shows similar behavior for the two concentrations. As the sphere size increases, the $G_D(t)$ decays more slowly and MSD reaches higher values before plateauing. Comparing identical BBC spheres with donors inside vs. outside, we see observe nearly identical $G_D(t)$ and MSD for small spheres $r_{sphere} < R_0^{DD}$ but these features diverge as the sphere size increases beyond the Förster transfer radius. For the larger spheres, $G_D(t)$ decays more slowly and the MSD is larger when donors are inside rather than outside the spheres. This size dependence suggests that domain shape is more important for trapping in large domains than in small domains. As observed in our results for lamellar morphologies, the concentration of donors (and traps) greatly affects the time scale of the exciton trapping (Figure 4.8a and b). Moreover, the mean square displacement increases more

rapidly for higher concentrations, but plateaus to a lower value (Figure 4.8c and c), whereas the $G_D(t)$ decays much more rapidly for the higher concentration.

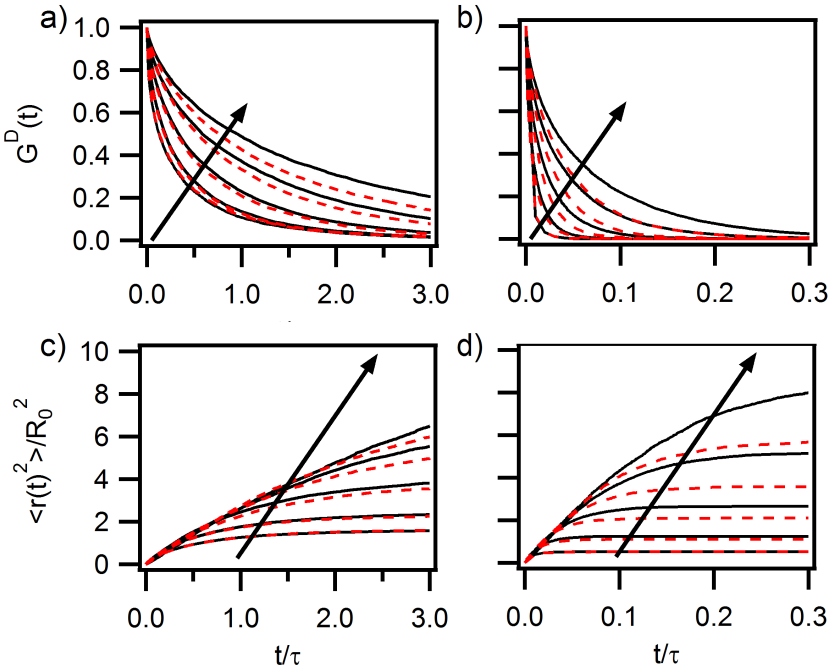

Figure 4.8: Simulation results for low concentration (C = 1) a) $G^D(t)$ and c) MSD and high concentration (C = 10) b) $G^D(t)$ and d) MSD for BCC spheres with equal donor and trap volumes for spheres with donors inside (black, solid line) and with donors outside (red, dashed line). The arrows show the direction of increasing sphere radius (decreasing SA/V_{donor}). The sphere radii are 0.2, 0.6, 1.0, 1.5, and $2.0R_0^{DD}$. Note different time scales.

For the next series of simulations, we discuss the HEX morphology. Because the we find that the cylinders show the same concentration based trends as spheres, we omit discussion on concentration dependence for the HEX phase and instead focus on how changing features sizes and volume fractions affect trapping kinetics. We varied the cylinder radius, r_{cyl} and spacing between cylinder centers, s, to

explore the importance of these dimensions. All morphologies were generated such that the number density of donors and traps within each domain was kept constant. We simulated three cases: (1) cylinders where both the size and spacings were varied, but in such a manner such that the volume fraction of donors and traps were maintained equal ($\phi_D = \phi_T$) as for the BCC spheres, (2) cylinders of constant size but with their center to center spacings varied, (3) cylinders with constant center to center spacing but with their sizes varied. For the second two cases ϕ_D and ϕ_T vary with the varied parameter s or r_{cyl}.

For Case 1, cylinders were simulated such that $\phi_D = \phi_T$ and $C_D = C_T = 1$ (Figure 4.9a and b) but with r_{cyl} and s simultaneously varied, analogous to the BCC spheres. For small cylinders ($r_{cyl} \lesssim 0.5R_0^{DD}$), $G^D(t)$ and MSD are not seen to change noticeably as a function of cylinder size; the lines for $r_{cyl} = 0.1$ and $0.5R_0^{DD}$ fall on top of one another for $G^D(t)$ and MSD. Just as with the BCC phase, when comparing identical HEX cylinders with donors inside vs. outside, we see observe nearly identical $G_D(t)$ and MSD for small cylinders ($r_{cyl} < R_0^{DD}$) but again these features diverge as the cylinder size increases. As before the larger cylinders with donors inside have larger MSD and more slowly decaying $G^D(t)$ than cylinders with donors in the inter-cylinder domains.

In an effort to analyze these results further and elucidate the differences in the HEX phase with very small features, we determined the locations of trapped

excitons relative to the Voronoi cells of the HEX lattice. Towards this objective, Voronoi cells were constructed by defining cell edges that are equidistant between two cylinder centers. The first Voronoi cells is defined by the nearest-neighbor cylinders and the second Voronoi cell is defined by the second-nearest-neighbor cylinders. The fraction of excitons trapped within the first and second Voronoi cells, $\phi_{Voronoi}$, increases with increasing cylinder radius and increasing unit cell size (Figure 4.9c). Even for the small cylinders where the $G^D(t)$ and MSD were nearly identical, $\phi_{Voronoi}$ is clearly distinguishable. For larger cylinders, where $G^D(t)$ decays more slowly and the plateau value of MSD increases with increasing cylinder radius, $\phi_{Voronoi}$ approaches 1 for the first Voronoi cell. At a given cylinder radius, $\phi_{Voronoi}$ is smaller for cylinders with traps inside because the excitons have a pathway through the continuous donors domain to escape the Voronoi cell. In contrast, for cylinders with donors inside, escaping the Voronoi cell would require the exciton to make a single large jump beyond the edge of the donor domain in order to either reach another cylindrical donor domain or reach a trap outside of the Voronoi cell.

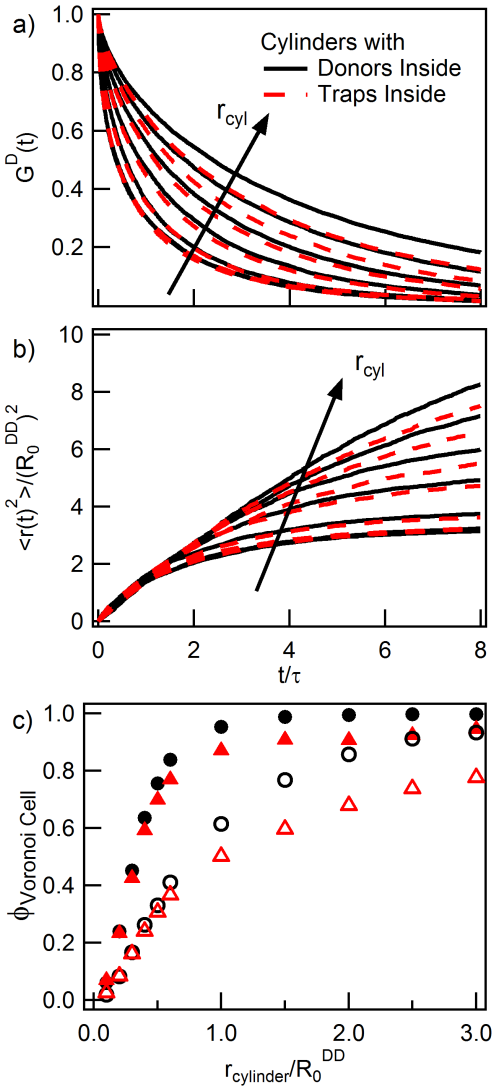

Figure 4.9: a) $G^D(t)$ and b) MSD for cylinders with donors inside (black solid) and traps inside (red dashed) of radius r = 0.1, 0.5, 1.0, 1.5, 2.0, 2.5, and $3R_0^{DD}$ where $\phi_D = \phi_T$. The arrows show the direction of increasing cylinder size. c) Fraction of trapped excitons within the first (empty) and second (solid) Voronoi cells of the HEX cylinders for cylinders with donors inside of cylinders (black circles) and traps inside of cylinders (red triangles).

In Figures 4.10 and 4.11, we display the free an trapped exciton distributions at $t = \tau$ to demonstrate the manner in which the cylinder size affects trapping positions (Figures 4.10 and 4.11). Untrapped and trapped excitons appear to be distributed uniformly in the donor and trap domains for cylinders that are small relative to R_0^{DD}. As the cylinder size increases, it becomes more difficult for an exciton in a larger donor domain to reach the trap domains and hence the overall density of trapped excitons decreases and correspondingly the density of untrapped excitons increases. For cylinders large relative to R_0^{DD}, trapped excitons cluster near interfaces and leave a depleted region of untrapped excitons next to the interface. The enhanced concentration of trapped excitons and the depleted region of untrapped excitons near interfaces was also seen for the lamellar exciton distributions discussed above (Figure 4.5).

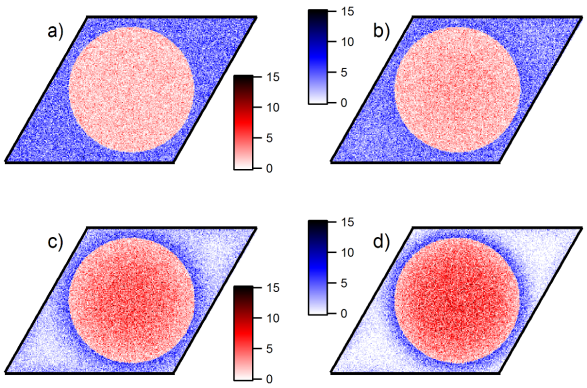

Figure 4.10: Exciton distributions at time $t = \tau_D$ for HEX cylinders with radii of a) 0.1, b) 1, c) 2, and d) $3R_0^{DD}$ where $\phi_D = \phi_T$. The cylinders are filled inside with donors (red) and have traps (blue) in the surrounding space. The color scale bars show the relative number density of excitons (arbitrary units).

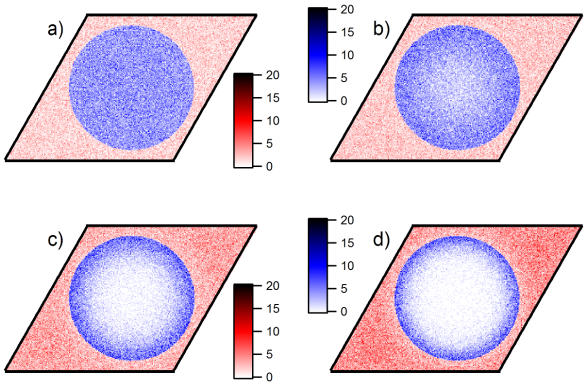

Figure 4.11: Exciton distributions at time $t = \tau_D$ for HEX cylinders with radii of a) 0.1, b) 1, c) 2, and d) $3R_0^{DD}$ where $\phi_D = \phi_T$. The cylinders are filled inside with traps (blue) and have donors (red) in the surrounding space. The color scale bars show the relative number density of excitons (arbitrary units).

Interestingly, the short time-scale behavior of the MSD is different for cylinders (and BCC spheres) compared to that of for lamellae (Figure 4.12). The MSD(t) increases monotonically with lamellae width for all times on the time scale of the simulation. Whereas for the cylindrical morphologies, MSD(t) is smaller for larger cylinders for small times ($t \lesssim \tau$) and crosses over to larger values for larger cylinders at large t. While the data shown in Figure 4.12a are for cylinders with donors inside, the behavior is representative of the trends seen for cylinders with traps inside, and also for BCC sphere geometries of both types.

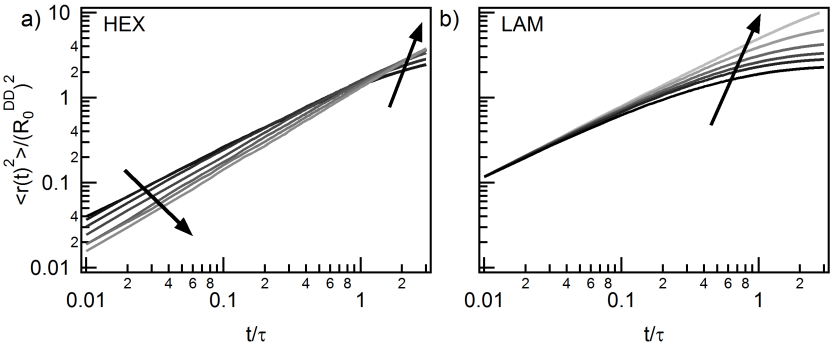

Figure 4.12: MSD of a) cylinders (donors inside) and b) lamellae of increasing domain size (black to grey). Cylinders range from $r_{cyl} = 0.1$ to $3R_0^{DD}$ and lamellae range from d =0.5 to $5R_0^{DD}$. The arrows show the direction of increasing domain size. The MSD exhibits different behavior on short time scales for cylinders and lamellae.

Within the HEX phase, we also wish to understand how exciton trapping changes if we relax the requirement of equal volume fractions. For Case 2, we set the cylinder radius to $r_{cyl} = R_0^{DD}$ for cylinders containing donors. As can

be seen in Figure 4.13, increasing s from 2 to $4R_0^{DD}$ causes $G_D(t)$ to decay more quickly and MSD to decrease. However increasing s further to 6 and $8R_0^{DD}$ did not appreciably change $G^D(t)$ and the mean square displacement. Such results can be understood by noting that small spacings result in a trap-limited regime in which the narrow trap domains surrounding the cylinders serves as a bottleneck to harvesting excitons (e.g. when $s = 2R_0^{DD}$, the cylinders are touching). Increasing the spacing beyond $s > 4R_0^{DD}$ does not lead to an increased trapping rate, since the trap domain surrounding each cylinder is larger than the extent of the region where excitons are trapped and the transfer among donors between cylinders becomes negligible. The transfer rate has an inverse one sixth dependence on distance so trapping events over distances longer than a few R_0^{DD} are rare. The mean square displacement of excitons in the plane normal to the cylinders for cylinders with $s > 4R_0^{DD}$ is also seen to be constant and plateaus to $1.89(R_0^{DD})^2$. Therefore the root mean squared displacement is $1.4R_0^{DD}$ which corresponds to a value larger than r_{cyl}, but less than the edge-to-edge distance of the cylinders. When the cylinders are touching, the root MSD is ($> 2.3R_0^{DD}$), which is larger than twice r_{cyl} and is consistent with the transfer of excitons between the cylinders before being trapped.

For Case 3, the cylinder sizes are varied while holding the center-to-center spacing constant ($s = 1.67R_0^{DD}$) and we observe that the trapping behaviors de-

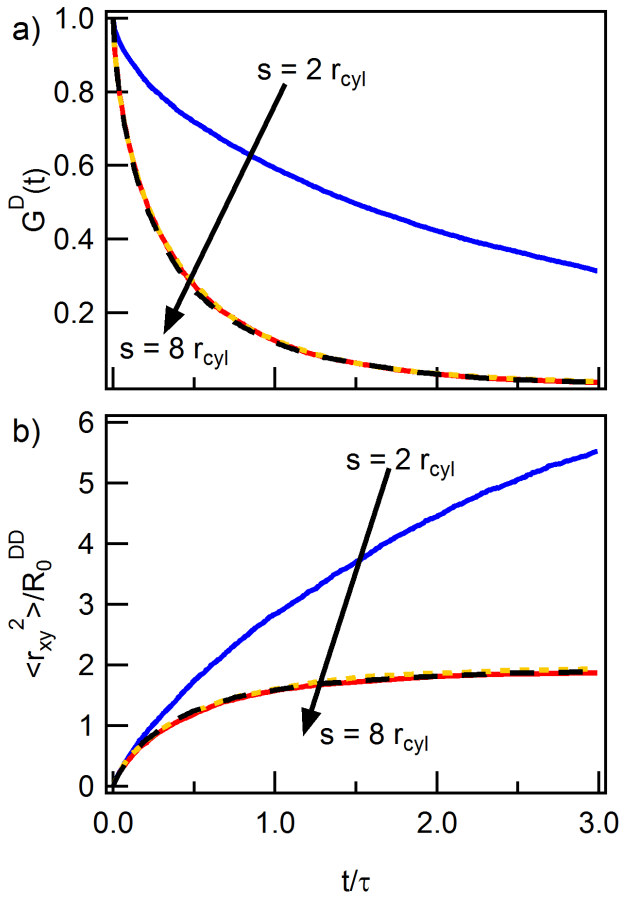

Figure 4.13: Simulation results for HEX cylinders with constant radius ($r = R_0^{DD}$) and but varying spacings, s. The spacings between cylinders varied from s = 2 to $8R_0$. a) $G_D(t)$ and the b) mean square displacement in the plane of the cylinders.

pends not only one cylinder size by also on whether the donors or traps are inside the cylinders (Figure 4.14). For cylinders with donors inside, increasing r_{cyl} from 0.3 to $1.67R_0^{DD}$ causes MSD to increase and $G^D(t)$ to decay more slowly. In contrast, when the traps are inside the cylinders, increasing r_{cyl} from 0.3 to $1.67R_0^{DD}$ causes MSD to decrease and $G^D(t)$ to decay more rapidly. These competing effects of increasing r_{cyl} on MSD and $G^D(t)$ can be rationalized as a consequence of the changes to the donor domain volumes. Excitons starting in smaller donor domains are more easily trapped due to increasing proximity of traps. When donors are placed inside cylinders, the donor domains increase in size with increasing r_{cyl}, whereas when the donors are place outside cylinders, the donor domains decrease in size with increasing r_{cyl}.

Thus we can conclude that $G^D(t)$ and MSD behave similarly for HEX cylinders, BCC spheres and lamellae as long as volume fractions of donors and traps are kept equal. However, changing cylinder size or spacing in a way that changes the volume fractions alters the the trapping kinetics of the excitons.

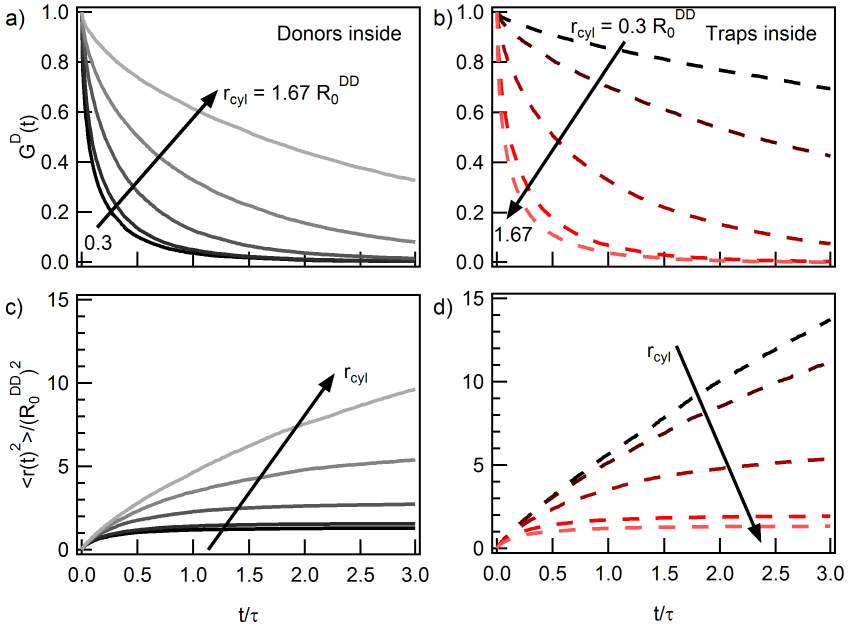

Figure 4.14: Simulation results for HEX cylinders with constant spacing ($s = 1.67R_0^{DD}$) and radius, r_{cyl} = 0.3, 0.5, 1.0, 1.5, and $1.67R_0$. $G_D(t)$ (MSD) for cylinders with a(c) donors inside and b(d) traps inside. The arrows show the direction of increasing cylinder radius.

4.4.3 Förster Transfer in Bicontinuous Phases - Gyroid and Microemulsion

Bicontinuous morphologies are particularly interesting in materials science because of their potential utility for facilitating simultaneous transport of two different species through the bicontinuous domains.

In our work, as input morphologies for the simulations we use a gyroid phase morphology of an AB diblock copolymer and the bicontinuous phases calculated

for an AB + A + B ternary blend of diblock copolymer and homopolymers. Donor and trap regions were distributed according to the density fields to create equal volume fractions of donors and traps with sharp interfaces. To minimize finite size effects, the calculated unit cells (Figure 4.1d and e) were scaled from 1 to $50R_0^{DD}$ to change domain sizes and tiled so that the simulation cell was $> 10R_0^{DD}$.

Figure 4.15 shows the results for $G^D(t)$ and MSD for bicontinuous morphologies. Similar to the other morphologies discussed, increasing the domain sizes slows the trapping ($G^D(t)$) and increases MSD.

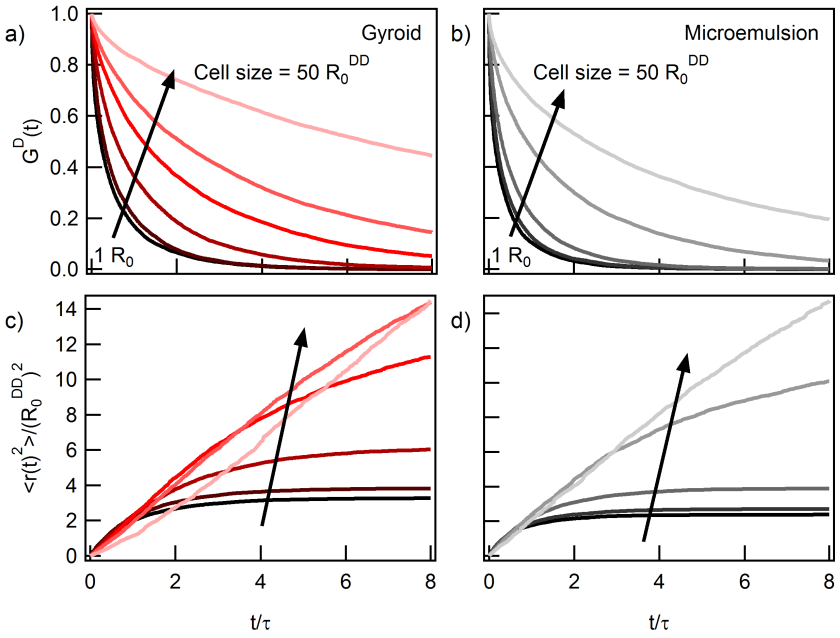

Figure 4.15: $G^D(t)$ and MSD for Gyroid (a, c) and a Microemulsion (b,d) for different sizes of unit cells, scaled from $1R_0^{DD}$ to $50R_0^{DD}$ (dark to light, 1, 5, 10, 17.5, 25, $50R_0^{DD}$) in order to change the domain sizes.

4.5 Morphological Dependence of Trapping Kinetics

Since there are no prior exact analytical solutions for the inhomogeneous distributions of donors and traps studied here, it is of interest to identify the features of the morphology which control the trapping behavior. For this objective, simulations of all morphologies (Lam, BCC, HEX, Gyroid, Microemulsion, and 2D and 3D checkerboards) were performed at two concentrations: $C_D = C_T = 1$ and $C_D = C_T = 10$ and the initial trapping rate was determined from fitting an exponential function to the first part (initial $t < 0.08\tau$) of the $G^D(t)$ curve for each simulation condition. To supplement the particular morphologies studied, 2D and 3D checkerboard structures were also simulated (3D checkerboard shown in Figure 4.1f). The dependence of the trapping rate was correlated to the domain volumes, surface areas, average distance to trap region, and surface area to volume ratios of the different morphologies to identify the main governing parameters.

Overall, the exciton trapping behavior (initial trapping rate) is best parametrized by the surface area to donor volume ratio (SA/V_{donor}) of the morphology.The initial trapping rate data from simulations, where $\phi_D = \phi_T$, collapses well onto a single curve when plotted against SA/V_{donor}, as shown in Figure 4.16. The data shows two regimes: (1) a linear regime (slope on the plot of ~ 1) where

the trapping rate increases with increasing SA/V; and (2) a flat regime where the rate plateaus above a certain SA/V. The transition happens at a slightly larger SA/V_{donor} for the higher concentration (~ 6.2) than for the lower concentration data (~ 3.7).

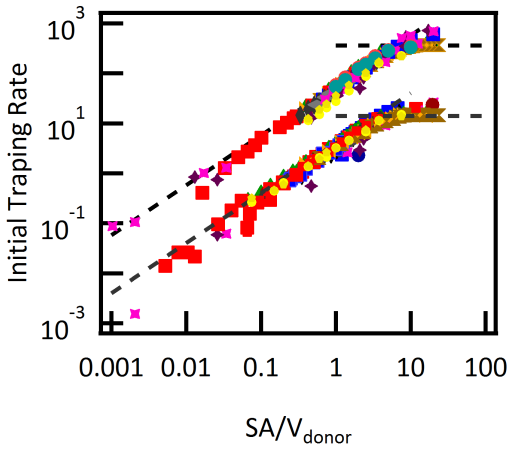

Figure 4.16: The initial trapping rate plotted vs. the ratio of surface area to donor domain volume for a variety of morphologies for two concentrations, $C_D = C_T = 1$ (lower data set) and $C_D = C_T = 10$ (upper data set). The dashed horizontal lines represent the trapping rate in a homogeneously mixed donor-trap system with the corresponding concentrations. The other dashed lines, meant to guide the eye, have a slope of 1.

In order to better characterize the trapping behavior and relate it to SA/V_{donor}, $G^D(t)$ for all morphologies was also fit with a stretched exponential function

$$G^D(t) = exp[-(At)^{\beta}]. \tag{4.3}$$

The A parameter describes the rate of the trapping and the beta parameter is generally related to the dimension of the confined energy transfer system.[99,100] The parameters A and β were extracted from fitting $G^D(t)$ and plotted against surface area to volume ratio (Figure 4.17a and b). Again, we observe a collapse of A and β parameters as a function of SA/V_{donor}. The A parameter shows similar behavior to the trapping rate, with a slope of ~ 1.5 for low SA/V_{donor}. Both A and β plateau above a SA/V_{donor} of ~ 6 for the higher concentration and ~ 3.5 for the lower concentration data.

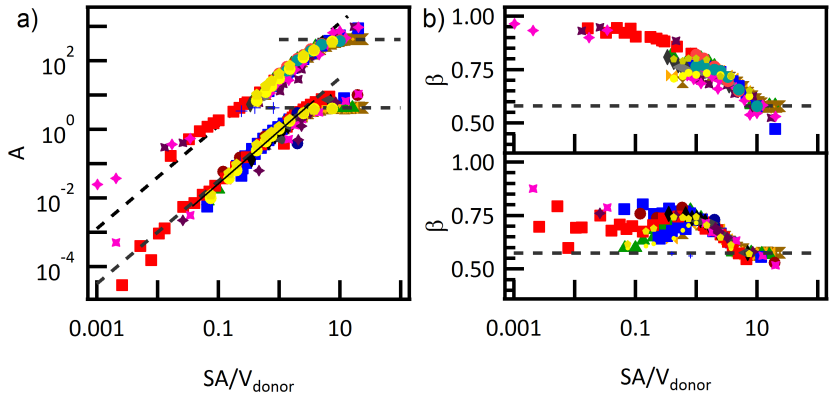

Figure 4.17: The (a) A and (b) β fitting parameters plotted vs. the ratio of surface area to donor domain volume for a variety of morphologies for two concentrations, $C_D = C_T = 1$ (lower data set) and $C_D = C_T = 10$ (upper data set). The dashed horizontal lines represent the value of the A parameter β parameter in a homogeneously mixed donor-trap system with the corresponding concentrations. The other dashed lines, meant to guide the eye, have a slope of 1.5.

To understand the behaviors seen in our results, below we provide some simple arguments for how the trapping rate scales with SA/V in (1) the linear regime ($SA/V_{donor} \lesssim 1$ with slope of $\sim$1) and (2) the flat regime ($SA/V_{donor} \gtrsim 1$).

4.5.1 Regime 1: Reaction Controlled Trapping

In the linear regime ($SA/V_{donor} \lesssim 1$), the slope of the trapping rate (Figure 4.16a) is consistent with a reaction controlled process where diffusion of excitons is fast and the trapping rate is controlled by the rate, r_{trap}, of excitons hopping across the interface between a uniformly distributed donor region and a spherical trap region of radius, R. In such a situation, the rate of the reaction is proportional to the probability that an exciton is in the interfacial region around the trap region, P_I.

$$r_{rxn} \propto P_I r_{trap}. \tag{4.4}$$

The probability, P_I is given by $\frac{V_{interface}}{V_{donor}}$, where $V_{interface}$ is the volume of the interfacial region (volume within distance R_0^{DT} of trap domain) and V_{donor} is the total volume of the donor domain. As a consequence, P_I scales as

$$P_I \sim \frac{R_0^{DT} 4\pi R^2}{V_{donor}} \sim \frac{R_0^{DT} SA}{V_{donor}}. \tag{4.5}$$

Substituting P_I from Eq. 4.5 into Eq. 4.4, we find that

$$r_{rxn} \propto \frac{SA}{V_{donor}} r_{trap} \tag{4.6}$$

meaning that the overall trapping rate is directly proportional to the ratio of surface area to donor domain volume, SA/V_{donor}. These arguments rationalize the slope of 1 on the log-log plot in Figure 4.16a.

4.5.2 Regime 2: The Uniformly-Mixed System

In the flat regime of the trapping ($SA/V \gtrsim 1$), the constant trapping rate is consistent with that of the uniformly, randomly mixed system. As the domain sizes become small relative to the Förster transfer radii, the system approaches the homogeneously mixed limit and the trapping rate asymptotes to a value consistent with the GAF systems.

The magnitude of the plateau is however dependent on volume faction. When $\phi_D = \phi_T$, the rate plateaus at the same trapping rate as for the randomly, uniformly distributed donor/trap case ($C_D = C_T = 1$ or $C_D = C_T = 10$), corresponding with donor domains that are on the order of or smaller than the Förster radius. When the volume fractions are not equal, the value of the trapping rate varies, as one would expect in a uniformly mixed system where $C_D \neq C_T$.

4.6 Conclusion

We have used KMC simulations to examine energy transfer in several inhomogeneous donor-trap systems that are inaccessible by a direct analytical approach. Using the simulations, we studied time-dependent Förster transport and trapping among donors and traps organized into lamellae, 2D and 3D checkerboard structures, body-centered cubic spheres, hexagonally packed cylinders, gyroid morphologies, and microemulsions. Based on our simulations, we determine that the most relevant geometrical parameter controlling these systems is the SA to V_{donor} ratio. Such a parameter is seen to correlate with the initial trapping rate and stretched exponential fitting parameters to trapping.

4.7 Simulation Notes

Simulation cells between 4 and $100R_0^{DD}$ were used with periodic boundary conditions and the minimum image convention. The number of wraps around the simulation cells was recorded for calculating the total mean square displacement.

A binary search was implemented to select each event (2) for fast searching, and binary trees were created only as needed for each step to conserve time and memory.

Inverse Transform Sampling: Inverse transform sampling is a method for generating random numbers from an arbitrary distribution, $f(x)$, using its inverse cumulative distribution function, $F^{-1}(x)$. For broadened interface studies, inverse transform sampling, with an inverse cumulative distribution function of $F^{-1}(x) = 1/2ln(exp(2x) - 1)$, was used to distribute donors and traps to a create a concentration gradient at the interface according to a hyperbolic tangent function.

Surface Area and Volume: The surface areas and domain volumes for lamellae, spheres, cylinders, and checkerboard structures were calculated based on geometry. The surface areas for gyroids and microemulsions were calculated using built-in MATLAB functions.First the isosurface was approximated, and then its surface area was determined. The domain volumes were simply approximated by counting the fraction of voxels that contained donors or traps, and scaling by the total volume.

Chapter 5

Simulations of Dye Sensitized Solar Cells: Improving Energy Relay Dyes for Dye Sensitized Solar Cells by Increasing Donor Homotransfer

5.1 Introduction

Dye sensitized solar cells (DSCs) have reached high efficiencies ($> 10\%$)[2] for single-dye, single-junction cells. However, the maximum attainable efficiency for a single-junction dye cell with a loss in potential due to an I^-/I_3^- electrolyte is estimated to be only 13.8% (or 20.3% for a cell with an electrolyte with a very optimized potential[1]).[132] In order to improve efficiency beyond the predicted limits, additional strategies are being explored, such as increasing the range of absorption

[1]Assuming an optical bandgap of 1.41 eV with full absorption at all energies below the bandgap and a very small loss in potential of only 0.4 eV with high fill factor and IPCE.[132]

across the solar spectrum by using multiple absorbing materials. Using two dyes instead of one has several advantages over attempting to cover the solar spectrum with a single dye. Firstly, it is more difficult to identify a single dye with a very broad absorption as opposed to two dyes with moderately broad, complementary absorptions. Secondly, there is a trade-off between a broadened absorption spectrum and the oscillator strength and thus the absorption of a molecule at a given wavelength. By using two molecules instead of one, each with a less broad absorption, ease of selection and a high oscillator strength can be maintained resulting in stronger absorption. One option for incorporating two dyes is to construct tandem solar cells, in which multiple junctions are connected in series in order to absorb different regions of the solar spectrum.[133,134] Each junction functions as a regular DSC by employing a strongly light-absorbing sensitizing dye, which is adsorbed to mesoporous titania, to collect photons from the solar spectrum. The excited state of the dye molecule injects an electron into the titania, leaving behind a hole on the dye. An electrolyte or hole transporting material then regenerates the dye. Two alternatives to such tandem cells, which take advantage of a wider portion of the solar spectrum, but maintain ease of fabrication involve either adding a second, co-sensitizing dye adsorbed to the semiconductor, or adding separate energy relay dyes (ERDs) to the electrolyte solution.[10] The co-sensitizing strategy has led to a record DSC performance of 12.3%,[9] but is limited by the absorption coefficients

of the dyes and the available surface area to which they can adsorb. The relay dye strategy, which we discuss in this work, allows for better absorption of light due to the ability to dissolve more dye in the electrolyte solution, but introduces the additional requirement that the relay dye can Förster energy transfer efficiently to the sensitizing dye.

Currently, the use of energy relay dyes is emerging as a popular approach to improve performance in dye sensitized solar cells,[10,12–16,118–123] reaching efficiencies up to 4.5%.[12] Energy relay dyes, which are generally dissolved in the electrolyte rather than absorbed to the nano-porous semiconductor, absorb light in a region of the solar spectrum not utilized by the main sensitizing dye, generate an excited state, and then energy transfer to the main sensitizing dye where the exciton generates usable charges. The exciton transport processes compete with exciton decay and exciton quenching by other species in the electrolyte. Exciton decay typically occurs with a characteristic exciton lifetime, τ_0, which is on the order of nanoseconds for successful relay dyes.[11] Dynamic exciton quenching, which can be significant, depends on the interaction of species in the electrolyte with the relay dye.

Förster resonant energy transfer has been analyzed for DSCs by Hoke and McGehee, who calculated exciton transfer efficiencies (ETEs) from donor relay dyes to acceptor sensitizing dyes in spherical and cylindrical nanopores.[135] They

found that reaching high exciton transfer efficiencies required either (1) relay dyes with large Förster transfer radii to the sensitizing dye, and possessing short exciton lifetimes so that quenching by other species in the electrolyte would not interfere with the FRET processes or (2) relay dyes that were not quenched by the electrolyte and had very long exciton lifetimes so that mass diffusion of the dye in solution could aid in exciton transport. They found that for (1), they could characterize the ETE with a single parameter, $R_C/(2R_P)$, where R_P denotes the the pore radius and R_C is a length given by

$$R_C = \left(\frac{C_A R_0^6}{1 + \tau_0 \sum_j k_{q_j} [Q_j]} \right)^{1/4} \tag{5.1}$$

where C_A is the surface acceptor concentration, τ_0 is the lifetime of the excited state, k_{q_j} is a bimolecular quenching coefficient, and $[Q_j]$ is the concentration of the quencher j.[135] We use this length scale in our discussion later.

The large Förster radius required for a high ETE is a rather restrictive requirement for relay dye selection, making it difficult to find good relay-sensitizing dye pairs. However, it may be anticipated that using dyes with significant donor homotransfer would be key to further improve exciton transfer efficiencies from the relay dye to the sensitizing dye. Although Hoke et. al. accounted for energy transfer, exciton lifetime, quenching, and diffusion, they assumed that donor ho-

motransfer amongst the relay dye was a negligible process,[135] which is expected to be reasonable for a small donor homotransfer radius, R_0^{DD}. In this work, we use Kinetic Monte-Carlo (KMC) simulations to explore how donor homotransfer influences ETE in cylindrical pores as a function of Förster transfer radii, relay dye concentration, exciton quenching, and pore size. Based on our results, we suggest strategies for improving the design of ERDs for DSCs.

5.2 Simulation Methods

In this work we use Kinetic Monte-Carlo simulations, which along with ordinary Monte-Carlo simulations have proven useful in understanding and modeling excitation and charge transport in organic materials,[136–145] to explore donor homotransfer among energy relay dyes. The simulation accommodates four processes: energy homotransfer between donors (relay dyes), energy transfer from a donor (relay dye) to an acceptor (sensitizing dye), exciton decay, and dynamic quenching of the exciton (photoluminescence quenching). All rates in the simulation are normalized by the exciton lifetime, τ_0. The rates of the resonant energy transfer processes are given by

$$k_F = \frac{1}{\tau_0}\left(\frac{R_0}{r_{ij}}\right)^6, \text{ or normalized by } \tau_0,\ k_F^* = \left(\frac{R_0}{r_{ij}}\right)^6. \tag{5.2}$$

where r_{ij} is the distance between dye molecules, τ_0 is the exciton lifetime, R_0 is the Förster transfer radius.[130,131] The Förster transfer radii, R_0^{DD} and R_0^{DA}, are denoted with superscripts for donor homotransfer and donor-to-acceptor heterotransfer, respectively. The simulation neglects diffusion of the dye molecules, and as such, is most applicable in cases where the energy transfer happens on a much shorter time scale than the diffusion of the dye molecules. For example, the simulations apply to DSCs containing relay dyes with short lifetimes relative to the timescale of diffusion or to solid state dye sensitized solar cells (ss-DSCs) where the relay dye is dispersed in a solid rather than a liquid. Diffusion improves exciton transfer to the sensitizing dye[135] so if diffusion did occur on a relevant time scale, neglecting it in the simulations underestimates the efficiency, thereby giving a conservative result.[2] The total rate of collisional quenching is given by

$$k_Q = \tau_0 \sum_j k_{qj}[Q_j] \tag{5.3}$$

where k_{qj} is the rate of quenching by species j and $[Q_j]$ is the concentration of the quenching species.[146] For example $\sum_j k_{qj}[Q_j]$ for a I^-/I_3^- electrolyte in a typical DSC is 5×10^9 s^{-1} and for a typical τ_0 of 1 nanosecond, k_Q would be 5.[135] Static quenching, which is especially important for high concentration dyes,[16] is not

[2]Assuming a diffusion constant of 0.6 nm^2/s,[135] a dye molecule would on average only diffuse ~ 2 nm during the ~ 1 ns lifetime of the dye, and is therefore negligible on the time and length scales considered.

treated in these simulations, except that it is inherently present in the fluorescence quantum yield of the dye, which is accounted for in the Förster transfer radius. Dye aggregates resulting in static quenching may act as trap sites for excitons in a donor homotransfer transport scheme and therefore care should be taken to avoid selecting dyes with a propensity to aggregate or otherwise statically quench when fabricating a DSC with an ERD. Design strategies are discussed *ex infra*. In solid state systems there may be preferred migration to particular sites due to the migration of excitons in a distribution of molecular sites with different dipolar environments. Our simulation does not treat the possibility of exciton diffusion to preferred sites and treats the sites as essentially having a narrow energetic distribution.[147]

The exciton transfer efficiency (ETE) is given by the fraction of excitons reaching a sensitizing dye before they decay or are quenched. There are two ways for the exciton to reach the sensitizing dye; it can either energy transfer directly to the sensitizing dye or it can transfer from relay dye molecule to relay dye molecule until it reaches a sensitizing dye molecule, (a schematic of the processes are shown in Figure 5.1). We especially wish to understand the importance of the latter process in exciton collection.

In order to mimic titania nanopores with realistic parameters, simulations were carried out in a cylindrical pore geometry with a cylinder radius of 15 nm and

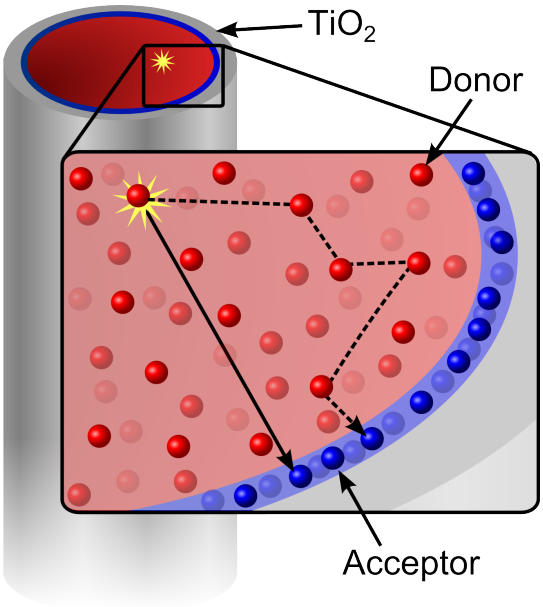

Figure 5.1: A schematic of a cylindrical pore in a dye sensitized solar cell with the sensitizing dye (blue) absorbed to the cylinder's surface and a relay dye (red) in the electrolyte solution filling the pore volume. An exciton generated on the relay dye can either energy transfer directly to the sensitizing dye (solid line) or transfer between relay dye molecules until it reaches a sensitizing dye molecule (dashed line).

a concentration of 0.5 sensitizing (acceptor) dye molecules/nm^2 adsorbed to the cylinder surface. Two relay (donor) dye concentrations of 0.006 and 0.06 relay dye molecules/nm^3 (10 and 100 mM) in the cylindrical pore were simulated with Förster transfer radii, R_0^{DD} and R_0^{DA}, varied from 0 to 10 nm. Exciton transfer efficiency was determined for each set of parameters. Hoke et. al. found that energy transfer in nano-cylinders and nano-spheres showed similar trends, albeit with slightly different numerical results; therefore, we only simulate nano-cylinders in this work.

Exciton transfer efficiency for different parameters was determined using a Kinetic Monte Carlo (KMC) simulation. We simulated four possible events (1) exciton transfer from a donor to an acceptor, (2) exciton transfer from a donor to another donor, (3) exciton decay, and (4) dynamic exciton quenching. The rates for events (1) and (2) were calculated from Equation 5.2, the rate for (3) is based on the exciton lifetime, τ_0, and the rate for (4) was calculated from Equation 5.3. The simulation parameters were the Förster radius for donor homotransfer, R_0^{DD}, the Förster transfer radius for transfer from donor to acceptor, R_0^{DA}, donor concentration, C_D, acceptor concentration, C_A (held constant at 0.5 chromophores/nm^2), total quenching rate, k_Q, and pore radius (R_P). The simulation used periodic boundary conditions with a minimum image convention in the direction of the axis of the cylinder. Donor dye molecules were randomly distributed in the pore volume and acceptor dye molecules were randomly distributed on the pore surface.

5.3 Results and Discussion

First we discuss the results for the case without donor homotransfer. Figure 5.2 (inset) shows the simulated ETE for such a case compared with the analytical solution[135] for the corresponding unitless parameter, $R_C/(2R_P)$, for simulations

with and without exciton quenching ($k_Q = 5$ and $k_Q = 0$, respectively). The simulations match well with the analytical solution (ΔETE < 0.04) and indicate the applicability of our simulation methodology.

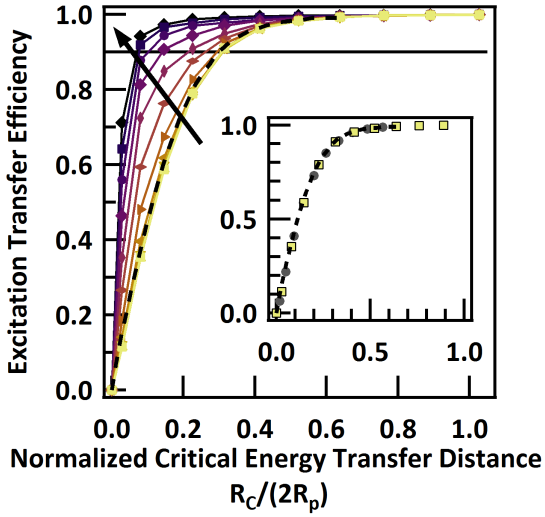

Figure 5.2: The exciton transfer efficiency with donor homotransfer for increasing R_0^{DD} ($R_0^{DD} = 0$, 1, 2, 3, 4, 5, 6, 7, 8, 9, and 10 nm) and all other parameters held constant ($C_D = 0.006$ relay dye molecules/nm^3, no quenching). The inset shows exciton transfer efficiency with no donor homotransfer from simulations with quenching ($k_Q = 5$) (grey circles) and without quenching (yellow squares) plotted with the analytical solution[135] (dashed black line) for the corresponding parameters. The horizontal solid black line indicates 90% ETE.

Overall, including donor homotransfer in the simulation is seen to improve the ETE. The effect of increasing R_0^{DD} ($C_D = 0.006$ molecules/nm^3, no quenching) from 0 to 10 nm is shown in Figure 5.2. For small increases in R_0^{DD} (from 0 to 3 nm), the ETE remains essentially the same (the increase in ETE is less than 0.04). As R_0^{DD} increases beyond 3 nm the ETE is seen to improve, exceeding 0.9

at $R_C/2R_P$ as small as 0.05 (with no quenching this corresponds to $R_0^{DA} \sim 2$ nm). With the donor homotransfer included in the simulation, $R_C/2R_P$ is no longer the only characteristic length scale so from here on we report data as a function of R_0^{DA} and R_0^{DD} in units of nanometers.

The ETE enhancement due to donor homotransfer is seen to display a strong dependence on C_D. Contour plots of ETE for $C_D = 0.006$ molecules/nm^3 (0.06 molecules/nm^3) are shown in Figure 5.3a(b). The most improvement to ETE (such that ΔETE > 0.1) is seen for systems with low to moderate donor-acceptor transfer ($R_0^{DA} \approx 2.7$ to 4.4 nm (0.5 to 4.1 nm)) and moderate to high donor homotransfer ($R_0^{DD} > 3.7$ nm (2.1 nm)). For $R_0^{DD} = 5$ nm, a high ETE of 0.9 can be achieved with R_0^{DA} as low as 4.3 nm (1.5 nm). Systems with larger R_0^{DA} showed less improvement with added donor homotransfer due to the already high ETE. Figure 5.3d(e) show the change in ETE (ΔETE) caused by the donor homotransfer. The ETE is seen to improve more rapidly with increasing R_0^{DD} for the higher C_D. This observation is consistent with an increased rate of diffusion of excitons through the relay dye matrix which has been shown for increasing C_D.[97]

For the cylindrical nano-pore of radius 15 nm, the assumption of negligible contribution from donor homotransfer is valid when $R_0^{DD} \lesssim 3$ nm for C_D =0.006 molecules/nm^3 ($R_0^{DD} \lesssim 2$ nm for C_D =0.06 molecules/nm^3). For larger R_0^{DD}, enhancement to the exciton transfer efficiency is fairly significant. Given an R_0^{DA}

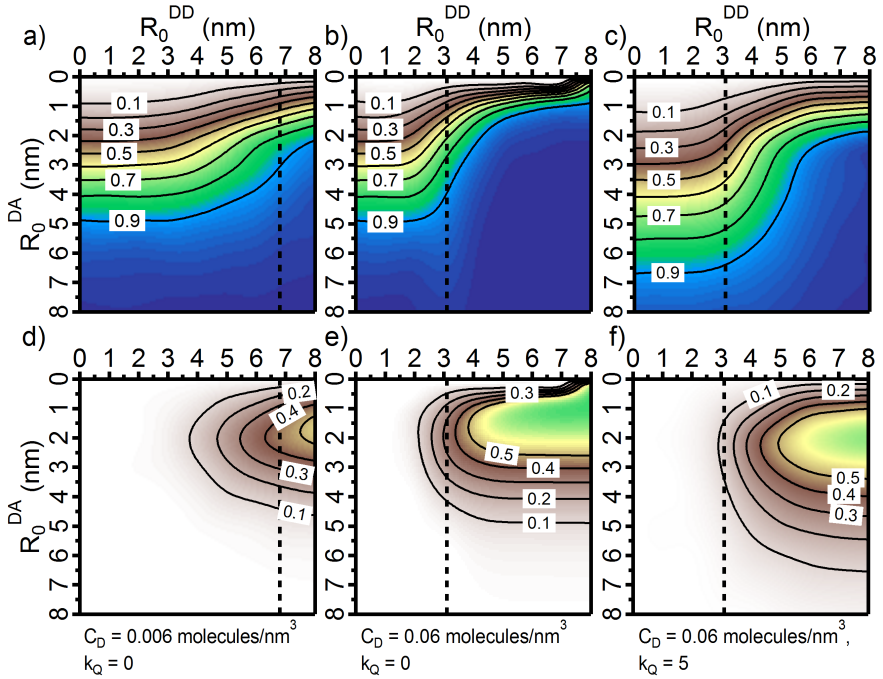

Figure 5.3: A contour plot of (a) the exciton transfer efficiency interpolated from the data in Figure 5.2, showing how ETE changes with varying R_0^{DD} and R_0^{DA} in a cylindrical pore of fixed radius, 15 nm, (b) a contour plot of the ETE for identical conditions when C_D is increased by 10×, and (c) a contour plot of the ETE for the higher C_D with quenching added ($k_Q = 5$). Plots (d-f) show the difference in ETE (corresponding to plots (a-c)) between cylinders with no donor homotransfer, and donor homotransfer with the specified R_0^{DD}. The dashed black lines show where R_0^{DD} = the average spacing between relay dye molecules.

of 3.1 nm with no donor homotransfer, ETE = 0.6. An R_0^{DD} of 6.7 nm is required to enhance the ETE by 50% (ETE = 0.9) at the lower concentration, and an R_0^{DD} of 3.6 nm is required at the higher concentration. When R_0^{DD} is small, adding donor-donor transfer has little effect on the ETE. However, when R_0^{DD} exceeds the average spacing between relay dye molecules, the ETE us seen to increase significantly. The inflection point of the contour line at ETE= 0.9 is at R_0^{DD} = 6.8 nm (3.2 nm), corresponding almost exactly to the average distance between relay dye molecules at 6.8 nm (3.1 nm). The blue region of the contour plots (ETE> 0.9 in Figure 5.3) can be thought of as the region of parameter-space where an ERD would be highly efficient. Then it can easily be seen that increasing C_D increases the set of dyes that can be used in a DSC. In order to select an efficient ERD-sensitizing dye pair, the dyes simply need to be selected so that R_0^{DD} and R_0^{DA} are at least as large as the values corresponding to any given point on the 90% contour line.

We have shown that without quenching species present, donor homotransfer amongst relay dyes greatly improves the ETE, especially for higher concentrations of relay dyes. However quenching of excitons on the relay dye by other species present in the electrolyte has been shown to greatly reduce the ETE.[135] To adjust for such processes, we introduced quenching into the KMC simulation to determine its effect on the improvements to ETE from donor homotransfer. Figures 5.3c and f

show how the ETE is affected by quenching ($k_Q = 5$) for the higher concentration of donors. The overall ETE is greatly reduced and the inflection point in the contour lines is seen to occur at a higher value of R_0^{DD} (5.4 nm for the ETE = 0.9 contour line), but the ETE is still improved fairly significantly by the inclusion of donor homotransfer in the simulation (more so than in the simulations with the lower concentration of donors and no quenching). This result suggests that donor homotransfer can be an important mechanism, even in systems with relatively high quenching of the relay dye.

In order to further explore how the exciton quenching influences the improvements to ETE seen with donor homotransfer, we simulated the ETE for three different possibilities with different pore size and rates of donor-to-acceptor transfer, corresponding to (1) $R_P = 30$ nm, $R_0^{DA} = 5$ nm, (2) $R_P = 15$ nm, $R_0^{DA} = 5$ nm, and (3) $R_P = 15$ nm, $R_0^{DA} = 2.5$ nm, with all other parameters held constant (at both donor concentrations with $R_0^{DD} = 4$ nm and also without donor homotransfer) as a function of quenching (Figure 5.4). Again, donor homotransfer is seen to enhance ETE, even when quenching occurs, although as the quenching rate increases the effectiveness of the donor homotransfer at a given set of parameters decreases (ΔETE decreases with increasing k_Q) due to increased competition between exciton diffusion and quenching.

The cylindrical pore of radius 15 nm with $R_0^{DA} = 5$ nm starts with a high ETE of 0.91 (Figure 5.4b). Since the ETE is already nearly unity, including donor homotransfer with $R_0^{DD} = 4$ nm can only increase ETE to 0.96 (ΔETE = 0.05). However, as quenching is increased, the ETE drops, giving an opportunity for donor homotransfer to enhance it (ΔETE is on the order of 0.1). Increasing the cylinder size from 15 to 30 nm (Figure 5.4a) greatly reduces the initial ETE, and consequently allows enhancement from the donor homotransfer, achieving an ETE of 0.84 without quenching (max ΔETE = 0.21). The ΔETE remains large until quenching is very high. Similarly, keeping the cylinder size at 15 nm, but decreasing the $R_0^{DA} = 2.5$ (Figure 5.4c) also greatly reduces the initial ETE, and allows for an improved ETE of 0.9, with an impressive ΔETE of 0.42 caused by donor homotransfer.

5.4 Strategies for Improving Relay Dyes

Typical R_0^{DA} for donor-acceptor chromophore pairs range from about 2 to 9 nm.[93,146] A pair of dyes with $R_0^{DA} > 7$ nm is expected to give an ETE over 0.9, even with high quenching rates. However, a pair of dyes that cover the solar spectrum, where one dye is optimized as a sensitizing dye, and the other is soluble

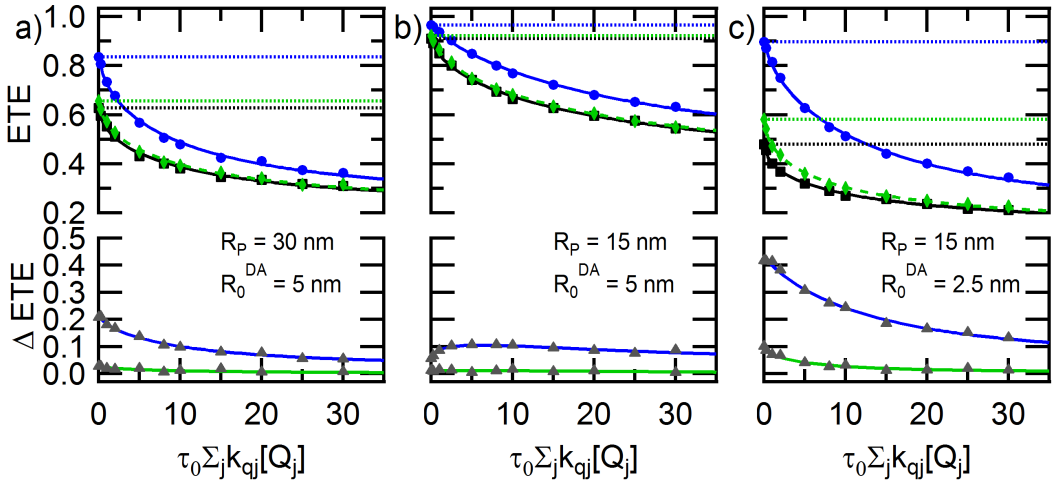

Figure 5.4: Plots of ETE as a function of quenching for cylinders with (a) R_P = 30nm, R_0^{DA} = 5nm, (b) R_P = 15nm, R_0^{DA} = 5nm, (c) R_P = 15nm, R_0^{DA} = 2.5nm for relay dyes with no donor transfer (black squares), donor transfer with R_0^{DD} = 4nm and C_D = 0.006 molecules/nm^3 (green diamonds), and donor transfer with R_0^{DD} = 4nm and C_D = 0.06 molecules/nm^3 (blue circles). The difference between the ETE with and without donor transfer is shown as ΔETE with grey triangles. Fits to the data (black, blue, and green curves) are shown in all plots along with horizontal lines indicating the value of ETE with no quenching (dotted black, blue and green curves).

in the electrolyte may not have quite such a high R_0^{DA}. Below, we discuss how selecting dyes with lower R_0^{DA} could still lead to efficient ETE.

The value of R_0 is related to the overlap between emission and absorbance spectra. If the donor emission strongly overlaps its own absorption (small Stokes shift), then it may not fully overlap the acceptor absorption. Similarly, if the Stokes shift is large enough for the donor emission to strongly overlap the acceptor absorption, it will not overlap its own absorption. An outstanding question is what values of R_0^{DA} and R_0^{DD} can we expect for a pair of dyes that reasonably cover

the solar spectrum and where the donor emission partially overlaps both its own and the acceptor's absorption?

The Förster transfer radius is calculated from

$$R_0^{DA} = \left(8.79 \times 10^{17} \kappa^2 n^{-4} \Phi_D \left[\int \left(\frac{f_D(\nu)\epsilon_A(\nu)}{\nu^4}\right) d\nu\right]\right)^{1/6} \tag{5.4}$$

giving R_0^{DA} in nm when wavenumbers, ν, are given in cm^{-1}.[148] The orientation factor, κ, describes the alignment of the molecular dipoles and is given by $cos\phi_{DA} - 3cos\phi_D \dot{c}os\phi_A$ and $\kappa^2 = 2/3$ for dynamically averaged orientations of D and A.[3] ϕ_{DA} is the angle between the transition dipoles of the molecules, and ϕ_D and ϕ_A are the angles between the vector from D to A and the transition dipoles of D and A respectively. The portion of Equation 5.4 in square brackets is the overlap integral, where $f_D(\nu)$ is the area-normalized donor fluorescence and $\epsilon_A(\nu)$ is the molar extinction coefficient of the acceptor. n is index of refraction of the surrounding material (typically ~ 1.5 in a DSC electrolyte[11]), and Φ_D is the fluorescence quantum yield.

[3]The dynamically averaged case for κ^2 only applies to dipoles rotating rapidly on the time scale of the energy transfer. Dynamic orientation is assumed in our simulation (e.g. for an ERD dissolved in a liquid electrolyte). However, in the isotropically oriented static case, it has been predicted[126] and experimentally verified[149] that a correction factor of 0.8452 must be applied to the time scale of the decay of $G^s(t)$, the probability that the exciton is on the initially excited donor. The decay is always slower in the static case,[126] meaning that it takes longer for an excitation to leave a donor, which suggests that our simulation overestimates the transfer rate and therefore the ETE for fully static donors (e.g. for ss-DSCs).

Donor[a]	Acceptor[b]	R_0^{DA} (nm)	R_0^{DD} (nm)	C_D (mM)	ETE[c]	PCE (%)	reference
PTCDI	TT1	7.9	3.8	13	0.47	3.2	Hardin[11]
DCM	TT1	6.8	3.0	22	0.96	4.5	Hardin[12]
DCM	SQ-1	6.2	2.2	12	0.68	1.6[d]	Mor[15]
N877	SQ-1	5.6	2.5	10	0.32	1.8[d]	Yum[13]
N877	SQ-1	5.6	2.5	10-50	0.14	3.7	Yum[14]
BL302	TT1	5.7	3.1	180	0.70	3.8	Margulis[16]
BL315	TT1	5	2.5	180	0.67	4.1	Margulis[16]

[a,b]The donor dyes are: 4-(Dicyanomethylene)-2-methyl-6-(4-dimethylaminostyryl)-4H-pyran (DCM), perylene-3,4,9,10-tetracarboxylic diimide (PTCDI), a ruthenium complex (N877), and two high-solubility derivatives of DCM (BL302 and BL315). The acceptor dyes are a zinc phthalocyanine dye (TT1) and a squaraine dye (SQ-1). These values of R_0^{DA} and R_0^{DD} were calculated from absorption and emission spectra, extinction coefficients, and quantum yields reported in the literature using Equation 5.4.
[c]ETEs reported in the references. Pore geometries and sizes vary.
[d]Solid-state DSCs.

Table 5.1: The calculated Förster transfer radii of relay dyes and sensitizing dyes used in the experimental literature, along with experimental concentrations and efficiencies.

Most ERDs used in experiments so far have $R_0^{DA} = 5 - 8$ nm and $R_0^{DD} < 4$ nm (Table 5.1), which means the donor-donor transfer does not contribute significantly to the ETE and even with quenching ($\tau_0 \sum_j k_{qj}[Q_j] = 5$) ETE is > 0.8. However DSCs with smaller R_0^{DA} or larger pore size would have much lower ETE and would require larger R_0^{DD} to boost the ETE. The small values of R_0^{DD} are largely due to the lack of overlap and also partly due to comparatively low absorption of the relay dye, although theoretically DCM, BL302, and PTCDI have large enough R_0^{DD} for improvements to ETE to be seen at high concentration with little to no quenching. Selecting dyes with larger R_0^{DD} would require (1) smaller Stokes shift and/or (2) larger extinction coefficients.

How much would the Stokes shift and extinction coefficient need to change to make a significant difference in ETE (e.g. for designing and synthesizing new ERDs) and would the increase in R_0^{DD} due to the reduced Stokes shift outweigh the concomitant decrease in R_0^{DA}? Using the absorption from PTCDI and shifting its emission spectrum to simulate different Stokes shifts, we find that R_0^{DD} can be increased from 3.8 (actual Stokes shift of 50 nm (1.7 eV)) up to 5.6 nm (Stokes shift of 0 nm (0 eV)). With $R_0^{DD} = 5.6$ nm, an ETE of 0.9 can be achieved with R_0^{DA} as low as 1.3 nm without quenching or 3.0 nm with $k_Q = 5$. At $R_0^{DD} = 3.8$ nm, an ETE of 0.9 would require values of R_0^{DA} twice as large (2.8 nm for no-quenching and 6.0 nm for quenching). Even at the lower concentration of donors

with no quenching, R_0^{DA} only needs to be 4.8 or 4.1 nm for R_0^{DD} of 5.6 and 3.8 nm, respectively. Selecting donors with small Stokes shifts decreases the need for a large R_0^{DA}. Additionally, increasing the extinction coefficient by a factor of ϵ' would increase R_0^{DD} by a factor of $(\epsilon')^{1/6}$. For example a threefold increase in extinction coefficient would give a 20% increase in R_0 (increasing the extinction coefficient also increases the overall absorption of light in the DSC). Picking a dye with a smaller Stokes shift (25 nm or 0.08 eV) and a larger extinction coefficient (150000 $M^{-1}cm^{-1}$, closer to the extinction coefficients of good sensitizing dyes) could easily yield a R_0^{DD} $\sim$6 nm,[4] which could easily be used to achieve a high ETE, even with a donor-acceptor pair with relatively poor energy transfer. In fact, several classes of dyes with high R_0^{DD} exist including rhodamines, BODIPYs, phthalocyanines, and squaryliniums, which have R_0^{DD} ranging from 5 up to 7 nm.[150,151] In our calculation, decreasing the Stokes shift of PTCDI to 0 nm reduces the overlap between the emission of PTCDI and the absorption of the commonly paired sensitizing dye, TT1, (see Table 5.1) which would reduce R_0^{DA} but only by less than 1 nm because of the one sixth dependence of Förster transfer radius on the overlap integral in Equation 5.4. From this small change, we can see that decreasing the Stokes shift of the ERD will only have a small effect on R_0^{DA} in most cases. Selecting an ERD-sensitizing dye pair with close, complemen-

[4]Based on calculations for PTCDI with reduced Stokes shift and three times larger extinction coefficient.

tary absorption spectra is ideal both for covering the entire solar spectrum and achieving good R_0^{DA}, so the reduced Stokes shift should not cause problems in a well designed DSC and the improved ETE from enhanced donor homotransfer would more than compensate for any small reduction in R_0^{DA}. In fact having an ERD with a small stokes shift and high rate of homotransfer may actually make it easier to find a suitable ERD-sensitizing dye pair because less spectral overlap is needed since high ETE can be achieved with a much smaller R_0^{DA}.

Most DSCs with ERDs in the literature have relatively low ERD concentrations (Table 5.1) on the order of the lower concentration we simulated (10 mM), largely due to solubility issues. Our results suggests that improving relay dye solubility and thus relay dye concentration in the electrolyte is a route not only to improving the fraction of light absorbed, but also to greatly improving the ETE due to enhancements from donor homotransfer. Experimental attempts to improve dye solubility (up to 180 mM) actually led to lower ETE (dropping from 0.9 for a related donor-acceptor system[12] down to 0.7 for the high-solubility dye), which was attributed to static quenching due to the formation of non-emissive complexes.[16] Minimizing static quenching is particularly important in systems designed for high donor homotransfer because static quenching sites can act as traps for excitons, which could negatively affect ETE. The concept of shielding fluorophores from quenching species using steric hindrance is well known in fluo-

rescence spectroscopy[146] and fluorescent molecules can be engineered to prevent quenching from aggregation using steric hindrance from bulky side groups (which are also useful for solubilizing conjugated molecules) which have been shown to improve fluorescence yield of BODIPYs in solid state films.[152] Another technique to prevent quenching by ions is using electrostatic forces from a charged fluorophore to repel the quencher[5] (e.g. using a fluorescent anion could reduce quenching by the I^-/I_3^- redox couple).[153] Using a charged dye may also help reduce dye aggregation due to electrostatic repulsion and thus reduce static quenching. The results of our simulation suggest that if the static quenching issue for high solubility dyes can be overcome, the increased concentrations of ERD in the electrolyte could boost the ETE.

Recently a great effort has been made to explore new electrolytes for DSCs,[154] and some of these may have the potential to decrease quenching of ERDs. Quenching from a typical I^-/I_3^- redox couple has been reported as $k_{qj}[Q_j] = 5 \times 10^9$ s^{-1} and for the solid-state electron transporting material, spiro-MeOTAD, it is about 2.6×10^7 s^{-1}, based on quenching ratio and PL lifetime reported by Yum et. al.[13] Assuming quenching rates due to electrolytes do not change significantly for different relay dyes, based on these numbers, quenching could be 200 times lower

[5]The quenching constant for quenching of riboflavin phosphate by iodide was reduced by 30% relative to the neutrally charged phosphate when the phosphate had a negative charge (at pH 5 and pH 8, respectively).

in ss-DSCs than quenching in DSCs with typical liquid electrolytes (like those used in most studies of relay dyes so far). Additionally, Cheon et. al. found that using a quasi-solid state electrolyte reduced the quenching of the relay dye relative to a liquid electrolyte.[122] In addition to reduced quenching, using relay dyes in ss-DSCs could lead to another interesting advantages over liquid electrolytes. For example, the hole transporting material spiro-MeOTAD commonly used in ss-DSCs absorbs in the UV and has peak PL emission at 424 nm.[155] Theoretically spiro-MeOTAD could act as a secondary energy relay material and Förster energy transfer to any of the donors in Table 5.1 which can then transfer to the acceptors and enhance the EQE in the UV region of the spectrum. Spiro-TBT, a derivative of spiro-MeOTAD that absorbs in the visible has already been used as a light absorbing material in DSCs.[120]

Now that we have established what is required to achieve a high ETE, the question becomes how much could a relay dye with high ETE improve the efficiency of a DSC? In order to surpass current state-of-the-art single-dye DSCs, which have remarkable panchromatic sensitizers ($\Delta\lambda \sim 600$ nm and PCE $> 10\%$),[156] the sensitizing dye will need to absorb in the red and NIR portion of the solar spectrum, with the energy relay dye filling in the UV and the rest of the visible spectrum. Several NIR sensitizing dyes have recently been developed,[157] some of which have absorption onset past 850 nm.[158–160] For example the sensitizing dye NK-637 has

very strong absorbance between 600 and 900 nm (ϵ_{max} = 146000 $M^{-1}cm^{-1}$).[158] However, the NIR dyes tend to suffer from high losses in potential and thus poor open circuit voltage ($V_{oc} < 0.5$ V) which leads to low efficiencies.

In order to estimate the efficiency of a DSC with relay dye-sensitizing-dye pair, we used a simple model similar to one used by Snaith[132] to estimate theoretical maximum attainable efficiency of a DSC, with the simplifying assumption that the dye will absorb photons at all wavelengths below the absorption onset. For comparison, we repeat the calculation with the main difference being our use of instantaneous rather than gradual absorption onsets. To make results comparable, we used the same fill factor (FF = 0.73) and incident photon conversion efficiency (IPCE = 0.9), and selected a low loss in potential of 0.5 eV. The theoretical efficiency for a single sensitizing dye that absorbs at all wavelengths below the absorption onset is shown in Figure 5.5a. Based on this result for a broadly absorbing single dye, the maximum efficiency of 20.9% occurs at an absorption onset of$\sim$900 nm (the efficiency is slightly higher than that predicted by Snaith because of the sharp absorption onset used in our model, but the wavelength is consistent with that result).

Using this model, we predicted the efficiency of a DSC with both a relay dye and a sensitizing dye. Based on the maximum at 900 nm, we chose to model a sensitizing dye with an onset at 900 nm (an absorption onset at 900 with a loss

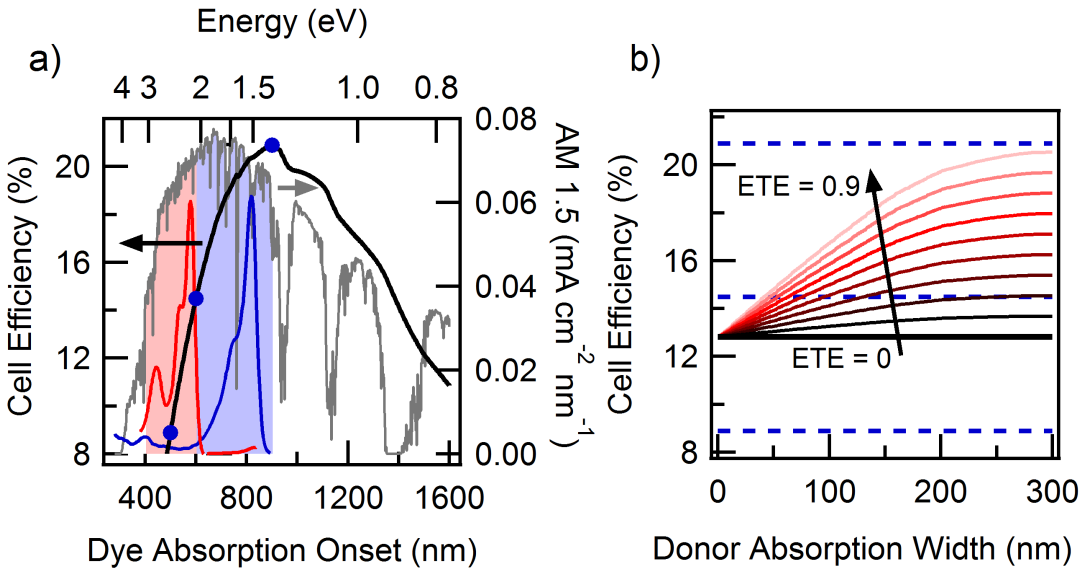

Figure 5.5: (a) The theoretical efficiency for a dye cell with a single sensitizing dye with FF = 0.73, and loss of 0.5 eV (black line). The blue markers show the efficiency at an absorption onset of 500, 600, and 900 nm. The AM 1.5 spectrum is shown for reference (grey line). The filled portions of the AM 1.5 spectrum show the photons absorbed by the donor (light red) and acceptor (light blue) in a relay dye system with donor absorption width of 200 nm. (b) The theoretical efficiency for a dye cell with the same assumptions, but with an acceptor absorbing between 600 and 900 nm, and a donor with absorption onset at 600 nm and varying absorption width for ETE ranging from 0 to 0.9 in increments of 0.1 (red lines). The blue dashed lines show the efficiencies of the cells with a single sensitizing dye at the absorption onsets marked in (a).

in potential of 0.5 eV would correspond to a V_{oc}= 0.88). While using sensitizing dyes that absorb further into the IR could lead to higher efficiencies, this would only be the case with losses in potential of less than 0.5 eV. The key to building a competitive DSC with ERDs will be finding an optimized NIR sensitizing dye with low losses. To model the DSC with a relay dye, we assume the sensitizing dye (acceptor) absorbs photons between 600 and 900 nm with IPCE = 0.9 and

IQE = 0.95. The energy relay dye (donor) has an absorption onset at 600 nm and varying absorption width, over which it is assumed to absorb all photons. Our results are plotted for ETE between 0 and 0.9 (Figure 5.5b). The acceptor alone would have an efficiency of 12.8%. When energy transfer from the relay dyes adds to the photocurrent, the efficiency increases up to a maximum 20.5% (nearly the same as predicted for a single dye with IPCE = 0.9 absorbing over the entire range). The efficiencies of the single-dye cells with absorption onsets at 500, 600, and 900 are shown for comparison and it interesting to note that the single-dye cell with absorption onset at 600 nm outperforms the relay dye DSC for some ETEs and donor absorption widths. However, for cells with high ETE and reasonable absorption, the cell with the relay dye is superior. For donor absorption with a width of 100 nm, there is a 30% improvement to efficiency at ETE = 0.9. If the width is increased to 200 nm, the improvement is 54%, and at a width of 300 nm the efficiency is improved by 60%.

5.5 Conclusion

One of the most pressing issues for excitonic solar cells is wide spectral coverage, for which efficient energy relay dyes are needed. We have used a KMC simulation to demonstrate that selecting a highly soluble relay dye with large

homotransfer in addition to reasonably good donor-to-acceptor transfer could enhance ETE beyond what was previously predicted.[135] Donor homotransfer was seen to improve ETE in all cases, especially when the donor concentration was increased. Quenching of the exciton by the electrolyte decreases the effectiveness of the donor homotransfer, but improvements are still seen over the case with no donor homotransfer. Donor homotransfer is also important for improving ETE when the nanopores increase in size.

Based on our simulations, we suggest that finding ways to increase R_0^{DD} of the relay dye (decreasing the Stokes shift and/or increasing the extinction coefficient) and increasing the solubility and thus the concentration of relay dye in the electrolyte will lead to improved ETE. Given an increased concentration, having a moderate R_0^{DD} (> 3) will compensate for a lower R_0^{DA} (increased concentration is also desirable for increasing absorption). This effect allows for greater flexibility in choosing a donor-acceptor pair to use as a relay and sensitizing dye and should expand the library of relay dyes that can be used in DSCs, making it easier to find a pair of dyes that will lead to a high efficiency solar cell. In fact if a relay dye could be designed to have high solubility and a very large R_0^{DD} in addition to a high extinction coefficient and absorbance across with UV and visible, it could act as a universal ERD and be paired with any sensitizing dye with complementary absorption that has R_0^{DA} greater than ~ 2 nm.

We also used a simple model to predict the theoretical efficiency of a DSC with a sensitizing dye absorbing in the red and NIR between 600 and 900 nm and a energy relay dye absorbing visible and ultra-violet wavelengths for different values of ETE. The model predicts that an ERD with perfectly complementary absorption to a well-performing NIR sensitizing dye could be used to nearly double the baseline efficiency of a DSC containing the sensitizing dye alone. With our simulation results expanding the selection principles for relay dyes to include dye pairs with smaller R_0^{DA}, the energy relay dye approach may be more tractable than the single-dye approach for extending DSC absorption into the near IR and reaching record breaking efficiencies.

Chapter 6

Energy Transfer Directly to Bilayer Interfaces to Improve Exciton Collection in Organic Photovoltaics

6.1 Introduction

Organic photovoltaics (OPVs), which use organic molecules as donors and acceptors in place of inorganic p-n junctions, have increased in efficiency rapidly, reaching over 10%.[2] Achieving higher efficiency goals requires new design strategies; consequently, work on ternary blends and cascade structures has developed in recent years.[161]

Ternary blend organic solar cells use a third material which allows for improved absorption of the solar spectrum and for implementation of strategies to promote

exciton and charge collection. However, to optimally design such complex solar cells we need to better understand which parameters are key for good performance.

Challenges in Exciton Harvesting in OPVs. Achieving efficient OPVs remains challenging, in part because of the interplay between requirements for collection of excitons and charges. Unlike inorganic solar materials, organic semiconductors have low dielectric constants, causing the excitons to be tightly bound in the bulk material (Frenkel rather than Wannier-Mott excitons). The bound excitons must move through the electron donor or acceptor phase and reach an interface where the energy offset between the donor and acceptor gives a driving force for separating into charges. Since organic semiconductors tend to have small exciton diffusion lengths (on the order of ten nanometers), small domain sizes are preferable for efficient exciton collection. On the other hand, large continuous domains are better for charge collection, because charges must migrate from the interfaces to the electrodes. Often bulk heterojunction (BHJ) morphologies, which have nanostructured domains, are employed to achieve both design requirements.

In comparison to BHJs, bilayer organic solar cells have the donor and acceptor vapor deposited in sequential layers. The vapor deposition has several advantages including better control over morphology and purer donor and acceptor domains. Bilayers are optimal for charge collection because they provide direct charge transport pathways from the interface to the electrodes. However, they are suboptimal

for exciton collection because the excitons formed in the bulk of the donor and acceptor layers cannot reach the interface due to relatively small exciton diffusion lengths. One way to address problems with exciton collection is to engineer films with longer exciton diffusion lengths, for example by controlling molecular orientation, using triplet excitons which have a longer lifetime, or engineering molecular spacings.[162–164] Another option is to overcome relatively low exciton diffusion lengths by using energy transfer to move excitons from one material to another.[112,165]

Exciton Collection via Ternary Blends and Cascade Structures. The simplest way to use energy transfer to enhance exciton collection is to have energy transfer directly from the electron donor to the electron acceptor (or vice versa). This energy transfer scheme was investigated experimentally[110,111,166] and analyzed theoretically.[109,167] Scully et al. for example, modeled exciton diffusion and energy transfer using a one dimensional diffusion equation that was modified to account for exciton decay and energy transfer. It was shown that energy transfer could lead to long range collection (over more than 25 nm) of excitons in the donor material. It has even been shown that exciton diffusion lengths are often overestimated due to the confounding influence of energy transfer from the donor to the acceptor.[168,169] However, this energy transfer scheme is limited because it only enhances exciton collection in one of the materials. In order to take

further advantage of energy transfer, additional device architecture engineering is necessary.

Ternary blend solar cells use a third organic semiconductor in addition to the electron donor (hole transporting material) and acceptor (electron transporting material) in order to broaden the absorption across the solar spectrum. The third material must have compatible energy levels with the electron donor and acceptor and is generally selected so that the ionization energies (IEs) and electron affinities (EAs) of the materials form an energy cascade for transport of the charges. The energy cascade helps separate charges and is additionally beneficial to reduce geminate charge recombination by spatially separating charges.[170] Many examples of ternary blends in bulk heterojunction solar cells show modest improvement to power conversion efficiency (PCE),[171–179] although there are also cases where apparently suitable materials with well aligned energy levels do not always improve PCE.[178,180,181] The relative positions of the three materials in the blend morphology is important for the energy cascade to function and is not easily controlled in bulk heterojunctions. It is however, more controlled in evaporated solar cells.[114,182–184]

In addition to using energy cascades to improve charge separation and reduce recombination, they can also be engineered to improve exciton collection. If in addition to having a cascade of IEs and EAs, the materials also have a cascade

of bandgaps, then they can benefit from an energy transfer cascade as well. Just as cascading IEs and EAs facilitate movement of the charges to the electrodes, cascading bandgaps, when properly arranged, can facilitate movement of excitons to interfaces. Roughly speaking, excitons will energy transfer to the material with to lowest bandgap, so a third low-bandgap component can be used not only to enhance absorption across the solar spectrum, but also to control the destination of excitons that are generated in other layers.

There are several ways to arrange an energy transfer cascade, but the main idea is that excitons that are generated in a larger optical gap material can be transferred to another material with a smaller optical gap via Förster energy transfer, and so on. One example is to have an energy cascade interfacial layer where the low-bandgap material is placed between the higher bandgap electron donor and acceptor; thus, excitons energy transfer to the middle layer, facilitating their movement toward the donor and acceptor interfaces. The electron donor (D) and the electron acceptor (A) are now energy donors and the interfacial cascade layer (C) can be an energy acceptor. When excitons can be quickly energy transferred directly to the interface rather than slowly diffusing there, they can generate charges with much higher efficiency, leading to a higher overall PCE. Several experimental papers have achieved improvements to evaporated bilayer solar cells using energy cascade architectures with interfacial layers.[113–117,185–187]

A variation on this basic architecture is to use a multi-donor or multi-acceptor cascade. The layers simultaneously have graded absorption spectra and funnel excitons from the largest to the smallest optical gap donor (or acceptor). Depending on the energy offsets, the exciton could be separated into charges at some or all of the interfaces. Several examples of successful 3-donor energy cascades have been published.[113,115,117] Creating cascaded devices demands versatile, ambipolar materials with a range of band- and optical gaps. Donors with a wide variety of energy levels and bandgaps are available, but the development of tunable, non-fullerene acceptors is needed because the commonly used fullerene-derivative acceptors are somewhat limited.

Understanding and Modeling Excitons in Multi-component OPVs. In order to characterize the effectiveness of the energy transfer in ternary blends one needs a figure of merit, which is commonly chosen as the exciton collection efficiency (ECE). The ECE is part of the external quantum efficiency (EQE) of a solar cell, which describes its overall efficiency at different wavelengths. The EQE is a product of the efficiencies of absorption, exciton collection, and charge collection. Therefore the solar cell must both absorb light efficiently and have a high exciton collection efficiency in order to have a high overall efficiency. This introduces a competing requirement for film thickness. The film needs to be thick in order to absorb light, but it needs to be thin enough that excitons can be

collected efficiently. The thicker the bilayer, the more light it will absorb thereby increasing the efficiency of exciton generation. In order to absorb 80% of the light at the absorption maximum, assuming a very high molar extinction coefficient of 350000 cm^{-1}, the film would need to be $\sim$ 46 nm thick and to absorb 90% of the light, it would need to be $\sim$ 66 nm thick (using the Beer-Lambert law and neglecting thin film optical effects that add oscillations in the fraction of light adsorbed as a function of film thickness due to interference[188]). For smaller extinction coefficients, the films would need to be even thicker. Such films with high absorption are thick enough that exciton collection would occur with a very low efficiency in a standard bilayer solar cell given typical exciton diffusion lengths of $\sim$10 nm. Even very high exciton diffusion lengths (100 nm) would be too small to achieve good performance with the thickest layers. Typical layers are generally between 5 and 100 nm thick in order to balance efficiencies of light absorption and exciton collection.

Simple bilayer structures can be modeled using diffusion-reaction equations that include terms for exciton generation, decay, and energy transfer.[109] However, more complex systems with rough interfaces or mixed interfaces become difficult to model with differential equations. Therefore we use kinetic Monte-Carlo (KMC) simulations to examine the effect of energy transfer in ternary energy cascade architectures relevant to organic solar cells. In this work, we use KMC simulations

to examine energy transfer strategies for improving exciton collection. Improving exciton collection allows for increased thickness of donor and acceptor layers and thus an increase in PCE due to increased optical absorption and high exciton yield. We identify several cascade architectures that take advantage of Förster energy transfer that can increase exciton yield to nearly 100%, even for optically thick films.

6.2 Simulation Methods

KMC simulations were carried out treating chromophores as points on a cubic lattice with a lattice constant of 1 nm giving a chromophore density of 1 chromophore/nm^3,[189] which is a typical value for small molecule chromophores in an organic film. For example PCBM, a common acceptor molecule, has a density of 1.5 g/cm^3 which corresponds to a chromophore density of 0.99 molecules/nm^3. Non-fullerene small molecules tend be more dense and conjugated polymer chromophores tend to be less dense. Energy transfer, $x^* + y \rightarrow x + y^*$, was simulated for single excitons using the rate

$$k_{ij} = \frac{1}{\tau}\left(\frac{R_0^{xy}}{r_{ij}}\right)^6 \tag{6.1}$$

where τ is the exciton lifetime, R_0^{xy} is the Förster transfer radius from a chromophore of type x to one of type y, and r_{ij} is the distance between chromophores i and j. Periodic boundary conditions were used in the plane of the film. Dexter transfer was not treated in our simulations.

The Förster transfer rates are treated as orientationally averaged and the transition dipole orientation is not treated in this work. Therefore the orientation factor, κ^2 is assumed to be 2/3 which is the value of κ^2 for dynamically averaged dipoles. More correctly, one should use $\kappa^2 = (0.8452)^2(2/3)$ for statically averaged dipoles;[126] however in this work we use $\kappa^2 = 2/3$ for consistency because it is the value most often used when calculating R_0 and only introduces a ~5% error in the Förster transfer rate which involves a $\kappa^{1/3}$ term. Assuming preferentially oriented dipoles (which would result from molecular orientation in non-amorphous films) would introduce anisotropic exciton diffusion rates and is not considered here. The effect of dipole alignment on energy transfer to the interface is briefly discussed in the section on charge transfer states as energy acceptors.

The self-transfer Förster radii, R_0^{DD}, R_0^{AA}, and R_0^{CC}, were set at 1.5 nm[1] so that the exciton diffusion length for each material is 5.6 nm,[2] a typical value for an exciton diffusion length in an organic semiconductor film (L_D from 5 to 10

[1]All exciton lifetimes were assumed to be equal to reduce the number of simulation parameters.

[2]The exciton diffusion coefficient for energy transfer in a cubic lattice is given by $0.409C^{4/3}R_0\tau^{-1}$ where the concentration, C is given by $4/3\pi R_0^3\rho$.[97] The exciton exciton diffusion length calculated from our simulations matches well with L_D calculated from this definition.

nm).[190] It has in fact been suggested that many reported exciton diffusion lengths are overestimated because they are enhanced by energy transfer.[191] In order to be consistent with the organic semiconductor literature, we use the definition of exciton diffusion length $L_D = \sqrt{D\tau}$, so the constant factors of $\sqrt{2}$ and $\sqrt{6}$ are included in the one and three dimensional solutions as necessary, respectively. The Förster transfer radii between dissimilar materials were varied between 1.5 and 10 nm, depending on the energy-cascade device architectures being simulated. In the simulations, excitons are generated in the film with a uniform distribution[3]. The exciton is considered to be collected when it reaches an interface. Charge collection is not simulated, instead we focus only on the contribution from exciton migration.

6.3 Results and Discussion

We examine how energy transfer can be used for an electron donor (D), acceptor (A) and energy cascade material (C) to improve exciton collection in device structures relevant to bilayer organic solar cells. The C chromophore is always assumed to have the narrowest gap with the longest wavelength absorption and

[3]A uniform distribution is used rather than a more complex absorption profile because the absorption profile depends on the position of the layer in the device and whether optical spacer layers are used. Exciton collection efficiency will be lower than predicted if the absorption profile is higher in regions far from the interface and higher if the absorption profile is higher in regions near the interface.

therefore always acts as an energy acceptor. In this work we examine two energy cascade schemes: Scheme A: $D \rightarrow C$ and $A \rightarrow C$ and Scheme B: $D \rightarrow A \rightarrow C$[4] (Figure 6.1a). Using these schemes, we simulate a variety of bilayer/interface architectures (Figure 6.1b) including: case 1: a bilayer with a monolayer of C at the flat (or rough) interface and energy transfer Scheme A, case 2: a bilayer with a multilayer of C at the flat interface and energy transfer Scheme A and case 3: a bilayer with a monolayer of C at the flat interface and energy transfer scheme B. We determine how a larger exciton diffusion length affects the role of energy transfer in exciton collection and discuss insights the simulations give us into the experimental literature. Additionally, we discuss the possibility that a charge transfer state could behave as an energy acceptor for a built-in cascade interfacial layer.

6.3.1 Energy Transfer in a Bilayer Morphology

Bilayer morphologies are often used in evaporated and solution processed[192,193] solar cells. While the bilayer structure is favorable for charge collection, it is not ideal for exciton diffusion to an interface when layers are thick. Here we explore

[4]Equivalent to $A \rightarrow D \rightarrow C$. The electron donor(acceptor) can act as either an energy donor or acceptor. The material's status as an electron donor or acceptor depends on its relative IE and EA. The material's status as an energy donor or acceptor depends on its bandgap and absorption and emission wavelengths.

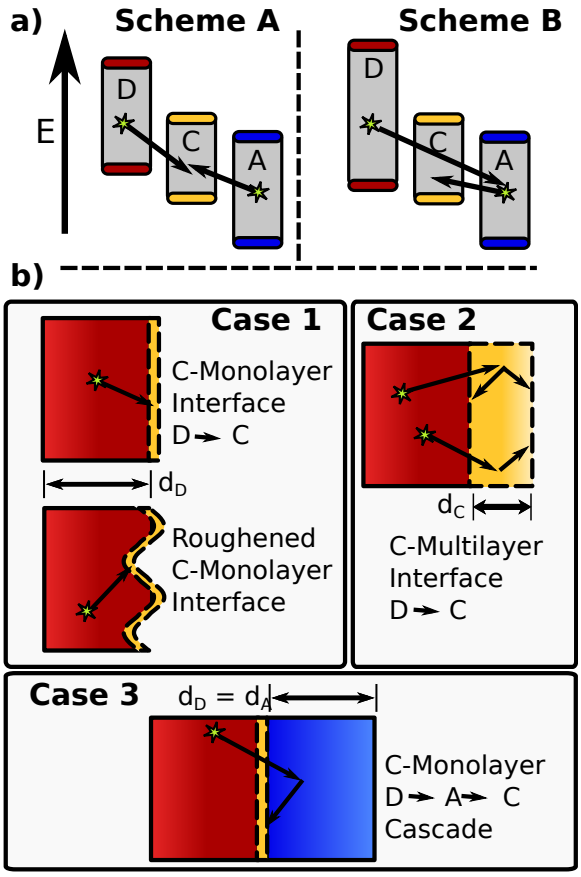

Figure 6.1: (a) Energy levels for energy transfer cascades for scheme A: direct transfer from D and A to the cascade interface C and scheme B: transfer from $D \rightarrow A \rightarrow C$. (b) Different DAC ternary blend energy cascade device architectures simulated in this work.

how energy transfer strategies can be used to improve exciton collection in bilayer structures.

6.3.2 Analytical Approximations

Using analytical expressions for exciton diffusion and energy transfer, we are able to offer some analytical approximations for ECE as a function of layer thickness for case 1 (see Appendix B for derivations). Exciton collection can occur via two mechanisms: exciton diffusion which we approximate based on a solution to the diffusion equation and energy transfer of the exciton to energy acceptors (C) at the interface, which we approximate using the known rate for energy transfer to a plane.[109]

The analytical approximations yield three interesting results: (1) For the experimentally reasonable values of R_0 and L_D, exciton diffusion outperforms energy transfer at low film thicknesses ($d_D \lesssim 5$ nm); however, the ECE for exciton diffusion drops off more rapidly with increasing film thickness than for energy transfer so for certain values of R_0 and L_D, there is a crossover where energy transfer leads to higher ECE for thicker films (Figure 6.2a). (2) Based on these two analytical solutions, we can define a lower bound on the ECE when exciton diffusion and energy transfer are both included (Figure 6.2b). The KMC simulated ECE is better than the lower bound because the exciton diffusion reinforces the energy

transfer by moving excitons within easy energy transfer range of the interface and the energy transfer provides a driving force for the capture of excitons generated near the interface before they can diffuse away. (3) For all thicknesses, the energy transfer to an infinite slab is significantly more effective than energy transfer to a plane (monolayer) for comparable R_0 (Figure 6.2c). The higher rate for transfer to a slab motivates the use of the C-multilayer in case 2 and the $D \rightarrow A \rightarrow C$ energy transfer in case 3.

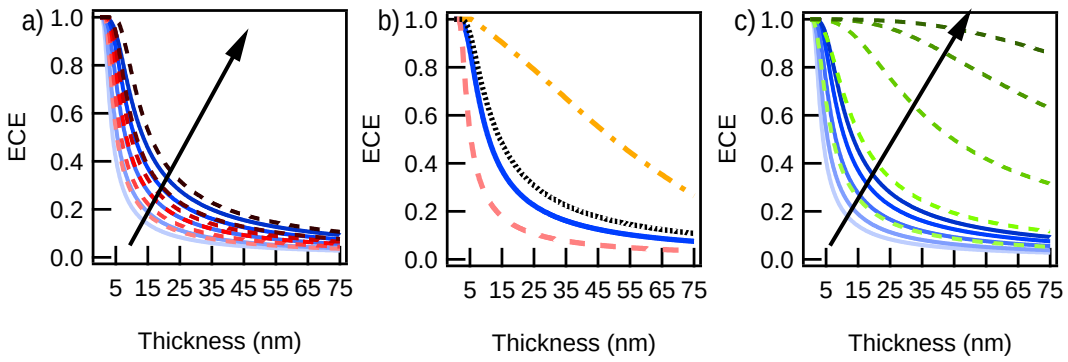

Figure 6.2: Predictions of our analytical approximations for exciton collection efficiency for (a) exciton diffusion alone (red, dashed) and energy transfer alone (blue, solid) with the arrow showing increasing L_D (5.6, 8.8, 13.6, 18.8, 21.4, 25.8, and 50 nm) for exciton diffusion and increasing R_0 (2, 3, 5, 7.5, 10 nm) for energy transfer. (b) The lower bound (black, dotted) and simulated (yellow, dash-dotted) ECE for a bilayer film with both exciton capture mechanisms active with $R_0 = 7.5$ nm (blue, solid, energy transfer only) and $L_D = 5.6$ nm (red, dashed, exciton diffusion only). (c) ECE for energy transfer from a point to a plane (blue, solid) and to an infinite slab (green, dashed) for the same R_0, with the arrow showing increasing R_0 (2, 3, 5, 7.5, 10 nm)

6.3.3 Case 1: Energy Transfer to a C-Monolayer

We first simulate the simplest energy cascade scheme, which involves D and A acting as energy donors to C, an energy acceptor (Figure 6.1a, Scheme A). Excitons from D do not transfer to A (or vice versa) because the spectral overlap between D and A is assumed to be negligible. The following energy transfer processes are allowed:

1. $D^* + D \rightarrow D + D^*$ with R_0^{DD}
2. $D^* + C \rightarrow D + C^*$ with R_0^{DC}
3. $A^* + A \rightarrow A + A^*$ with R_0^{AA}
4. $A^* + C \rightarrow A + C^*$ with R_0^{AC}

We simulate this scenario with a monolayer of C between bilayers of D and A with varying bilayer thickness ($d_D = d_A$ from 7 to 75 nm) and Förster transfer radii ($R_0^{DC(AC)}$ from 1.5 to 10 nm) and determine the exciton collection efficiency. It is assumed that charges can be generated at either the A/C or D/C interface.

Overall as the film thickness increases ECE decreases (Figure 6.3a). However increasing $R_0^{DC(AC)}$ for energy transfer to the cascade interfacial layer significantly increases the ECE. For the thinnest bilayer (7 nm), the ECE is increased by nearly 70% when $R_0^{DC(AC)} = 5$ nm and for the thickest bilayer (75 nm), the increase in

ECE is over 160%. For intermediate film thicknesses, including energy transfer ($R_0^{DC(AC)} = 10$ nm) greatly increases ECE from 0.2 to 0.93 and from 0.08 to 0.6 for the 25 nm and 50 nm films, respectively. Unfortunately for the thicker layers, which may be needed to absorb all of the incident sunlight, unrealistically large values of $R_0^{DC(AC)}$ would be necessary to reach higher ECE. For the 75 nm film, the overall ECE still remains low, only reaching 0.4 at $R_0^{DC(AC)} = 10$ nm. Having a monolayer of C at the interface leads to large increases in ECE, but additional strategies are needed to reach very high ECE for the thickest films (> 50 nm), which are needed to achieve high EQE.

For thicker films without an energy cascade or those with low $R_0^{DC(AC)}$, the tradeoff between increasing absorption and lower ECE is not enough to improve the overall number of excitons collected. However, in films where the ECE gets a boost from the energy transfer cascade, increasing film thickness does lead to an overall increase in the relative number of excitons collected (Figure 6.3b) (assuming a uniform distribution of the excitons in the film, with exciton generation proportional to total absorption calculated by the Beer-Lambert law for an extinction coefficient of 350000 cm^{-1})[5]. For $R_0^{DC(AC)} = 7.5$ nm, a 25 nm film will lead to two times more excitons being collected than for a 7 nm film, (2.5 times more at $R_0^{DC(AC)} = 10$ nm). The 50 nm film has overall worse ECE than the 25

[5]As before, thin film effects are neglected.

nm film, but approaches the same value at high $R_0^{DC(AC)}$. Assuming high charge mobilities so the increased thickness does not affect charge collection, the energy transfer cascade would allow for thicker solar cells with improved PCE.

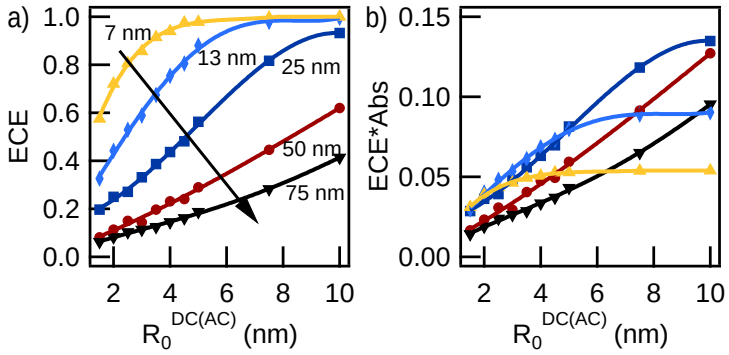

Figure 6.3: (a) The exciton collection efficiency (ECE) for films (D or A) of increasing thickness from 7 to 75 nm with a monolayer energy cascade material (C) at the interface. The arrow indicates increasing film thickness. (b) The product of ECE and fraction of light absorbed for each film thickness.

Even for the films with the best exciton harvesting, the upper bound on the EQE for bilayers with perfectly flat interfaces (assuming good charge separation and collection) appears to be around 15% (Figure 6.3b). One way to address the low ECE for thick layers is to increase interfacial area by roughening the bilayer interface. We simulate this condition using an egg-crate $Asin(2\pi x/L)sin(2\pi y/L)$ interface (Figure 6.1c). We vary the period and amplitude of the *sin* functions to generate a representative set of rough interfaces for 50 and 75 nm thick films. The period was varied so that the features were 15, 30, 60, or 120 nm in the plane of the film. The amplitude was varied from 5 nm up to the film thickness (50 or

75 nm). ECE is seen to increase with increasing amplitude and decreasing period (Figure 6.4a). Amplitudes approaching the thickness of the film were required to reach high ECE. In the 50 (75) nm film, increasing the film roughness without introducing the energy transfer cascade layer increased ECE from 0.13 to 0.38 (0.06 to 0.31). Adding the energy cascade significantly increased ECE, even for small $R_0^{DC(AC)}$. However a $R_0^{DC(AC)}$ of at least 3.5 nm (4 nm) was needed to reach an ECE of 0.9 for the 50 nm (75 nm) film. Even for features with high amplitude (A = film thickness), increasing L decreases the ECE (Figure 6.4b). For a 50 nm (75 nm) thick film, an ECE of 0.9 can be reached for L up to 60 nm, with $R_0^{DC(AC)}$ = 8 nm ($R_0^{DC(AC)}$ = 8.5). Smaller $R_0^{DC(AC)}$ are sufficient for smaller L. Overall, the films with small L, large A, and large $R_0^{DC(AC)}$ had the best ECE. This morphology is similar to a columnar/chessboard-type structure with tall, narrow columns often suggested as an optimal design for OPVs.[138,194,195]

Having a bilayer with a roughened interface is clearly beneficial for the performance of OPVs and this result corresponds well with experimental results.[26,196] However, for very thick films it is nearly impossible to achieve > 90% ECE with a roughened interface alone (no energy transfer). Including an energy transfer cascade will however, lead to the improved, > 90% ECE necessary for good solar cell performance, even with moderate Förster transfer radii.

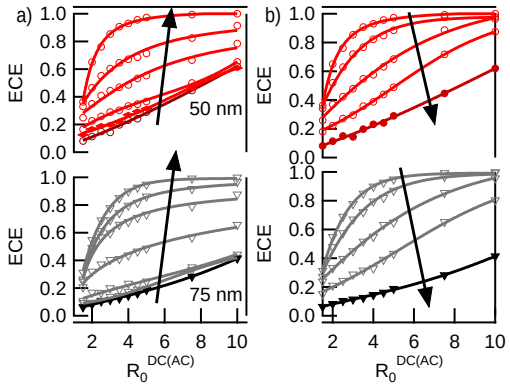

Figure 6.4: The exciton collection efficiency (ECE) for 50 (red) and 75 (black) nm thick films for an interface with increased roughness, but still only a monolayer of the interfacial energy cascade layer. (a) L = 15 nm and A varied from 0 to the film thickness. The arrow shows the direction of increasing A (0, 5, 10, 20, 30, and 50 nm in red and 0, 5, 10, 30, 50, 60, and 75 nm in black). (b) A = film thickness, L varied from 15 to 120 nm. The arrow shows the direction of increasing L (15, 30, 60, and 120 nm).

To summarize case 1: For relatively thin films $\leq$ 25 nm, a monolayer of cascade interfacial layer should be sufficient to boost the ECE to greater than 0.9. Roughening the interface with the monolayer of C can provide an additional boost, allowing for a high ECE, even for thick films up to 75 nm as long as the amplitude of the roughness is on the order of the film thickness and the period of in-plane modulation is short, i.e. 30 nm or less.

6.3.4 Case 2: Energy Transfer to a C-Multilayer

Increasing the interface roughness (i.e. a nanostructured morphology) is one way to improve exciton collection efficiency. Another option is to increase the

energy cascade interfacial layer from a monolayer to a multilayer (Figure 6.1b, case 2). The analytical rate of energy transfer from a point to a plane is given by (see Appendix B)

$$k_f^{\text{point-to-plane}} = \tau^{-1} \frac{\pi R_0^6 C_A}{2} \frac{1}{x^4} \tag{6.2}$$

where x is the distance of the D or A exciton to the C-plane and C_A is the two-dimensional energy acceptor concentration, whereas the rate for transfer from a point to a slab of thickness L is given by

$$k_f^{\text{point-to-slab}} = \tau^{-1} \frac{\pi R_0^6 C'_A}{6} \left(\frac{1}{x^3} - \frac{1}{(x+L)^3} \right) \tag{6.3}$$

where in this case x denotes the distance of the exciton to the nearest face of the C slab and C'_A is the three-dimensional concentration. Since the rate goes from being proportional to x^{-4} to proportional to $\sim x^{-3}$ (at large L), we would expect more efficient energy transfer for a thicker interfacial layer. We simulated multilayers to explore how increasing the thickness of the interfacial C-layer affects the energy transfer of excitons to the interface (Figure 6.5). We find that as the interfacial layer thickness increases, the fraction of excitons reaching C increases rapidly. For a 50 nm thick donor layer with only a monolayer of C (R_0^{DC} = 7.5 nm), 45% of the excitons will be captured. Increasing the monolayer to a C bilayer leads to 50% of excitons being captured and having a 10 molecule thick C layer increases

the proportion of excitons reaching C to nearly 60%. The effect is strongest for larger R_0^{DC}.

Optimizing C-layer Thickness. However, having a broad interfacial layer may lead to a reduction in charge separation because the exciton is no longer immediately at a D-C or A-C interface. If the exciton must migrate to one side or the other of the C-layer then not all of the excitons reaching C will actually form charges before decaying. For the 50 nm bilayer with $R_0^{DC} = 7.5$ nm, 99% of excitons reaching the interfacial C bilayer are collected. For a 5 molecule thick layer of C the number of excitons reaching C that are collected drops to 97% and for a 10 molecule thick layer it drops to 86%. Even though more excitons are reaching the C-block for thicker C layers fewer of them will actually be collected at the interface. This interplay between efficient energy transfer to C and inefficient migration to the C-interface leads to a sweet-spot in C-layer thickness. The optimal thickness of C depends on d_D and R_0^{DC}. The ECE for films with C-multilayers ($d_D = 25$ and 50 nm) is shown in figure Figure 6.5a. In the simulations for 25 and 50 nm thick films, the C-layer thickness had almost no effect until R_0^{DC} was greater than about 3 nm. Above $R_0^{DC} = 3$ nm, the optimal C-layer thickness ranged between 2 and 6 layers, but only made a difference of about ± 0.1 in the overall ECE (Figure 6.5c).

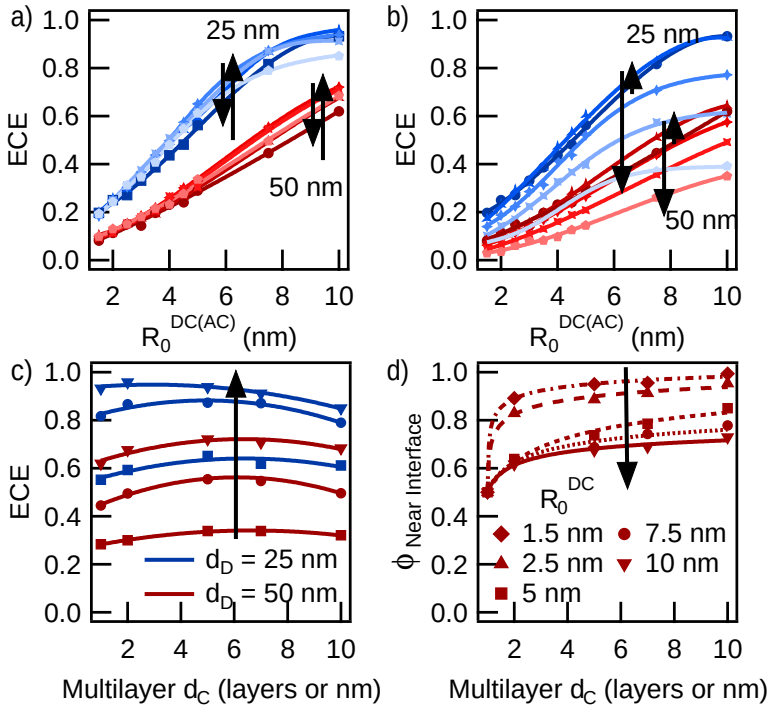

Figure 6.5: (a) and (b) The exciton collection efficiency for multilayers of C ranging from 1 to 10 layers (nm) for bilayers with film thickness 25 and 50 nm. In (a) excitons can be collected on both sides of C and in (b), they can only be collected at the far side. The markers are from simulations of 1, 2, 5, 7, and 10 layers and the lines are best fits (dark to light). (c) The exciton collection efficiency versus number of C-layers for large values of R_0^{DC} for 25 and 50 nm thick bilayer films. (d) The fraction of excitons collected at the near interface for different thicknesses of C-layers and values of R_0^{DC} for the 50 nm thick film.

Consequences of a Thick C-layer. When excitons are transferred to the C block, they must reach either the near or far side of the C block to be collected. In Figure 6.5d, we quantify the fraction of excitons collected at the near side of the C layer for $d_D = 50$ nm. The probability of being collected on either side of the C-block is equal for a monolayer of C, but as the C layer increases in thickness, the likelihood of excitons being collected on the near side of the interface increases.

Additionally, the exciton is more likely to be collected on the near side of the interface for systems with small values of R_0^{DC}. This is because for large values of R_0^{DC} excitons are able to transfer farther into the C-block than for small values. We can see this from a plot of the distribution of positions of excitons after first arrival in the C region (Figure 6.6). The simulation results show that the excitons are positioned according to a distribution that is best fit by a double exponential function with the majority of excitons located within a few nanometers of the interface. As R_0 increases, excitons are transferred farther into the energy acceptor, allowing some of them to migrate to the far interface.

In some energy cascade schemes, there may not be enough driving force to separate excitons at both sides of the C-layer. In this case the excitons may need to diffuse across the C-layer before they can be collected. We simulated this situation (Figure 6.5b) and find that indeed, ECE is significantly reduced for thick C-layers when excitons cannot be collected at the near interface. In fact

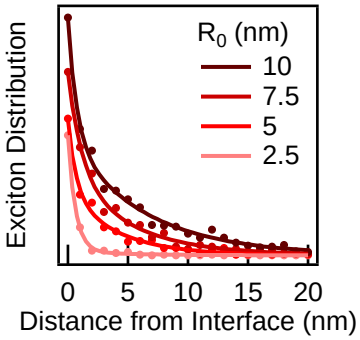

Figure 6.6: The distributions of the positions in the energy acceptor material ($d_A = 75$ nm) that excitons reach immediately after transfer from an energy donor ($d_D = 75$ nm) with a flat interface.

having a C layer with more than 2 monolayers is detrimental to exciton collection when the excitons must reach the far interface. The exciton collection at the far interface is even less than one would expect for uniformly distributed excitons because the excitons are actually preferentially distributed at the near interface (as in Figure 6.6).

To summarize case 2: Despite the increase in the energy transfer rate, using a C-multilayer offers only moderate overall enhancement to ECE; thus energy acceptor multilayers are not an effective way to enhance ECE. Additionally, when optimizing the interfacial layer thickness, one to five layers of material should be sufficient, and it is likely better to err on the side of thinner layers. However, a thick C-layer may be desirable to allow for the absorption of more light in a complementary region of the solar spectrum. In order to overcome the limitation of using a thick C-layer, the C material would need to have a larger exciton

diffusion length (increased from 5.6 up to at least 20 nm) so that excitons could more readily reach the interface or the interface would need to be roughened to increase interfacial area as discussed in the previous section.

6.3.5 Case 3: Energy Transfer to the acceptor and the monolayer

Finding a donor and acceptor that both transfer efficiently to the interfacial cascade material and also maintain other requirements necessary to function well in an organic solar cell (e.g. complementary absorption and IE/EA cascades) may be challenging. An energy transfer scheme that would be easier to attain experimentally may be $D \rightarrow A \rightarrow C$ (Figure 6.1b) which would include the following processes:

1. $D^* + D \rightarrow D + D^*$ with R_0^{DD}
2. $D^* + A \rightarrow D + A^*$ with R_0^{DA}
3. $A^* + A \rightarrow A + A^*$ with R_0^{AA}
4. $A^* + C \rightarrow A + C^*$ with R_0^{AC}.

Excitons from D do not transfer to C because the optical gap of C is too low in energy for the emission from D to overlap the absorption of C.

Therefore, in this case D is an energy donor to A, and A is an energy donor to C. We would expect that the exciton collection efficiency for the A layer would be the same as predicted for the flat monolayer in case 1 but the efficiencies for D should change. We simulate this energy cascade for $L_D = 5.6$ nm and $R_0^{DA} = R_0^{AC}$ from 1.5 to 10 nm (Figure 6.7a). At low $R_0^{DA(AC)}$, the ECE is essentially identical to direct transfer to C, but as $R_0^{DA(AC)}$ increases, the ECE actually surpasses the ECE for direct transfer to a monolayer of C. Because the A region is thicker than one monolayer and therefore there are more chromophores to which the exciton can transfer, the overall rate of exciton transfer from D to A is larger than for D to a monolayer of C, especially for large R_0^{DA} (much like in case 2). Once excitons hop to A, they are still near the interface (Figure 6.6) and R_0^{AC} is large so they transfer to the C interface with high probability before decaying (unlike in case 2).

Due to better exciton yield with the $D \rightarrow A \rightarrow C$ scheme, a 50 nm film, which would have had ECE = 0.6 with a C monolayer ($R_0^{DC} = 10$ nm), would now have ECE = 0.8 ($R_0^{DA} = R_0^{AC} = 10$ nm). Thus at large values of R_0, the $D \rightarrow A \rightarrow C$ scheme show a 33% improvement over the monolayer case or a 900% improvement over the case without an energy transfer cascade (ECE = 0.08).

Effectiveness of the Interfacial C Layer. In order to elucidate the relative importance of the $D \rightarrow A$ and $A \rightarrow C$ transfer, we simulated a similar case

where the enhanced energy transfer only occurred from D to A and not A to C (R_0^{AC} = 1.5 nm). Figure 6.7b shows that even by itself, the $D \rightarrow A$ transfer improves ECE relative to exciton diffusion alone. However, even though most of the excitons in A will be localized near the interface in a double exponential distribution (as demonstrated in the previous section, Figure 6.6), an efficient $A \rightarrow C$ energy transfer process is also necessary to get the very large values of ECE needed for efficient solar cells.

Enhanced Collection in Thicker Films. Figure 6.7c and d show the probability that an exciton will be collected at various starting positions in a 75 nm thick film with energy transfer for case 1 and case 3. In both cases, excitons near the interface are harvested with high efficiency, but the energy transfer scheme in case 3 is able to harvest excitons farther from the interface. As expected, the probability of exciton collection at a given position is higher with energy transfer included than for exciton diffusion only. This understanding of ECE as a function of position could be used along with optical modeling of a solar cell stack to optimize layer thicknesses. Because the energy transfer cascade schemes extend the region in which excitons can be efficiently harvested, energy transfer should make the solar cells more robust to thin film optical effects that localize the electric field maximum within the film causing sensitivity to layer thickness.

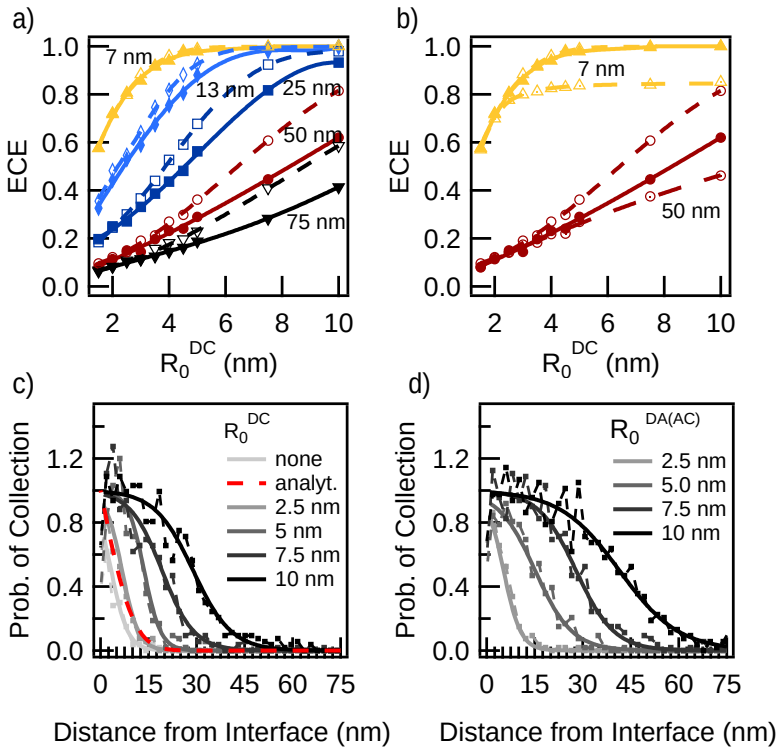

Figure 6.7: (a) The exciton collection efficiency (ECE) for the $D \rightarrow A \rightarrow C$ cascade (dashed lines, open markers) compared with ECE for the corresponding results for $D \rightarrow C$ or $A \rightarrow C$ (solid lines, filled markers). (b) The ECE for $d_D =$ 7 and 50 nm and $d_A = 50$ nm with a $D \rightarrow A \rightarrow C$ cascade a slow rate of $A \rightarrow C$ transfer (R_0^{AC} =1.5 nm) (red, long-dashed) compared with the results in (a). The probability an exciton reaches the interface and is collected, given its starting position in the film for (c) case 1 and (d) case 3.

To summarize case 3: Surprisingly, the $D \rightarrow A \rightarrow C$ cascade (Scheme B) with a monolayer of C at the interface leads to better ECE than Scheme A with with a monolayer of C at the interface for comparable Förster transfer radii. This energy cascade scheme is also in general more experimentally viable for three materials with complementary absorption and is also relevant to charge transfer (CT) states, which are located at electron donor-acceptor interfaces and have the potential to behave as energy acceptor monolayers.

6.3.6 Exciton Diffusion Length

In the previous sections, we simulated moderate exciton diffusion lengths (L_D = 5.6 nm). In order to confirm that energy transfer is still effective for materials with higher L_D, we simulated ECE for a representative selection of conditions described previously for L_D up to 26 nm (see Figure S1). We conclude that even for systems with higher L_D, introducing the energy transfer cascades and roughened interfaces still leads to significantly improved ECE. Thus these remain viable strategies for improving exciton yield, even when exciton diffusion lengths are large.

6.3.7 Applications to Experimental Literature

Recently an 8.4% efficient organic solar cell using an energy transfer cascade without fullerene was published by Cnops et al.[116] They used a donor, $\alpha-6T$, and two acceptors, SubPc and SubNc, in a trilayer structure: $\alpha-6T$(60 nm)/SubNc(12 nm)/SubPc(18 nm). The SubPc and SubNc have the same EA levels and the IEs are only offset by 0.2 eV so the authors assume that there is not enough driving force to separate excitons at the SubPc/SubNc interface This is analogous to our case 2 with a thick C-layer (12 nm SubNc) between the energy donor (electron acceptor) and energy acceptor (electron donor) where the excitons reaching C from energy transfer can only be collected at the far side of the C-layer. This means that excitons generated in SubPc must reach the SubNc/$\alpha-6T$ interface before they can generate charges. However, the IQE shows that both SubPc and SubNc have high efficiency of exciton collection. They propose a mechanism that the SubPc material energy-transfers to the SubNc with a measured Förster transfer radius of $R_0 = 7.5$ nm; then all excitons are separated at the SubNc/$\alpha-6T$ interface.

Using our simulations, we test this proposed mechanism given their experimental data (thickness, R_0, etc).[116] We find that for a flat interface the exciton should transfer from SubPc to SubNc with 99% efficiency. However, assuming an exciton diffusion length of 5.6 nm for the SubNc (corresponding to $R_0 = 1.5$

nm), the efficiency of excitons reaching the SubNc/$\alpha-6T$ interface is only 27%. In order for the ECE to be high enough to account for the high IQE, the exciton diffusion length in SubNc must be greater than 18.4 nm (corresponding to a high self-$R_0 = 4.5$ nm). Alternatively the roughness of the interface may explain how the excitons are collected with such high efficiency. The RMS roughness of the SubNc/$\alpha-6T$ films is 15.9 nm by AFM,[6] greater than the thickness of the SubNc film. Despite the high roughness which would lead some SubPc contacting $\alpha-6T$, the authors assume that the SubPc/$\alpha-6T$ interfacial area is too small for many excitons to be collected directly from SubPc, which is likely true. Our simulations suggest that the roughness instead enhances collection of excitons via the SubPc $\rightarrow$ SubNc energy transfer pathway indirectly by reducing the distance excitons must diffuse once they have been energy transferred to SubNc. In a case like this where the interfacial layer is also used for light harvesting in the 700 to 900 nm region of the solar spectrum, a greater than monolayer thick SubNc layer is necessary and therefore roughness at the interface is crucial for achieving high ECE and thus good solar cell performance.

[6]In addition to AFM, interfacial roughness in this type of solar cell could be measured by X-ray and neutron refelctometry.[197]

6.3.8 CT States as Energy Acceptors

In cases 1 and 3, we showed that a monolayer of an energy cascade interfacial layer greatly improved exciton yield. Charge transfer (CT) states form between adjacent donor and acceptor chromophores, thus forming an effective interfacial monolayer (assuming fairly sharp interfaces between relatively pure domains). Here we propose that donor-acceptor CT states could act as an energy cascade interfacial monolayers (C) for Förster energy transfer and we consider their applicability as energy acceptors for common donor materials. We estimate the value of R_0^{D-CT} for several donor-acceptor systems and discuss how big R_0^{D-CT} could be. We show that energy transfer to CT states could indeed be large enough to have an effect on ECE. We then investigate the effect of dipole alignment at the interface and discuss strategies for maximizing the value of R_0^{D-CT}.

An optimal energy transfer cascade material would spontaneously form a localized layer at domain interfaces and have cascading energy levels that align well with the electron donor and acceptor IEs and EAs as not to limit V_{OC} but to allow for both energy and charge transport. The CT state can meet all of these criteria. By definition, the CT state occurs at the donor-acceptor interface, the energy levels are set by the donor IE and acceptor EA so they are correctly aligned, and the CT energy is related to the V_{OC}.[198,199] Additionally, it has been shown that charges can be generated from direct excitation of the CT state.[200,201]

However, intermolecular CT states have low oscillator strength (at least an order of magnitude lower than reasonably good organic chromophores, e.g. 0.3 vs. 0.024 for BP and BP-PCBNB CT states)The lower oscillator strength will cause a lower extinction coefficient, $\epsilon_a(\nu)$, for the CT state, which will affect the magnitude of R_0. The Förster transfer radius (in nm) can be calculated from

$$R_0^{DA} = \left(8.79 \times 10^{17} \kappa^2 n^{-4} \Phi_D \left[\int \left(\frac{f_D(\nu)\epsilon_A(\nu)}{\nu^4}\right) d\nu\right]\right)^{1/6} \tag{6.4}$$

where κ is the orientational factor, n is the index of refraction, Φ_D is the donor fluorescence quantum yield, $f_D(\nu)$ is the normalized fluorescence of the energy donor, $\epsilon_A(\nu)$ is the absorbance of the energy acceptor scaled by the extinction coefficient, and ν is the wavenumber in cm.[148]

The magnitude of R_0^{DA} depends on the overlap of the donor fluorescence and acceptor absorbance; however there is only a one sixth dependence on $\epsilon_A(\nu)$ so if the CT oscillator strength is 10^{-1} lower than for a representative organic semiconductor absorption, then there would only be a $\sim 20\%$ decrease in R_0 due to the lower extinction coefficient. Additionally, the CT state peak could be well-located for good fluorescence overlap for the lower bandgap material in the solar cell, due to CT state optical gap necessarily being smaller than the optical gaps of the electron donor and acceptor. The lower energy of the CT state is also advantageous

because the ν^4 term in the integrand gives a boost to R_0. Based on these factors, we estimate R_0 could be up to 3.5 nm for a Donor/CT pair with a high quantum yield donor, a CT state with relatively high oscillator strength ($f \sim 0.03$), and good overlap between the emission of the donor and the absorption of the CT state.

Calculating R_0^{D-CT} For Model Materials. Here we calculate R_0^{D-CT} for several representative materials and explain how we estimate an upper bound of ~ 3.5 nm. The CT state for P3HT-PCBM is centered at 1.4 eV[199,202] and we assume an absorption coefficient of 2500 L mol^{-1} cm^{-1}[7]. Based on the absorbance and PL data,[199,202,203] we calculate that $R_0^{P3HT-CT}$ will be 1.1 nm, a fairly small value of R_0, which typically ranges from 1 to 10 nm for donor-acceptor pairs. (See Appendix B for the calculation.) Therefore $R_0^{P3HT-CT}$ is too small to enhance the ECE via Förster transfer relative to exciton diffusion. However, there are two reasons that this value is particularly low; first the P3HT PL emission (peak at 1.75 eV) does not overlap well with the CT state absorption (peak at 1.4 eV), and second P3HT is not an optimal donor because it has a rather low quantum yield (only about 2%[204]).

[7]The actual absorption coefficient has not been measured for this CT state so we use the absorption coefficient for a similar donor-acceptor CT state from BP/PCBNBto obtain an order of magnitude estimate

A CT state better positioned relative to the fluorescence peak and a donor with better quantum yield would lead to a higher R_0^{D-CT}. For the polymer donor APFO3, which has a higher PLQY of $\sim 30\%$, and the acceptor PCBM, the CT sate is centered at 1.9 eV and the fluorescence peak is nearby at 1.8 eV. This leads to a calculated value of $R_0^{APFO3-CT} = 1.9$ nm, which is large enough to generate small improvements to ECE in some cases. For thin, 13 nm films with flat interfaces, it should lead to a 23% (25%) improvement for $D \rightarrow C$ ($D \rightarrow A \rightarrow C$) cascade relative to diffusion only, leading to ECE = 0.41 (0.45). For films with rough interfaces the effect is even greater, with ECE increasing by 57% (68%) for 75 (50) nm films with $A = d_D$ and $L = 15$ nm, leading to ECE = 0.50 (0.61). Although these values of ECE are still fairly poor considering that they set an upper limit on EQE, they do illustrate that the contribution of energy transfer to the CT state would be non-negligible in some cases. Particularly in some bulk heterojunction solar cells where the nano-structured domains are much smaller, small Förster transfer radii to the CT states at the interface between relatively pure domains could lead to much higher ECE than would be expected based solely on the exciton diffusion length.

To achieve higher ECE for energy transfer to a CT state, one would need a larger R_0. Given an energy donor with a higher quantum yield, one may be able to engineer a higher R_0 by selecting an appropriate molecule with which to pair it, e.g.

a non-fullerene acceptor, so the CT state energy is well-positioned.For instance a pair of materials with good overlap between fluorescence and CT absorbance with a PLQY of 90% and a 10 times larger CT absorption coefficient would give $R_0 = 3.4$ nm (See Appendix B, Figure S3for estimates of R_0 for different PLQY and ϵ). While this is still a relatively small value of R_0, it is large enough for significant improvement to ECE in thin films with energy cascades or for thicker films when they are nanostructured. In a thin film ($d_D = 13$ nm) with a flat interface, $R_0 = 3.4$ nm doubles the efficiency for $D \rightarrow C$ and $D \rightarrow A \rightarrow C$ cascades relative to diffusion only, leading to ECE = 0.67 and 0.72 respectively. For thicker, nanostructured films with a $D \rightarrow C$ cascade the effect is even greater, with ECE improving by 160% (145%) up to 0.85 (0.90) for 75 (50) nm films with $A = d_D$ and $L = 15$ nm. These values of ECE are high enough to achieve a solar cell with high EQE. When R_0^{D-CT} is large enough, the monolayer of CT states inherently at the electron donor-acceptor interface should act as highly efficient energy acceptors, helping to facilitate movement of the excitons directly into the CT states. Additionally, the relative dipole alignment of the CT states and the donors in the film could enhance the overall rate of energy transfer to the interface by up to four times for parallel dipole alignment (e.g. some conjugated molecules oriented edge-on to the interface) and even poorly aligned dipoles (e.g. conjugated molecules oriented face-on to the interface) would have overall rates

of transfer to the interfacial plane comparable the simulations (see Appendix B for calculations).

Based on the results of our simulations and calculations of R_0^{D-CT}, having a CT state that acts as a built in energy transfer cascade layer could significantly improve OPVs without the need to engineer a third molecule as an interfacial layer. Additionally the concept of CT states acting as energy acceptors has implications for understanding and explaining differences in performance of bulk heterojunction solar cells. To design a CT state with good energy transfer properties one would want: a donor with good quantum yield, a CT state with good oscillator strength, a Stokes shift suitable for the CT state energy, and ideally for the donor material to align edge-on with the DA interface such that the donor transition dipole is aligned pointing approximately in the direction perpendicular to the plane of the interface.

6.4 Conclusion

In conclusion, we have used KMC simulations to explore the use of energy transfer cascades to improve exciton collection in bilayer organic solar cells. For a monolayer of energy acceptor at the interface of the electron donor and acceptor, we find that high exciton collection efficiency can be achieved for moderately thick

bilayers (50 nm layers) when materials with high Förster transfer radii are employed. We also find that roughening the bilayer interface significantly improves exciton collection efficiency. This nanostructured morphology reduces the overall distance an exciton must travel to the interface leading to a small improvement to ECE without energy transfer, and a large improvement when energy transfer is included in the simulation. Additionally, the overall bilayer structure is maintained, which should be favorable for efficient charge transport.

Interestingly, we find that the $D \rightarrow A \rightarrow C$ energy cascade results in higher exciton collection efficiency than the $D \rightarrow C$ energy cascade. Although it may seem that energy transfer directly to C would be more efficient than energy transfer across C to A and then back to C, the significantly larger number of A chromophores than C chromophores actually makes the latter process more efficient, especially for larger values of R_0. However, increasing the thickness of the interfacial layer did not prove to be an effective exciton collection strategy relative to a monolayer because the increased exciton transfer to C did not offset the necessity for excitons to diffuse from the interior of the C-layer to an interface.

We also examined the efficacy of the donor-acceptor charge transfer state as an interfacial layer energy acceptor. In most cases, R_0^{D-CT} will be too small to contribute significantly to exciton collection (e.g. for P3HT-PCBM where $R_0^{P3HT-CT}$ is only 1.1 nm), but in materials with a larger R_0^{D-CT} (e.g. for APFO3-PCBM

where $R_0^{APFO3-CT}$ is 1.9 nm) we estimate that for an optimized CT state, R_0^{D-CT} could reasonably be as large as 3.4 nm. The CT state could therefore lead to small improvements in bilayer cells and significant improvements in nanostructured bilayers and bulk-heterojunctions.

Using one of the energy transfer cascades described here would theoretically allow for both good absorption and exciton collection, overcoming one of the greatest limitations in organic bilayer solar cells. By adding an energy cascade interfacial layer, a 7 nm donor or acceptor layer could be increased to 75 nm leading to better overall absorption without reducing exciton collection efficiency. Assuming the materials have good electron and hole mobility, increasing thickness should have a negligible effect on charge collection efficiency, resulting in thick solar cells with good EQE and PCE. This strategy may overcome the need for a nanostructured bulk heterojunction, simplifying the processing and optimization of organic solar cells.

Based on our simulations, the optimal design for a bilayer solar cell requires an energy transfer interfacial monolayer, a rough interface (RMS roughness approx. equal to film thickness) and a $D \rightarrow A \rightarrow C$ energy cascade, with R_0^{DA} and $R_0^{AC} > 5$ nm. Alternatively, if the interfacial layer is to be thick to absorb efficiently at complementary wavelengths, the optimal design requires a $D \rightarrow C$ and $A \rightarrow C$

energy cascade with rough interfaces and/or a large L_D for C so that excitons are not trapped in the C-layer.

Chapter 7

Conclusions

In conclusion, we have studied several aspects of organic and hybrid solar cells. We were able to achieve a deeper understanding of structural and morphological properties of donor (DTS and CDT) and acceptor (DTI) molecules that contribute to good solar cell performance. Both studies are excellent examples of why gaining good control over the final device morphology is essential for improving organic solar cell performance to economically viable levels.

First we performed a systematic study of *d*-CDT$(PTTh_2)_2$ and *d*-DTS-$(PTTh_2)_2$, two donor molecules that differ by only the bridgehead atom (carbon and silicon, respectively). We found that the largest difference between the compounds: their thermal behavior, largely explains the difference in their performance in solar cells. Both compounds have crystalline phases which grow with thermal annealing at temperatures below the melt. The crystalline domains grow larger for *d*-CDT$(PTTh_2)_2$ leading to domains that are too large for good perfor-

mance in BHJ OPVs. The results here have implications for device lifetime, as cold crystallization can limit the morphological stability at operational temperatures in practical solar cells.

Second we studied the non-fullerene acceptor, DTI and discovered why it does not perform well in annealed organic solar cells. Using photoluminescence quenching studies, we discovered that excitons formed in the DTI phase readily form charges, especially in annealed films. However electron transport in the DTI phase is highly anisotropic and the electron mobility across the film is very low, decreasing with annealing. The results suggest that DTI could be an even more successful acceptor if it could be engineered to preferentially orient face-on rather than edge-on to the substrate.

We were also able to apply a kinetic Monte Carlo simulation of Förster energy transfer to study both organic photovoltaics and dye sensitized solar cells. We were able to gain insights into how energy transfer can best be used to improve these solar cells and propose suggestions for improved chromophores and device architectures.

First, we used KMC simulations to examine energy transfer in several inhomogeneous donor-trap systems that are inaccessible by a direct analytical approach and studied time-dependent Förster transport and trapping in them. We deter-

mined that the SA to V_{donor} ratio was the parameter that best correlated with the initial trapping rate and stretched exponential fitting parameters to trapping.

Second, we used the KMC simulation to demonstrate how donor homotransfer can enhance exciton collection efficiency in dyes sensitized solar cells with energy relay dyes. We suggested that one could design a universal energy relay dye by selecting a highly soluble relay dye with large homotransfer and low quenching rates which would improved exciton transfer efficiency. This realization should make it easier to select relay/sensitizing dye pairs because the dyes can be chosen somewhat independently of one another (only considering the complementary absorption) allowing for an expanded parameter space of dyes that will lead to high efficiency solar cells.

Third, we have used KMC simulations to explore the use of energy transfer cascades to improve exciton collection in bilayer organic solar cells. We find that a monolayer of energy acceptor at the interface can lead to improvements in exciton collection, especially if the interface has nanostructured roughness. Interestingly, we find that the $D \rightarrow A \rightarrow C$ energy cascade results in higher exciton collection efficiency than the $D \rightarrow C$ energy cascade and that having a thicker layer of C is only marginally useful. We also examined the efficacy of the donor-acceptor charge transfer state as an interfacial layer energy acceptor and found that in optimal situations, it could lead to small improvements in bilayer cells and significant

improvements in nanostructured bilayers and bulk-heterojunctions. Using one of the energy transfer cascades would theoretically allow for both good absorption and exciton collection, overcoming one of the greatest limitations in organic bilayer solar cells. Energy cascades may also help overcome the need for a nanostructured bulk heterojunction, simplifying the processing and optimization of organic solar cells.

Designing organic solar cells with good exciton and charge transport is crucial for good performance as shown for DTS, CDT, and DTI and good exciton collection is essential in dye sensitized cells with energy relay dyes. This work computationally demonstrates several strategies to improve exciton transport and collection so that some materials design limitations for these devices can be lifted.

Bibliography

[1] Tang, C. W. *Appl. Phys. Lett.* **48**(2), 183–185 (1986).

[2] Green, M. A., Emery, K., Hishikawa, Y., Warta, W., and Dunlop, E. D. *Prog. Photovolt Res. Appl.* **21**, 827–837 (2013).

[3] Nelson, J. *Curr. Opin. Solid State Mater. Sci.* **6**(1), 87–95 February (2002).

[4] Dennler, G., Scharber, M. C., and Brabec, C. J. *Adv. Mater.* **21**(13), 1323–1338 April (2009).

[5] Peet, J., Senatore, M. L., Heeger, A. J., and Bazan, G. C. *Adv. Mater.* **21**(14-15), 1521–1527 April (2009).

[6] Padinger, F., Rittberger, R., and Sariciftci, N. *Adv. Funct. Mater.* **13**(1), 85–88 January (2003).

[7] Slota, J. E., He, X., and Huck, W. T. *Nano Today* **5**(3), 231–242 June (2010).

[8] O'Regan, B. and Grätzel, M. *Nature* **353**, 737–740 (1991).

[9] Yella, A., Lee, H.-W., Tsao, H. N., Yi, C., Chandiran, A. K., Nazeeruddin, M. K., Diau, E. W.-G., Yeh, C.-Y., Zakeeruddin, S. M., and Grätzel, M. *Science* **334**, 629–634 November (2011).

[10] Hardin, B. E., Snaith, H. J., and McGehee, M. D. *Nat. Photonics* **6**(3), 162–169 February (2012).

[11] Hardin, B. E., Hoke, E. T., Armstrong, P. B., Yum, J.-h., Comte, P., Torres, T., Fréchet, J. M. J., Nazeeruddin, M. K., Grätzel, M., and McGehee, M. D. *Nat. Photonics* **3**(June), 406–411 (2009).

[12] Hardin, B. E., Yum, J.-H., Hoke, E. T., Jun, Y. C., Péchy, P., Torres, T., Brongersma, M. L., Nazeeruddin, M. K., Grätzel, M., and McGehee, M. D. *Nano Lett.* **10**(8), 3077–3083 August (2010).

[13] Yum, J.-H., Hardin, B. E., Moon, S.-J., Baranoff, E., Nüesch, F., McGehee, M. D., Grätzel, M., and Nazeeruddin, M. K. *Angew. Chemie Int. Ed.* **48**(49), 9277–9280 January (2009).

[14] Yum, J.-H., Baranoff, E., Hardin, B. E., Hoke, E. T., McGehee, M. D., Nüesch, F., Grätzel, M., and Nazeeruddin, M. K. *Energy Environ. Sci.* **3**(4), 434–437 (2010).

[15] Mor, G. K., Basham, J., Paulose, M., Kim, S., Varghese, O. K., Vaish, A., Yoriya, S., and Grimes, C. A. *Nano Lett.* **10**(7), 2387–2394 July (2010).

[16] Margulis, G. Y., Lim, B., Hardin, B. E., Unger, E. L., Yum, J.-H., Feckl, J. M., Fattakhova-Rohlfing, D., Bein, T., Grätzel, M., Sellinger, A., and McGehee, M. D. *Phys. Chem. Chem. Phys.* **15**(27), 11306–11312 July (2013).

[17] Green, M. A., Emery, K., Hishikawa, Y., Warta, W., and Dunlop, E. D. *Prog. Photovolt Res. Appl.* **20**, 606–614 (2012).

[18] Li, G., Zhu, R., and Yang, Y. *Nat. Photonics* **6**(3), 153–161 February (2012).

[19] Brabec, C. J., Gowrisanker, S., Halls, J. J. M., Laird, D., Jia, S., and Williams, S. P. *Adv. Mater.* **22**(34), 3839–56 September (2010).

[20] He, Z., Zhong, C., Su, S., Xu, M., Wu, H., and Cao, Y. *Nat. Photonics* **6**, 591–595 (2012).

[21] Wei, G., Wang, S., Renshaw, K., Thompson, M. E., and Forrest, S. R. *ACS Nano* **4**(4), 1927–34 April (2010).

[22] Wei, G., Wang, S., Sun, K., Thompson, M. E., and Forrest, S. R. *Adv. Energy Mater.* **1**(2), 184–187 March (2011).

[23] Sun, Y., Welch, G. C., Leong, W. L., Takacs, C. J., Bazan, G. C., and Heeger, A. J. *Nat. Mater.* **11**(1), 44–8 January (2012).

[24] van der Poll, T. S., Love, J. A., Nguyen, T.-Q., and Bazan, G. C. *Adv. Mater.* **24**(27), 3646–9 July (2012).

[25] Walker, B., Tamayo, A. B., Dang, X.-D., Zalar, P., Seo, J. H., Garcia, A., Tantiwiwat, M., and Nguyen, T.-Q. *Adv. Funct. Mater.* **19**(19), 3063–3069 October (2009).

[26] Matsuo, Y., Sato, Y., Niinomi, T., Soga, I., Tanaka, H., and Nakamura, E. *J. Am. Chem. Soc.* **131**(44), 16048–50 November (2009).

[27] Shang, H., Fan, H., Liu, Y., Hu, W., Li, Y., and Zhan, X. *Adv. Mater.* **23**(13), 1554–7 April (2011).

[28] Walker, B., Kim, C., and Nguyen, T.-Q. *Chem. Mater.* **23**(3), 470–482 February (2011).

[29] Roncali, J. *Acc. Chem. Res.* **42**(11), 1719–30 November (2009).

[30] Riede, M., Mueller, T., Tress, W., Schueppel, R., and Leo, K. *Nanotechnology* **19**(42), 424001 October (2008).

[31] Li, Y., Guo, Q., Li, Z., Pei, J., and Tian, W. *Energy Environ. Sci.* **3**(10), 1427–1436 (2010).

[32] Zhou, J., Wan, X., Liu, Y., Zuo, Y., Li, Z., He, G., Long, G., Ni, W., Li, C., Su, X., and Chen, Y. *J. Am. Chem. Soc.* **134**(39), 16345–51 October (2012).

[33] Mishra, A. and Bäuerle, P. *Angew. Chemie Int. Ed.* **51**(9), 2020–67 February (2012).

[34] Wei, G., Xiao, X., Wang, S., Zimmerman, J. D., Sun, K., Diev, V. V., Thompson, M. E., and Forrest, S. R. *Nano Lett.* **11**(10), 4261–4 October (2011).

[35] Mayerhöffer, U., Deing, K., Gruss, K., Braunschweig, H., Meerholz, K., and Würthner, F. *Angew. Chem. Int. Ed. Engl.* **48**(46), 8776–9 January (2009).

[36] Bagnis, D., Beverina, L., Huang, H., Silvestri, F., Yao, Y., Yan, H., Pagani, G. A., Marks, T. J., and Facchetti, A. *J. Am. Chem. Soc.* **132**(12), 4074–5 March (2010).

[37] Loser, S., Bruns, C. J., Miyauchi, H., Ortiz, R. P., Facchetti, A., Stupp, S. I., and Marks, T. J. *J. Am. Chem. Soc.* **133**(21), 8142–5 June (2011).

[38] Yin, B., Yang, L., Liu, Y., Chen, Y., Qi, Q., Zhang, F., and Yin, S. *Appl. Phys. Lett.* **97**(2), 023303 (2010).

[39] Liu, Y., Wan, X., Yin, B., Zhou, J., Long, G., Yin, S., and Chen, Y. *J. Mater. Chem.* **20**(12), 2464–2468 (2010).

[40] Zhang, J., Deng, D., He, C., He, Y., Zhang, M., Zhang, Z.-G., Zhang, Z., and Li, Y. *Chem. Mater.* **23**(3), 817–822 February (2011).

[41] Günes, S., Neugebauer, H., and Sariciftci, N. S. *Chem. Rev.* **107**(4), 1324–38 May (2007).

[42] Moulé, A. J. and Meerholz, K. *Adv. Funct. Mater.* **19**(19), 3028–3036 October (2009).

[43] Treat, N. D., Shuttle, C. G., Toney, M. F., Hawker, C. J., and Chabinyc, M. L. *J. Mater. Chem.* **21**, 15224–15231 (2011).

[44] Chen, Y.-H., Huang, P.-T., Lin, K.-C., Huang, Y.-J., and Chen, C.-T. *Org. Electron.* **13**(2), 283–289 February (2012).

[45] Collins, B., Gann, E., Guignard, L., He, X., McNeill, C. R., and Ade, H. *J. Phys. Chem. Lett.* **1**, 3160–3166 (2010).

[46] Fitzner, R., Mena-Osteritz, E., Mishra, A., Schulz, G., Reinold, E., Weil, M., Körner, C., Ziehlke, H., Elschner, C., Leo, K., Riede, M., Pfeiffer, M., Uhrich, C., and Bäuerle, P. *J. Am. Chem. Soc.* **134**(27), 11064–7 July (2012).

[47] Lin, L.-Y., Chen, Y.-H., Huang, Z.-Y., Lin, H.-W., Chou, S.-H., Lin, F., Chen, C.-W., Liu, Y.-H., and Wong, K.-T. *J. Am. Chem. Soc.* **133**(40), 15822–5 October (2011).

[48] Steinmann, V., Kronenberg, N. M., Lenze, M. R., Graf, S. M., Hertel, D., Meerholz, K., Bürckstümmer, H., Tulyakova, E. V., and Würthner, F. *Adv. Energy Mater.* **1**(5), 888–893 October (2011).

[49] Mikroyannidis, J. A., Suresh, P., and Sharma, G. *Synth. Met.* **160**(9-10), 932–938 May (2010).

[50] Schulze, K., Uhrich, C., Schüppel, R., Leo, K., Pfeiffer, M., Brier, E., Reinold, E., and Bäuerle, P. *Adv. Mater.* **18**(21), 2872–2875 November (2006).

[51] Wagner, J., Gruber, M., Hinderhofer, A., Wilke, A., Bröker, B., Frisch, J., Amsalem, P., Vollmer, A., Opitz, A., Koch, N., Schreiber, F., and Brütting, W. *Adv. Funct. Mater.* **20**(24), 4295–4303 December (2010).

[52] Wei, G., Lunt, R. R., Sun, K., Wang, S., Thompson, M. E., and Forrest, S. R. *Nano Lett.* **10**(9), 3555–9 September (2010).

[53] Coropceanu, V., Cornil, J., da Silva Filho, D. A., Olivier, Y., Silbey, R., and Brédas, J.-L. *Chem. Rev.* **107**(4), 926–952 October (2007).

[54] Henson, Z. B., Welch, G. C., van der Poll, T., and Bazan, G. C. *J. Am. Chem. Soc.* **134**(8), 3766–79 February (2012).

[55] Welch, G. C., Perez, L. A., Hoven, C. V., Zhang, Y., Dang, X.-D., Sharenko, A., Toney, M. F., Kramer, E. J., Nguyen, T.-Q., and Bazan, G. C. *J. Mater. Chem.* **21**, 12700–12709 (2011).

[56] Peet, J., Kim, J. Y., Coates, N. E., Ma, W. L., Moses, D., Heeger, A. J., and Bazan, G. C. *Nat. Mater.* **6**(7), 497–500 July (2007).

[57] Hou, J., Chen, H.-Y., Zhang, S., Li, G., and Yang, Y. *J. Am. Chem. Soc.* **130**(48), 16144–5 December (2008).

[58] Chen, H.-Y., Hou, J., Hayden, A. E., Yang, H., Houk, K. N., and Yang, Y. *Adv. Mater.* **22**(3), 371–5 January (2010).

[59] Scharber, M. C., Koppe, M., Gao, J., Cordella, F., Loi, M. A., Denk, P., Morana, M., Egelhaaf, H.-J., Forberich, K., Dennler, G., Gaudiana, R., Waller, D., Zhu, Z., Shi, X., and Brabec, C. J. *Adv. Mater.* **22**(3), 367–70 January (2010).

[60] Risko, C., McGehee, M. D., and Brédas, J.-L. *Chem. Sci.* **2**(7), 1200 (2011).

[61] Yassar, A., Horowitz, G., Valat, P., Wintgens, V., Hmyene, M., Deloffre, F., Srivastava, P., Lang, P., and Gamier, F. *J. Phys. Chem.* **99**, 9155–9159 (1995).

[62] Gavezzotti, A. *Synlett* **2**, 201–214 (2002).

[63] Gavezzotti, A., Strutturale, C., and Milano, U. *J. Chem. Soc. Perkin Trans. 2* , 1399–1404 (1995).

[64] Gavezzotti, A. *Acta Crystallogr. B.* **66**(Pt 3), 396–406 June (2010).

[65] Collins, B. A., Li, Z., McNeill, C. R., and Ade, H. *Macromolecules* **44**, 9747–9751 (2011).

[66] Chabinyc, M. L. *Polym. Rev.* **48**, 463–492 (2008).

[67] Chabinyc, M. L., Toney, M. F., Kline, R. J., Mcculloch, I., and Heeney, M. *J. Am. Chem. Soc.* **129**(7), 3226–3237 (2007).

[68] Salleo, A., Kline, R. J., DeLongchamp, D. M., and Chabinyc, M. L. *Adv. Mater.* **22**(34), 3812–38 September (2010).

[69] Rogers, J. T., Schmidt, K., Toney, M. F., Kramer, E. J., and Bazan, G. C. *Adv. Mater.* **23**(20), 2284–8 May (2011).

[70] Baker, J. L., Jimison, L. H., Mannsfeld, S., Volkman, S., Yin, S., Subramanian, V., Salleo, A., Alivisatos, a. P., and Toney, M. F. *Langmuir* **26**(11), 9146–51 June (2010).

[71] Mannsfeld, S. C. B., Virkar, A., Reese, C., Toney, M. F., and Bao, Z. *Adv. Mater.* **21**(22), 2294–2298 June (2009).

[72] Mannsfeld, S. C. B., Tang, M. L., and Bao, Z. *Adv. Mater.* **23**(1), 127–31 January (2011).

[73] Breiby, D. W., Bunk, O., Andreasen, J. W., Lemke, H. T., and Nielsen, M. M. *J. Appl. Cryst.* **41**(2), 262–271 March (2008).

[74] Tong, M., Cho, S., Rogers, J. T., Schmidt, K., Hsu, B. B. Y., Moses, D., Coffin, R. C., Kramer, E. J., Bazan, G. C., and Heeger, A. J. *Adv. Funct. Mater.* **20**(22), 3959–3965 November (2010).

[75] Warren, B. E. *X-ray Diffraction.* Dover Publications, (1990).

[76] Rivnay, J., Noriega, R., Kline, R., Salleo, A., and Toney, M. *Phys. Rev. B* **84**(4), 1–20 July (2011).

[77] Smilgies, D.-M. *J. Appl. Cryst.* **42**(Pt 6), 1030–1034 December (2009).

[78] Leong, W. L., Welch, G. C., Seifter, J., Seo, J. H., Bazan, G. C., and Heeger, A. J. *Adv. Energy Mater.* **3**, 356–363 October (2013).

[79] Blakesley, J. C., Clubb, H. S., and Greenham, N. C. *Phys. Rev. B* **81**(4), 045210 January (2010).

[80] Street, R. A. *Phys. Rev. B* **84**(7), 075208 August (2011).

[81] Mikhnenko, O. V., Cordella, F., Sieval, a. B., Hummelen, J. C., Blom, P. W. M., and Loi, M. a. *J. Phys. Chem. B* **112**(37), 11601–4 September (2008).

[82] Presselt, M., Barenklau, M., Rosch, R., Beenken, W. J. D., Runge, E., Shokhovets, S., Hoppe, H., and Gobsch, G. *Appl. Phys. Lett.* **97**(25), 253302 (2010).

[83] Street, R. A., Song, K., Northrup, J., and Cowan, S. *Phys. Rev. B* **83**(16), 165207 April (2011).

[84] Kozub, D. R., Vakhshouri, K., Orme, L. M., Wang, C., Hexemer, A., and Gomez, E. D. *Macromolecules* **44**, 5722–5726 July (2011).

[85] Takacs, C. J., Sun, Y., Welch, G. C., Perez, L. A., Liu, X., Wen, W., Bazan, G. C., and Heeger, A. J. *J. Am. Chem. Soc.* **134**(40), 16597–606 October (2012).

[86] Cook, S., Ohkita, H., Kim, Y., Benson-Smith, J. J., Bradley, D. D., and Durrant, J. R. *Chem. Phys. Lett.* **445**(4-6), 276–280 September (2007).

[87] Pho, T. V., Toma, F. M., Tremolet de Villers, B. J., Wang, S., Treat, N. D., Eisenmenger, N. D., Su, G. M., Coffin, R. C., Douglas, J. D., Fréchet, J. M. J., Bazan, G. C., Wudl, F., and Chabinyc, M. L. *Adv. Energy Mater.* November (2013).

[88] Su, G. M., Pho, T. V., Eisenmenger, N. D., Wang, C., Wudl, F., Kramer, E. J., and Chabinyc, M. L. *J. Mater. Chem. A* **2**(6), 1781 (2014).

[89] Cisse, L., Destruel, P., Archambeau, S., Seguy, I., Jolinat, P., Bock, H., and Grelet, E. *Chem. Phys. Lett.* **476**(1-3), 89–91 July (2009).

[90] Sahoo, H. *J. Photochem. Photobiol. C Photochem. Rev.* **12**(1), 20–30 March (2011).

[91] Fung, B. K. and Stryer, L. *Biochemistry* **17**(24), 5241–8 November (1978).

[92] Yuan, L., Lin, W., Zheng, K., and Zhu, S. *Acc. Chem. Res.* **46**(7), 1462–73 July (2013).

[93] Demchenko, A. P. *Introduction to Fluorescence Sensing*. Springer, Netherlands, (2009).

[94] Fredrickson, G. H. and Helfand, E. *Macromolecules* **19**(10), 2601–2605 (1986).

[95] Farinha, J. P. S. and Martinho, J. M. G. *J. Phys. Chem. C* **112**(29), 10591–10601 July (2008).

[96] Yekta, A., Spiro, J. G., and Winnik, M. A. *J. Phys. Chem. B* **102**, 7960–7970 (1998).

[97] Gochanour, C. R., Andersen, H. C., and Fayer, M. D. *J. Chem. Phys.* **70**(9), 4254–4271 (1979).

[98] Loring, R. F., Andersen, H. C., and Fayer, M. D. *J. Chem. Phys.* **76**(4), 2015–2027 (1982).

[99] Blumen, A. and Klafter, J. *J. Chem. Phys.* **84**(3), 1397–1401 (1986).

[100] Drake, J. M., Klafter, J., and Levitz, P. *Science (80-.).* **251**(5001), 1574–1579 (2012).

[101] Ediger, M. D. and Fayer, M. D. *J. Chem. Phys.* **78**(5), 2518–2524 (1983).

[102] Ediger, M. D. and Fayer, M. D. *Macromolecules* **16**(12), 1839–1844 December (1983).

[103] Ediger, M. D. and Fayer, M. D. *J. Phys. Chem.* **88**(25), 6108–6116 (1984).

[104] Yekta, A., Duhamel, J., and Winnik, M. A. *Chem. Phys. Lett.* **235**, 119–125 (1995).

[105] Yekta, A., Winnik, M. A., Farinha, J. P. S., and Martinho, J. M. G. *J. Phys. Chem. A* **101**(96), 1787–1792 (1997).

[106] Farinha, J. P. S., Spiro, J. G., and Winnik, M. A. *J. Phys. Chem. B* **108**, 16392–16400 (2004).

[107] Brabec, C. J., Heeney, M., McCulloch, I., and Nelson, J. *Chem. Soc. Rev.* **40**(3), 1185–99 March (2011).

[108] Collins, B. A., Tumbleston, J. R., and Ade, H. *J. Phys. Chem. Lett.* **2**, 3135–3145 (2011).

[109] Scully, S., Armstrong, P., Edder, C., Fréchet, J., and McGehee, M. *Adv. Mater.* **19**(19), 2961–2966 October (2007).

[110] Liu, Y., Summers, M. a., Edder, C., Fréchet, J. M. J., and McGehee, M. D. *Adv. Mater.* **17**(24), 2960–2964 December (2005).

[111] Liu, Y.-X., Summers, M. A., Scully, S. R., and McGehee, M. D. *J. Appl. Phys.* **99**(9), 093521 (2006).

[112] Feron, K., Belcher, W. J., Fell, C. J., and Dastoor, P. C. *Int. J. Mol. Sci.* **13**(12), 17019–47 January (2012).

[113] Schlenker, C. W., Barlier, V. S., Chin, S. W., Whited, M. T., McAnally, R. E., Forrest, S. R., and Thompson, M. E. *Chem. Mater.* **23**(18), 4132–4140 September (2011).

[114] Cnops, K., Rand, B. P., Cheyns, D., and Heremans, P. *Appl. Phys. Lett.* **101**(14), 143301 (2012).

[115] Ichikawa, M., Takekawa, D., Jeon, H.-G., and Banoukepa, G. D. *Org. Electron.* **14**(3), 814–820 March (2013).

[116] Cnops, K., Rand, B. P., Cheyns, D., Verreet, B., Empl, M. A., and Heremans, P. *Nat. Commun.* **5**, 3406 1–6 January (2014).

[117] Griffith, O. L. and Forrest, S. R. *Nano Lett.* **14**, 23532358 (2014).

[118] Hardin, B. E., Sellinger, A., Moehl, T., Humphry-Baker, R., Moser, J.-E., Wang, P., Zakeeruddin, S. M., Grätzel, M., and McGehee, M. D. *J. Am. Chem. Soc.* **133**(27), 10662–10667 July (2011).

[119] Yum, J.-H., Hardin, B. E., Hoke, E. T., Baranoff, E., Zakeeruddin, S. M., Nazeeruddin, M. K., Torres, T., McGehee, M. D., and Grätzel, M. *ChemPhysChem* **12**(3), 657–661 February (2011).

[120] Driscoll, K., Fang, J., Humphry-Baker, N., Torres, T., Huck, W. T. S., Snaith, H. J., and Friend, R. H. *Nano Lett.* **10**, 4981–4988 November (2010).

[121] Itzhakov, S., Buhbut, S., Tauber, E., Geiger, T., Zaban, A., and Oron, D. *Adv. Energy Mater.* **1**(4), 626–633 July (2011).

[122] Cheon, J. H., Kim, S. A., Ahn, K.-S., Kang, M.-S., and Kim, J. H. *Electrochim. Acta* **68**, 240–245 April (2012).

[123] Humphry-Baker, N., Driscoll, K., Rao, A., Torres, T., Snaith, H. J., and Friend, R. H. *Nano Lett.* **12**(2), 634–639 February (2012).

[124] Eisenmenger, N. D., Delaney, K. T., Ganesan, V., Fredrickson, G. H., and Chabinyc, M. L. *J. Phys. Chem. C* **118**(26), 14098–14106 July (2014).

[125] Chatterjee, A. and Vlachos, D. G. *J. Comput. Mater. Des.* **14**(2), 253–308 February (2007).

[126] Baumann, J. and Fayer, M. D. *J. Chem. Phys.* **85**(7), 4087–4107 (1986).

[127] Poulsen, L., Jazdzyk, M., Communal, J.-E., Sancho-García, J. C., Mura, A., Bongiovanni, G., Beljonne, D., Cornil, J., Hanack, M., Egelhaaf, H.-J., and Gierschner, J. *J. Am. Chem. Soc.* **129**(27), 8585–93 July (2007).

[128] Olaya-Castro, A. and Scholes, G. D. *Int. Rev. Phys. Chem.* **30**(1), 49–77 January (2011).

[129] Dexter, D. *J. Chem. Phys.* **21**(5), 836–850 (1953).

[130] Förster, T. *Ann. Phys.* **437**(1-2), 55–75 (1948).

[131] Förster, T. *Zeitschrift Naturforsch. Tl. A* **4**, 321 (1949).

[132] Snaith, H. J. *Adv. Funct. Mater.* **20**(1), 13–19 January (2010).

[133] Dürr, M., Bamedi, A., Yasuda, A., and Nelles, G. *Appl. Phys. Lett.* **84**(17), 3397–3399 (2004).

[134] Kubo, W., Sakamoto, A., Kitamura, T., Wada, Y., and Yanagida, S. *J. Photochem. Photobiol. A Chem.* **164**(1-3), 33–39 June (2004).

[135] Hoke, E. T., Hardin, B. E., and McGehee, M. D. *Opt. Express* **18**(4), 3893–3904 February (2010).

[136] Bassler, H. *Phys. Status Solidi* **175**(1), 15–56 January (1993).

[137] McNeill, C. R., Westenhoff, S., Groves, C., Friend, R. H., and Greenham, N. C. *J. Phys. Chem. C* **111**(0), 19153–19160 (2007).

[138] Yang, F. and Forrest, S. R. *ACS Nano* **2**(5), 1022–1032 May (2008).

[139] Athanasopoulos, S., Hennebicq, E., Beljonne, D., and Walker, A. B. *J. Phys. Chem. C* **112**(30), 11532–11538 July (2008).

[140] Viani, L., Tolbod, L. P., Jazdzyk, M., Patrinoiu, G., Cordella, F., Mura, A., Bongiovanni, G., Botta, C., Beljonne, D., Cornil, J., Hanack, M., Egelhaaf, H.-J., and Gierschner, J. *J. Phys. Chem. B* **113**(31), 10566–10570 August (2009).

[141] Meng, L., Shang, Y., Li, Q., Li, Y., Zhan, X., Shuai, Z., Kimber, R. G. E., and Walker, A. B. *J. Phys. Chem. B* **114**(1), 36–41 January (2010).

[142] Meng, L., Wang, D., Li, Q., Yi, Y., Brédas, J.-L., and Shuai, Z. *J. Chem. Phys.* **134**(12), 124102 1–7 March (2011).

[143] Ansari-Rad, M., Abdi, Y., and Arzi, E. *J. Phys. Chem. C* **116**(5), 3212–3218 February (2012).

[144] Mohan, S. R., Singh, M. P., Joshi, M. P., and Kukreja, L. M. *J. Phys. Chem. C* **117**, 24663–24672 (2013).

[145] Maqsood, I., Cundy, L. D., Biesecker, M., Kimn, J.-h., Johnson, D., Williams, R., and Bommisetty, V. *J. Phys. Chem. C* **117**, 21086–21095 (2013).

[146] Lakowicz, J. R. *Principles of Fluorescence Spectroscopy.* Springer Science+Business Media, New York, 3rd edition, (2006).

[147] Bassler, H. and Schweitzer, B. *Acc. Chem. Res.* **32**(2), 173–182 (1999).

[148] Turro, N. J., Scaiano, J., and Ramamurthy, V. *Modern Molecular Photochemistry of Organic Molecules.* University Science Books, Sausalito, CA, (2010).

[149] Gochanour, C. R. and Fayer, M. D. *J. Phys. Chem.* **85**, 1989–1994 (1981).

[150] Du, H., Fuh, R.-C. A., Li, J., Corkan, L. A., and Lindsey, J. S. *Photochem. Photobiol.* **68**(2), 141–142 (1998).

[151] Dixon, J. M., Taniguchi, M., and Lindsey, J. S. *Photochem. Photobiol.* **81**, 212–213 (2005).

[152] Vu, T. T., Badre, S., Dumas-Verdes, C., Vachon, J.-J., Julien, C., Audebert, P., Senotrusova, E. Y., Schmidt, E. Y., Trofimov, B. A., Pansu, R. B., Clavier, G., and Meallet-Renault, R. *J. Phys. Chem. C* **113**, 11844–11855 (2009).

[153] Holmström, B. and Tegner, L. *Photochem. Photobiol.* **5**, 207–212 (1966).

[154] Wang, M., Grätzel, C., Zakeeruddin, S. M., and Grätzel, M. *Energy Environ. Sci.* **5**(11), 9394–9405 (2012).

[155] Salbeck, J., Bauer, J., Weissgrtel, F., and Bestgen, H. *Synth. Met.* **91**, 209–215 (1997).

[156] Funaki, T., Funakoshi, H., Kitao, O., Onozawa-Komatsuzaki, N., Kasuga, K., Sayama, K., and Sugihara, H. *Angew. Chemie Int. Ed.* **51**(30), 7528–7531 July (2012).

[157] Park, J., Viscardi, G., Barolo, C., and Barbero, N. *Chimia (Aarau).* **67**(3), 129–135 January (2013).

[158] Ono, T., Yamaguchi, T., and Arakawa, H. *Sol. Energy Mater. Sol. Cells* **93**, 831–835 June (2009).

[159] Macor, L., Fungo, F., Tempesti, T., Durantini, E. N., Otero, L., Barea, E. M., Fabregat-Santiago, F., and Bisquert, J. *Energy Environ. Sci.* **2**(5), 529–534 (2009).

[160] Maeda, T., Hamamura, Y., Miyanaga, K., Shima, N., Yagi, S., and Nakazumi, H. *Org. Lett.* **13**(22), 5994–5997 November (2011).

[161] Ameri, T., Khoram, P., Min, J., and Brabec, C. J. *Adv. Mater.* **25**(31), 4245–66 August (2013).

[162] Luhman, W. a. and Holmes, R. J. *Appl. Phys. Lett.* **94**(15), 153304 (2009).

[163] Menke, S. M. and Holmes, R. J. *Energy Environ. Sci.* **7**(2), 499 (2014).

[164] Menke, S. M., Luhman, W. A., and Holmes, R. J. *Nat. Mater.* **12**(2), 152–7 February (2013).

[165] Koeppe, R., Bossart, O., Calzaferri, G., and Sariciftci, N. *Sol. Energy Mater. Sol. Cells* **91**(11), 986–995 July (2007).

[166] Cook, S., Ohkita, H., Durrant, J. R., Kim, Y., Benson-Smith, J. J., Nelson, J., and Bradley, D. D. C. *Appl. Phys. Lett.* **89**(10), 101128 (2006).

[167] Albuquerque, R. Q., Hofmann, C. C., Köhler, J., and Köhler, A. *J. Phys. Chem. B* **115**(25), 8063–70 June (2011).

[168] Luhman, W. A. and Holmes, R. J. *Adv. Funct. Mater.* **21**(4), 764–771 February (2011).

[169] Scully, S. R. and McGehee, M. D. *J. Appl. Phys.* **100**(3), 034907 (2006).

[170] Groves, C. *Energy Environ. Sci.* **6**(5), 1546 (2013).

[171] Dastoor, P. C., Mcneill, C. R., Frohne, H., Foster, C. J., Dean, B., Fell, C. J., Belcher, W. J., Campbell, W. M., Officer, D. L., Blake, I. M., Thordarson, P., Crossley, M. J., Hush, N. S., and Reimers, J. R. *J. Phys. Chem. C* **111**, 15415–15426 (2007).

[172] Yang, F., Lunt, R. R., and Forrest, S. R. *Appl. Phys. Lett.* **92**(5), 053310 (2008).

[173] Huang, J.-H., Velusamy, M., Ho, K.-C., Lin, J.-T., and Chu, C.-W. *J. Mater. Chem.* **20**(14), 2820 (2010).

[174] Honda, S., Ohkita, H., Benten, H., and Ito, S. *Adv. Energy Mater.* **1**(4), 588–598 July (2011).

[175] Chen, M. C., Liaw, D. J., Huang, Y. C., Wu, H. Y., and Tai, Y. *Sol. Energy Mater. Sol. Cells* **95**, 2621–2627 (2011).

[176] Hesse, H. C., Weickert, J., Hundschell, C., Feng, X., Müllen, K., Nickel, B., Mozer, A. J., and Schmidt-Mende, L. *Adv. Energy Mater.* **1**(5), 861–869 October (2011).

[177] Cha, H., Chung, D. S., Bae, S. Y., Lee, M.-J., An, T. K., Hwang, J., Kim, K. H., Kim, Y.-H., Choi, D. H., and Park, C. E. *Adv. Funct. Mater.* **23**(12), 1556–1565 March (2013).

[178] Hwang, I., McNeill, C. R., and Greenham, N. C. *Synth. Met.* **189**, 63–68 March (2014).

[179] Ye, L., Xia, H., Xiao, Y., Xu, J., and Miao, Q. *RSC Adv.* **4**(3), 1087 (2014).

[180] Cooling, N., Burke, K. B., Zhou, X., Lind, S. J., Gordon, K. C., Jones, T. W., Dastoor, P. C., and Belcher, W. J. *Sol. Energy Mater. Sol. Cells* **95**(7), 1767–1774 July (2011).

[181] Cooling, N. a., Zhou, X., Sales, T. a., Sauer, S. E., Lind, S. J., Gordon, K. C., Jones, T. W., Burke, K. B., Dastoor, P. C., and Belcher, W. J. *Sol. Energy Mater. Sol. Cells* **98**, 308–316 March (2012).

[182] Sista, S., Yao, Y., Yang, Y., Tang, M. L., and Bao, Z. *Appl. Phys. Lett.* **91**(22), 223508 (2007).

[183] Zhang, G., Li, W., Chu, B., Chen, L., Yan, F., Zhu, J., Chen, Y., and Lee, C. S. *Appl. Phys. Lett.* **94**(14), 143302 (2009).

[184] Sim, M., Kim, J. S., Shim, C., and Cho, K. *Chem. Phys. Lett.* **557**, 88–91 February (2013).

[185] Honda, S., Ohkita, H., Benten, H., and Ito, S. *Chem. Commun.* **46**(35), 6596–8 September (2010).

[186] Honda, S., Yokoya, S., Ohkita, H., Benten, H., and Ito, S. *J. Phys. Chem. C* **115**, 11306–11317 (2011).

[187] Yang, L., Zhou, H., Price, S. C., and You, W. *J. Am. Chem. Soc.* **134**(12), 5432–5 March (2012).

[188] Liu, L. and Li, G. In *2011 11th IEEE Int. Conf. Nanotechnol.*, 332–336. Ieee, August (2011).

[189] Geens, W., Martens, T., Poortmans, J., Aernouts, T., Manca, J., Lutsen, L., Heremans, P., Borghs, S., Mertens, R., and Vanderzande, D. *Thin Solid Films* **451-452**, 498–502 March (2004).

[190] Mikhnenko, O. V., Kuik, M., Lin, J., van der Kaap, N., Nguyen, T.-Q., and Blom, P. W. M. *Adv. Mater.* **26**(12), 1912–7 March (2014).

[191] Scully, S. R. and McGehee, M. D. *J. Appl. Phys.* **100**(3), 034907 (2006).

[192] Lee, K. H., Schwenn, P. E., Smith, A. R. G., Cavaye, H., Shaw, P. E., James, M., Krueger, K. B., Gentle, I. R., Meredith, P., and Burn, P. L. *Adv. Mater.* **23**(6), 766–70 February (2011).

[193] Tao, C., Aljada, M., Shaw, P. E., Lee, K. H., Cavaye, H., Balfour, M. N., Borthwick, R. J., James, M., Burn, P. L., Gentle, I. R., and Meredith, P. *Adv. Energy Mater.* **3**(1), 105–112 January (2013).

[194] Watkins, P. K., Walker, A. B., and Verschoor, G. L. B. *Nano Lett.* **5**(9), 1814–8 September (2005).

[195] Scharber, M. C. and Sariciftci, N. S. *Prog. Polym. Sci.* **38**(12), 1929–1940 (2013).

[196] Yang, F., Shtein, M., and Forrest, S. R. *J. Appl. Phys.* **98**(1), 014906 (2005).

[197] Lee, K. H., Zhang, Y., Burn, P. L., Gentle, I. R., James, M., Nelson, A., and Meredith, P. *J. Mater. Chem. C* **1**(14), 2593 (2013).

[198] Vandewal, K., Oosterbaan, W. D., Bertho, S., Vrindts, V., Gadisa, A., Lutsen, L., Vanderzande, D., and Manca, J. V. *Appl. Phys. Lett.* **95**(12), 123303 (2009).

[199] Vandewal, K., Tvingstedt, K., Gadisa, A., Inganäs, O., and Manca, J. V. *Phys. Rev. B* **81**(12), 125204 March (2010).

[200] Drori, T., Sheng, C.-X., Ndobe, a., Singh, S., Holt, J., and Vardeny, Z. *Phys. Rev. Lett.* **101**(3), 037401 July (2008).

[201] Vandewal, K., Albrecht, S., Hoke, E. T., Graham, K. R., Widmer, J., Douglas, J. D., Schubert, M., Mateker, W. R., Bloking, J. T., Burkhard, G. F., Sellinger, A., Fréchet, J. M. J., Amassian, A., Riede, M. K., McGehee, M. D., Neher, D., and Salleo, A. *Nat. Mater.* **13**(1), 63–8 January (2014).

[202] Tvingstedt, K., Vandewal, K., Gadisa, A., Zhang, F., Manca, J., and Inganäs, O. *J. Am. Chem. Soc.* **131**(33), 11819–24 August (2009).

[203] Lee, J., Vandewal, K., Yost, S. R., Bahlke, M. E., Goris, L., Baldo, M. A., Manca, J. V., and Van Voorhis, T. *J. Am. Chem. Soc.* **132**(34), 11878–80 September (2010).

[204] Cook, S., Furube, A., and Katoh, R. *Energy Environ. Sci.* **1**(2), 294 (2008).

[205] Sun, Y., Takacs, C. J., Cowan, S. R., Seo, J. H., Gong, X., Roy, A., and Heeger, A. J. *Adv. Mater.* **23**(19), 2226–30 May (2011).

[206] Holzwarth, U. and Gibson, N. *Nat. Nanotechnol.* **6**(9), 534 September (2011).

[207] Ho Choi, C., Kertesz, M., and Karpfen, A. *J. Chem. Phys.* **107**(17), 6712–21 (1997).

[208] Champagne, B., Perpete, E. A., van Gisbergen, S. J. A., Baerends, E.-F., Snijders, J. G., Soubra-Ghaoui, C., Robins, K. A., and Kirtman, B. *J. Chem. Phys.* **109**(23), 10489–98 (1998).

[209] Dkhissi, A., Beljonne, D., Lazzaroni, R., Louwet, F., Groenendaal, L., and Bredas, J. L. *Int. J. Quantum Chem.* **91**(3), 517–523 December (2003).

[210] Pal, S. K., Kesti, T., Maiti, M., Zhang, F., Inganäs, O., Hellström, S., Andersson, M. R., Oswald, F., Langa, F., Osterman, T., Pascher, T., Yartsev, A., and Sundström, V. *J. Am. Chem. Soc.* **132**(35), 12440–51 September (2010).

[211] Jarzab, D., Lu, M., Nicolai, H. T., Blom, P. W. M., and Loi, M. A. *Soft Matter* **7**(5), 1702 (2011).

[212] Quist, P. A. C., Sweelssen, J., Koetse, M. M., Savenije, T. J., and Siebbeles, L. D. A. *J. Phys. Chem. C* **111**, 4452–4457 (2007).

[213] Inganas, O., Svensson, M., Gadisa, A., Zhang, F., Persson, N., Wang, X., and Andersson, M. *Appl. Phys. A Mater. Sci. Process.* **79**(1), 31–35 June (2004).

[214] Fredrickson, G. H. *J. Chem. Phys.* **88**(9), 5291 (1988).

Appendices

Appendix A

Supporting Information for Chapter 2

A.1 Synthesis of *d*-DTS($PTTh_2$)$_2$ and *d*-CDT-($PTTh_2$)$_2$

Synthesis and characterization of *d*-DTS($PTTh_2$)$_2$ has previously been reported,[55] while *d*-CDT($PTTh_2$)$_2$ was prepared in an identical fashion and is described below. Analytical measurements were performed as previously reported.[55] In a N_2 filled glove box a 20 mL microwave tube was charged with 4,4-*bis*(2-ethylhexyl)-2,6-*bis*(trimethylstannyl)-4H-cyclopenta[2,1-*b*:3,4-*b*']dithiophene ((CDT_{EH}-$SnMe_3$)$_2$, 520 mg, 0.71 mmol), 7-bromo-4-(5-(5-hexylthiophen-2-yl)thiophen-2-yl)-[1,2,5]thiadiazolo[3,4-c]pyridine ($HexTh_2PTBr$, 640 mg, 1.4 mmol), $Pd(PPh_3)_4$ (0.025 g, 0.02 mmol), toluene (15 mL), and sealed with a teflon cap. The reaction mixture was heated to 120°C for 3 minutes, 140°C for 3 minutes, and 175°C for 120 minutes, using a Biotage microwave reactor. Upon cooling, the residue was passed through a short silica plug eluting with $CHCl_3$ (5% Et_3N) (500 mL). All volatiles were removed in vacuo to give the crude product as a purple solid. The material was then loaded onto silica and purified by flash chromatography using a hexanes/$CHCl_3$ (5% Et_3N) gradient. After fraction collection and solvent removal a purple solid was obtained. Purification by silica column chromatography was carried out twice. The solid was slurried in MeOH (300 mL), sonicated for 10 minutes, and filtered. The solid was washed with copious amounts of MeOH-Hexanes (50:50), MeOH, Acetone and then dried under vacuum for 24 hours. The product was collected as purple solid. Recovered yield: 710 mg (85%). **1H NMR**: ($CDCl_3$): δ 8.83 (s, 2H, PT-CH), 8.58 (d, $^3J_{H-H}$ = 5 Hz, 2H, Th-CH), 8.10 (t, 2H, SDT-CH), 7.25 (d, $^3J_{H-H}$ =

5 Hz, 2H Th-CH), 7.19 (d, $^3J_{H-H}$ = 5 Hz, 2H Th-CH), 6.76 (m, 2H, Th-CH), 2.84 (m, 4H Th-CH_2), 2.08 (m, 4H, CH_2), 1.72 (tt, 3JH-H = 6 Hz, 4H, CH_2), 1.42 (m, 4H, CH), 1.35 (m, 8H, CH_2), 1.05-1.00 (br m, 14H, CH_2), 0.92 (m, 6H, CH_2), 0.84 (m, 4H, CH_2), 0.66 (m, 12H, CH_3). **Elemental analysis**: calculated for $C_63H_72N_6S_8$: C, 64.68; H, 6.20; N, 7.18. Found: C, 64.5; H, 6.30; N, 7.48 %. $\mathbf{T}_d$: (5% mass loss at 398°C under N_2). **LSMS (FD)**: m/z, calculated for $C_63H_72N_6S_8$ (M^+): 1168; found: 1168 (M^+), 584 (M^{2+}).

A.2 Sample Preparation

Indium tin oxide (ITO) coated glass substrates (ITO layer 140 nm thick) were obtained from Thin Film Devices (Anaheim, CA). All substrates were cleaned in an ultrasonic bath of acetone followed by 2-propanol for 20 min each and dried with a stream of nitrogen. Molybdenum oxide (MoO_3) (obtained from Sigma Aldrich) was thermally evaporated onto the cleaned glass/ITO substrates at a rate of about 0.3 /s to a final thickness of 10 nm. Further experimentation to determine the stoichiometry of the MoO_x film was not performed, but other work suggests that it is MoO_3.[205]

Samples used in the *in situ* UV-Vis, polarized optical microscopy, and GIWAXS studies were prepared by spin casting (2500 rpm, 45 s) 12 mg/mL solutions of *d*-DTS($PTTh_2$)$_2$ or *d*-CDT($PTTh_2$)$_2$ dissolved in chloroform (Sigma-Aldrich, St. Louis, MO) directly onto the glass/ITO/MoOx substrates. For the blend films, $PC_{71}BM$, obtained from Nano-C (Westwood, MA), was added to the *d*-DTS($PTTh_2$)$_2$ or *d*-CDT($PTTh_2$)$_2$ solutions to create a final small molecule:$PC_{71}BM$ ratio of 3:2 by mass, and the resulting solution was spin coated onto the substrates using the same conditions. All solutions were stirred at 50°C overnight before spin coating to allow for complete dissolution. Solution preparation and spin coating were done in a glove box in a N_2 environment.

Photovoltaic devices were prepared by spin coating *d*-DTS($PTTh_2$)$_2$:$PC_{71}BM$ or *d*-CDT($PTTh_2$)$_2$:$PC_{71}BM$ solutions onto glass/ITO/MoO_x substrates as previously described. Directly after spin coating, 90 nm thick aluminum contacts were thermally evaporated on top of the active layer.

A.3 Differential scanning calorimetry

DSC measurements were carried out on a TA Instruments DSC 2920 differential scanning calorimeter. About 4 mg of material was used in Tzero aluminum pans. Each sample was first equilibrated at 25°C then heated at 10°C min^{-1} to

300°C (for *d*-DTS($PTTh_2$)$_2$based samples) or 200°C (for *d*-CDT($PTTh_2$)$_2$based samples) to erase any thermal history. Each sample was then cooled at a rate of 2°C min^{-1} to 0°C, and heated again at 2°C min^{-1} to 200°C or 300°C, accordingly. The first heating run is not shown in the figures.

A.4 UV-Visible absorption measurements

Solution UV-visible spectroscopy was conducted using either a Beckman Coulter DU 800 series or a Perkin Elmer Lambda 750 spectrophotometer at room temperature. Solutions were prepared in chloroform in an N_2 atmosphere in Teflon capped 1 mm quartz cuvettes. *In situ* UV-Vis measurements were performed in ambient with an Ocean Optics DH-2000 UV-VIS-NIR Lightsource and an Ocean Optics HR 2000+ High Resolution Detector. Samples were prepared by spin coating solutions of *d*-DTS($PTTh_2$)$_2$, *d*-CDT($PTTh_2$)$_2$, *d*-DTS($PTTh_2$)$_2$:$PC_{71}BM$, or *d*-CDT($PTTh_2$)$_2$:$PC_{71}BM$ onto glass/ITO/MoO_x substrates as described previously. An Instec heating stage connected to a temperature control unit was mounted between optical fibers connected to the light source and detector. The heating stage is equipped with an opening that allows light to pass through the sample and the stage. The entire setup was enclosed with black cardboard to block ambient light. In this way, the temperature of the samples can be controlled by the hot stage as the absorption spectra are simultaneously collected. A bare glass/ITO/MoO_x substrate was used as a reference, and spectra were taken with a halogen source at an ∼85 ms integration time and data collected with SpectraSuite software.

A.5 In-situ UV-visible absorption studies of thin films

To gain a better understanding of the changes upon thermal annealing in the two compounds, we have measured the UV-visible absorption in-situ as the films were heated. Thin films of *d*-DTS($PTTh_2$)$_2$ and *d*-CDT($PTTh_2$)$_2$ and their blends with $PC_{71}BM$ were spin coated onto glass/ITO/MoO_x substrates to mimic device architecture, sans the aluminum cathode. As temperature was sequentially increased, it was generally observed that the overall intensity of the absorption maxima (500-800 nm) increased. This is most noticeable for the *d*-DTS($PTTh_2$)$_2$:$PC_{71}BM$ films compared to *d*-CDT($PTTh_2$)$_2$:$PC_{71}BM$. Interestingly, it is during slow cooling that the intensity of the lower energy interaction peak (∼750

nm) increases most significantly, and the overall intensity does not decrease during this cooling process.

A.6 Polarized Optical Microscopy

Optical microscope images were taken on an Olympus BH-2 microscope. The samples were illuminated from below. A polarizer was placed directly above the light source and another in between the lens and the eyepiece. A cross-polarized setup was used, i.e. the lower polarizer was rotated to be orthogonal to the top polarizer, resulting in a dark background image. Bright spots seen in the sample are a result of rotation of polarized light by crystallites.

A.7 Grazing Incidence Wide Angle X-ray Scattering

GIWAXS experiments were performed at the Stanford Synchrotron Radiation Laboratory (SSRL) on beamline 11-3. An area detector, MAR 2300 image plate, was used for 2D collection. The energy of the incident X-ray beam was 12.7 keV, and the angle of incidence was 0.14° with a 40 cm sample to detector distance, above the critical angle of the organic film but below the critical angle of the substrate. Samples were kept under a helium atmosphere to reduce X-ray damage and background scattering; exposure times of 15 s to 30 s were used. Peak analysis was done in the WxDiff software.[72]

A peak fitting analysis of the GIWAXS data was done with the Scherrer equation to determine crystallite size. However, since diffraction peak width decreases with increasing crystallite size, the Scherrer equation can only be applied for crystallites up to a certain size because it can become difficult to differentiate between peak broadening due to crystallite size and broadening from other factors.[206] It is important to consider these resolution-limiting factors and apply them to the grazing-incidence geometry.[77] As noted in the paper, some of the *d*-CDT($PTTh_2$)$_2$ crystallites were too large for the Scherrer analysis to give reasonable results.

A.8 Transmission Electron Microscopy

Selected Area Electron Diffraction was performed on an FEI T20 operating at 200 kV. High-Resolution Transmission Electron Microscopy (HR-TEM) and Scanning Transmission Electron Microscopy (STEM) were performed on an FEI Titan

operating at 300 kV. HR-TEM images were taken under approximately parallel illumination and while using a low-dose imaging procedure involving electronic shifting of the beam to minimize damage. The defocus was nominally set to maximize the instrumental transfer function over wavelengths extending from 1.5 nm to 4 nm. We note, particularly for the highly crystalline samples, the practical dosage is limited not by fading of the diffraction patterns but by damage induced drift of the sample during exposure that reduces the observed signal. The overlays were created using the algorithm detailed in Takacs et. al..[85] The threshold for detection of the lattice planes was set to greater than 7 sigma above the shot noise background of the camera. The STEM images were taken using a 2.3 mrad convergence angle. While this effectively reduces the spot size to ∼0.5 nm, it allows for the collection angle to be reduced allowing visualization of the 2.0 nm lattice planes. The sensitivity is likely less than HR-TEM but sample drift during acquisition is no longer an issue, making imaging conditions easily reproducible. We are unaware of any reports where this low of a convergence angle has been used to image similar lattice features in other conjugated materials.

An interesting region of the as-cast *d*-CDT($PTTh_2$)$_2$BHJ and the Fourier transform of the same region are shown in Figure A.14a and Figure A.14b, respectively. The Fourier transform shows broad peaks highlighted in the orange/red bands (1.75/2.0 nm) along with a comparatively narrow peak within the green band (2.7 nm). Additional analysis was performed to spatially resolve the local packing behavior and to create the orange/red overlay and green overlay in Figure A.14c and Figure A.14d, respectively. In the case of the orange/red overlay, the spatial structure seems to be highly variable within the crystal showing changes in the direction of the lattice planes along with what may be changes in the packing structure even within the crystal. The green overlay appears to lie in a single direction and overlap much of the red region suggesting these may be part of the same structure.

A.9 *In situ* current-voltage measurements during thermal annealing

The BHJ solar cells were annealed on a hotplate as dark and light J-V curves were continuously measured. The devices were illuminated with an array of 14 red (620 nm) 1 W LumiLEDs mounted above a digitally controlled hotplate in a N_2 glove box. The intensity was set to give approximately the short circuit current measured under one sun of simulated AM 1.5 light. However, due to variations of the light intensity between experiments, all *in situ* annealing plots

show the current normalized by the current of the as cast sample under the LED illumination. Devices were placed on glass slides attached to a metal plate, and electrically connected by clamping with a dip-clip. A thermocouple was attached to the glass slide next to the device that allowed for continuous monitoring of device temperature. The hot plate was covered with a large glass petri dish to prevent temperature fluctuations due to air currents in the glove box. Two types of in-situ J-V measurements were made: temperature ramp studies, and constant temperature studies. For temperature ramp studies, devices were first mounted, connected, and placed on the hotplate at room temperature (ITO side face up), and then the hotplate was set to ramp at 200°C/hr while J-V curves and temperature were continuously monitored using a Keithley 2400 SMU and a thermocouple. For constant temperature experiments, the metal base and glass slide were pre-heated on the hotplate to the desired temperature prior to connecting the device. The metal base was temporarily removed from the hotplate as the device was clipped into place, which results in slight cooling of the glass slide, but the desired temperature was reached again in about 3 mins after being replaced onto the hotplate. J-V curves and temperature were monitored as for the temperature ramp studies.

A.10 Orbital and Excited State Calculations

Calculations for geometry optimization and orbitals were done with Gaussian 03 at the RB3LYP level of theory with a 6-31G(d) basis set. Orbitals were plotted in Avogadro. The first 10 excited states were then determined with a single point TDDFT calculation (Table A.1 and A.2). The excitations in the calculation were shifted ∼0.35 eV lower in energy than what was found experimentally, which is often the case in TDDFT calculations where the delocalization of the conjugated system is over-estimated.[207–209]

A.11 Transient Photocurrent (TPC) Measurement

TPC measurements[83] were performed on a *d*-DTS($PTTh_2$)$_2$:$PC_{71}BM$ OPV device after annealing. The device was held at a given bias and pulsed with light from an array of 14 red (620 nm) 1 W LumiLEDs. The measurement was done for the short circuit condition to -1.0 V in increments of 0.1V. The current transients were collected for the device at 27°C, then heated to 40°C, 53°C, and 68°C, and then cooled again to 28°C. The current transients were integrated to determine

the amount of extracted charge and fit with an exponential function to determine the time constant.

A.12 Grazing Incidence Wide-Angle X-Ray Scattering

Values for the d-spacings and crystallite correlation lengths for both as-cast and annealed pristine and BHJ films are enumerated in Table A.3 and Table A.4. As noted in the main text of the manuscript, Scherrer analysis can be somewhat inaccurate in determining correlation lengths since paracrystalline disorder and lattice-parameter fluctuations can contribute significantly to peak breadth.[76] Contributions from disorder can be determined by analyzing the peak breadth and peak shape as a function of diffraction order for a family of peaks, e.g. (h00). One way to do this is to fit peaks with a pseudo-Voigt profile, a linear combination of a Lorentzian and a Gaussian, both with the same full-width-at-half-maximum (FWHM),

$$I(q) = I_0 + A\left[\eta\frac{2}{\pi}\frac{\Delta q}{(4(q-q_c)^2+\Delta q^2)} + (1-\eta)\frac{\sqrt{4ln(2)}}{\sqrt{\pi}\Delta q}\exp\left[-\frac{4ln(2)}{\Delta q^2}(q-q_c)^2\right]\right] \tag{A.1}$$

where I_0 is the intensity offset, A the amplitude, q_c the center position of the peak, Δq the FWHM, and η the mixing parameter. If the FWHM increases with diffraction order, then disorder is contributing to the peak width. The value of η can be used to estimate the contribution from paracrystallinity. If η is close to unity, then the peak is Lorentzian and paracrystalline disorder dominates. If η is close to zero, the peak is Gaussian and lattice-parameter fluctuations dominate. Since the crystal structure of the molecules studied here is not known, it is difficult to index the reflections and isolate a family of peaks. Also, the higher order peaks that do show up in some of the 2D scattering images have relatively low intensity, making analysis difficult. However, a rough estimate is done for pristine *d*-DTS-$(PTTh_2)_2$ films where the reflections along q_z are likely to be of the same family, (h00). Figure A.7 shows that the FWHM for both as-cast and annealed *d*-DTS-$(PTTh_2)_2$ films increased with peak order, suggesting a disorder component. The η term generally lies between zero and one, indicating contributions from both paracrystallinity and lattice-parameter fluctuations, although the as-cast film may have a stronger paracrystalline contribution. The error in the data at high q makes drawing further conclusions difficult, but this preliminary analysis suggests that

disorder likely contributes to peak breadth in the materials of interest here, and this should be considered when referring to results from the Scherrer equation.

Pristine *d*-DTS(PTTh$_2$)$_2$ films

The scattering from as-cast films of *d*-DTS(PTTh$_2$)$_2$ shows similar diffraction peaks to those observed previously (Figure A.7).[55] There are prominent features at q = 0.33 Å^{-1} (nearly out-of-plane) and at q = 1.80 Å^{-1} (in plane) and a broad, isotropic diffuse ring present at q ≈ 1.6 Å^{-1} attributed to amorphous scattering. Weaker peaks near the q_z axis and off-axis are also observed and are likely higher order diffraction peaks. As indicated in the main body of the manuscript, we use the convention of the previous publication and refer to the peak at q = 0.33 Å^{-1} as the (100) reflection, and the q = 1.8 Å^{-1} reflection as the (010).1 Based on the in-plane portion of the (100) peak, the alkyl stacking has a d-spacing of about 20.2 Å, and the $\pi - \pi$ stacking in the [010] direction has a *d*-spacing of 3.5 Å.

Sector plots of the scattering intensity show a broad angular distribution, but with a dominant texture such that the a* axis is approximately aligned along q_z, consistent with an edge-on orientation of the conjugated core relative to the substrate. Using peaks along q_{xy}, we determine a correlation length of at least 26.1 nm for the [100] population oriented along q_{xy} and a correlation length of 32.1 nm for the [010] direction.

Annealing neat *d*-DTS(PTTh$_2$)$_2$ films at 80°C leads to noticeable morphological changes. Looking first at pristine *d*-DTS(PTTh$_2$)$_2$, the diffuse amorphous ring that was present in the as-cast film vanishes upon annealing. Also, higher order reflections, which are more pronounced and have narrower peak widths, are visible, suggesting improved quality and greater size of the crystallites. No significant changes in crystallographic texture were observed. The (100) spacing remained essentially the same (d = 20.7 Å), as did the (010).

Sector plots (Figure A.9 and Figure Figure A.10) reveal that the (100) and (010) reflections of *d*-DTS(PTTh$_2$)$_2$:PC$_{71}$BM both show a broader angular distribution relative to pristine films, suggesting that PC$_{71}$BM disrupts the preferential orientation of the crystallites in as-cast films. For as-cast samples, addition of PC$_{71}$BM results in a slight decrease in the *d*-spacing of the (100) peak for crystallites with [100] perpendicular to the substrate, but a slight increase for crystallites with the [100] axis parallel to the substrate. Addition of PC$_{71}$BM leads to a decrease in crystallite size for both as-cast and annealed *d*-DTS(PTTh$_2$)$_2$ films.

Pristine *d*-CDT(PTTh$_2$)$_2$ films

In as-cast *d*-CDT(PTTh$_2$)$_2$ film (Figure A.8), there is a peak at q = 0.39 Å^{-1} near the out of plane direction, corresponding to a *d*-spacing of 16.0 Åfor crystallites with [100] perpendicular to the substrate, noticeably less than the spacing of the [100] of *d*-DTS(PTTh$_2$)$_2$, and the (010) peak occurs at q = 1.75

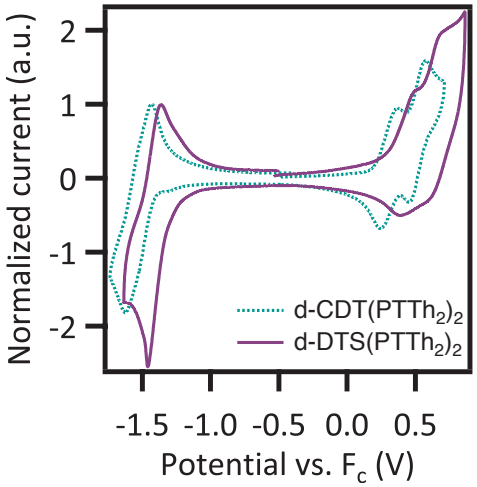

Figure A.1: Cyclic voltammetry plots of *d*-DTS($PTTh_2$)$_2$ (solid purple) and *d*-CDT($PTTh_2$)$_2$ (dotted green) obtained in CH_2Cl_2 solution.

Å^{-1} (d-spacing of 3.6 Å). Higher order peaks are visible suggesting a higher degree of structural order as well. The correlation length of the as cast *d*-CDT($PTTh_2$)$_2$ film for the (100) direction is ∼15-25 nm. For the as cast pristine film, the (100) peak has high intensity out of plane. In the annealed pristine *d*-CDT($PTTh_2$)$_2$ films, many higher order reflections are visible, and central spots of high intensity within them suggest an overall improvement in crystallinity and crystal correlation length. The sector plot (Figure A.9 and Figure A.10) shows significant angular broadening of most of the reflections, indicating that there is still a distribution of crystallite orientations. The *d*-spacing from the (100) and (010) reflections remained similar, but the crystallite correlation length increased to roughly 30-40 nm in the [100] direction. The in-plane crystallite correlation length in the [010] direction increased dramatically to about 100 nm, and this is near the maximum size limit where Scherrer analysis applies.

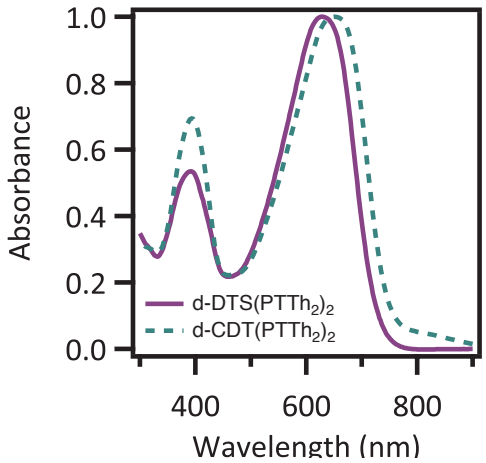

Figure A.2: UV-visible absorption spectra of *d*-DTS($PTTh_2$)$_2$ and *d*-CDT-($PTTh_2$)$_2$ in chloroform solution.

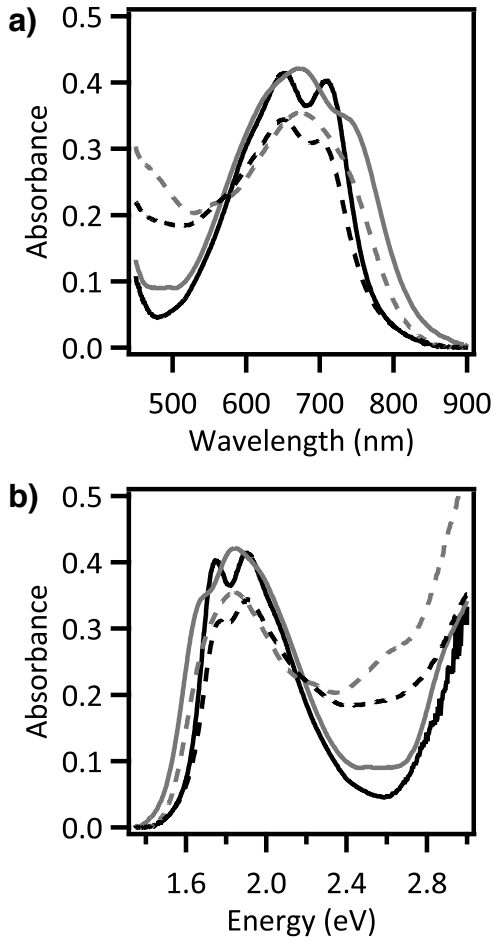

Figure A.3: The UV-Visible absorption spectrum a) vs. wavelength (nm) and b) vs. energy (eV) for as cast films of *d*-DTS($PTTh_2$)$_2$ (black solid) *d*-CDT($PTTh_2$)$_2$ (grey solid) and the blends with $PC_{71}BM$ (black and grey dashed, respectively). Films were on glass/ITO/MoO_x with the substrate subtracted as a reference.

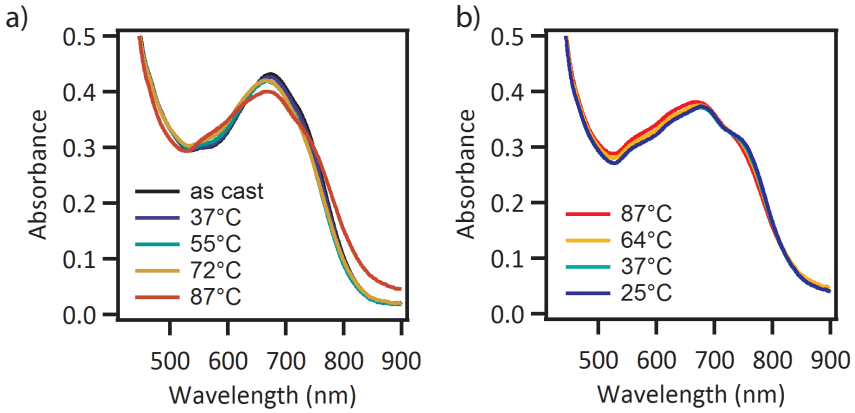

Figure A.4: UV-Visible absorbance spectra measured during (a) heating and (b) cooling of a *d*-CDT(PTTh$_2$)$_2$:PC$_{71}$BM film on a glass/ITO/MoO$_x$ substrate.

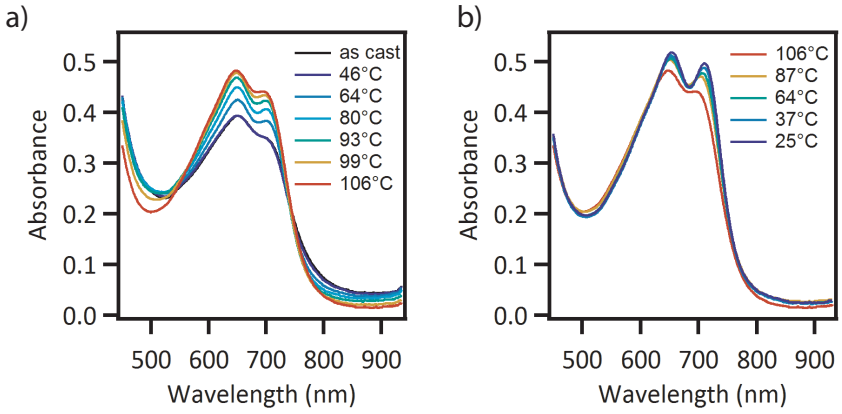

Figure A.5: UV-visible absorbance spectra obtained during (a) heating and (b) cooling of a *d*-DTS(PTTh$_2$)$_2$:PC$_{71}$BM film on a glass/ITO/MoO$_x$ substrate.

Excited State	Energy (eV)	Wavelength (nm)	f	Orbital Transition	λ
1	1.547	801.44	1.2987	HOMO $\rightarrow$ LUMO	0.70141
2	1.7502	708.41	0.0666	HOMO $\rightarrow$ LUMO+1	0.69789
3	2.1365	580.32	0.2548	HOMO-1 $\rightarrow$ LUMO	0.69162
4	2.3146	535.67	0.0318	HOMO-1 $\rightarrow$ LUMO+1	0.69405
5	2.504	495.14	0.0499	HOMO-2 $\rightarrow$ LUMO	0.67171
				HOMO $\rightarrow$ LUMO+2	-0.16929
				HOMO $\rightarrow$ LUMO+4	0.10383
6	2.6858	461.62	0.8125	HOMO-2 $\rightarrow$ LUMO	0.15614
				HOMO $\rightarrow$ LUMO+2	0.6752
7	2.7119	457.19	0.0274	HOMO-2 $\rightarrow$ LUMO+1	0.69385
8	3.066	404.38	0.3672	HOMO $\rightarrow$ LUMO+3	0.69013
9	3.1147	398.06	0.0005	HOMO-3 $\rightarrow$ LUMO	0.68399
10	3.157	392.73	0.0614	HOMO-2 $\rightarrow$ LUMO	-0.10872
				HOMO $\rightarrow$ LUMO+4	0.67818

Table A.1: Calculated excited states for *d*-DTS($PTTh_2$)$_2$, with the energy, wavelength, oscillator strength (f), orbital transition(s) contributing to the excited state, and weighting (λ) of each orbital transition.

Excited State	Energy (eV)	Wavelength (nm)	f	Orbital Transition	λ
1	1.5033	824.73	1.452	HOMO $\rightarrow$ LUMO	0.70175
2	1.7074	726.15	0.0315	HOMO $\rightarrow$ LUMO+1	0.69824
3	2.1314	581.71	0.1697	HOMO-1 $\rightarrow$ LUMO	0.69006
				HOMO $\rightarrow$ LUMO+3	0.10554
4	2.3253	533.19	0.0322	HOMO-1 $\rightarrow$ LUMO+1	0.69416
5	2.4864	498.65	0.0545	HOMO-2 $\rightarrow$ LUMO	0.68527
				HOMO $\rightarrow$ LUMO+4	0.11879
6	2.7058	458.21	0.0271	HOMO-2 $\rightarrow$ LUMO+1	0.69387
7	2.7191	455.98	1.139	HOMO $\rightarrow$ LUMO+2	0.69126
8	3.023	410.14	0.2451	HOMO $\rightarrow$ LUMO+3	0.68986
9	3.1085	398.85	0.0008	HOMO-3 $\rightarrow$ LUMO	0.68631
10	3.198	387.69	0.0002	HOMO-4 $\rightarrow$ LUMO	0.11745
				HOMO-2 $\rightarrow$ LUMO	-0.10511
				HOMO $\rightarrow$ LUMO+4	0.66596

Table A.2: Calculated excited states for *d*-CDT($PTTh_2$)$_2$, with the energy, wavelength, oscillator strength (f), orbital transition(s) contributing to the excited state, and weighting (λ) of each orbital transition.

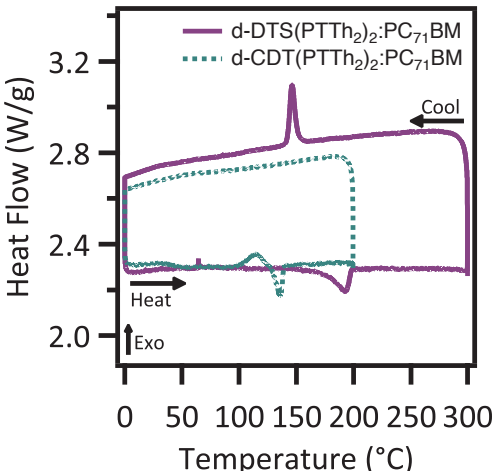

Figure A.6: DSC traces of *d*-DTS$(PTTh_2)_2$:$PC_{71}BM$ and *d*-CDT-$(PTTh_2)_2$:$PC_{71}BM$. The heating and cooling rate was 2°C/min

Crystallite correlation length for as cast samples

	(100) reflection		(010) reflection
	Out-of-plane portion (nm)	In-plane portion (nm)	In-plane portion (nm)
d-DTS($PTTh_2$)$_2$	37.7	26.1	32.1
d-DTS($PTTh_2$)$_2$:$PC_{71}BM$	26.0	21.8	27.1
d-CDT($PTTh_2$)$_2$	20.0	17.2	27.0
d-CDT($PTTh_2$)$_2$:$PC_{71}BM$	11.8	n/a	4.4*

Crystallite correlation length for annealed (80°C) samples

	(100) reflection		(010) reflection
	Out-of-plane portion (nm)	In-plane portion (nm)	In-plane portion (nm)
d-DTS($PTTh_2$)$_2$	33.3	49.2	34.9
d-DTS($PTTh_2$)$_2$:$PC_{71}BM$	22.7	24.6	39.1
d-CDT($PTTh_2$)$_2$	28.3	39.0	99.5*
d-CDT($PTTh_2$)$_2$:$PC_{71}BM$	26.3	n/a	190.0*

Table A.3: Crystallite correlation lengths for as cast and annealed (80°C) samples of *d*-DTS($PTTh_2$)$_2$, *d*-CDT-($PTTh_2$)$_2$, and their blends with $PC_{71}BM$for the (100) and (010) reflection.

d-spacings of as cast samples

	(100) reflection		$\pi - \pi$ (010) reflection
	out-of-plane *d*-spacing (nm)	in-plane *d*-spacing (nm)	in-plane *d*-spacing (nm)
d-DTS($PTTh_2$)$_2$	1.90	2.02	0.35
d-DTS($PTTh_2$)$_2$:$PC_{71}BM$	1.86	2.04	0.35
d-CDT($PTTh_2$)$_2$1.60	1.82	*hard to tell*	0.36
d-CDT($PTTh_2$)$_2$:$PC_{71}BM$	n/a	n/a	0.34

Annealed at 80° C

	(100) reflection		$\pi - \pi$ (010) reflection
	out-of-plane *d*-spacing (nm)	in-plane *d*-spacing (nm)	in-plane *d*-spacing (nm)
d-DTS($PTTh_2$)$_2$	1.91	2.07	0.35
d-DTS($PTTh_2$)$_2$:$PC_{71}BM$	1.93	2.08	0.35
d-CDT($PTTh_2$)$_2$	1.60	1.71	0.36
d-CDT($PTTh_2$)$_2$:$PC_{71}BM$	1.61	n/a	0.36

Table A.4: *d*-spacings for as cast and annealed (80°C) samples of *d*-DTS($PTTh_2$)$_2$, *d*-CDT($PTTh_2$)$_2$, and their blends with $PC_{71}BM$for the (100) and (010) reflection.

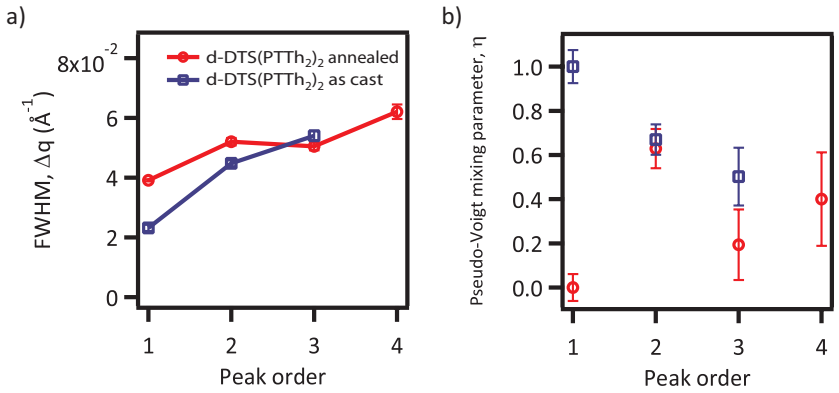

Figure A.7: Peak parameters for isolated peaks along q_z for pristine *d*-DTS-$(PTTh_2)_2$. a) Peak width, δq, as a function of peak order and b) pseudo-Voigt mixing parameter, η, as a function of peak order.

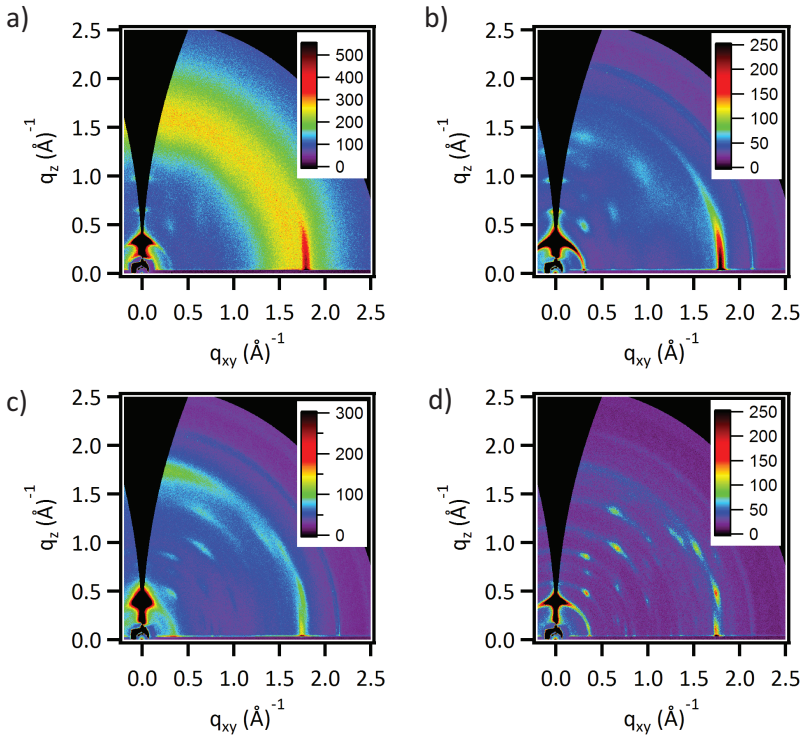

Figure A.8: Two-dimensional GIWAXS plots of a (a) *d*-DTS($PTTh_2$)$_2$ film as cast, (b) *d*-DTS($PTTh_2$)$_2$ film annealed at 80°C, (c) *d*-CDT($PTTh_2$)$_2$ film as cast and (d) *d*-CDT($PTTh_2$)$_2$ film annealed at 80°C. All samples are on glass/ITO/MoO_x substrates.

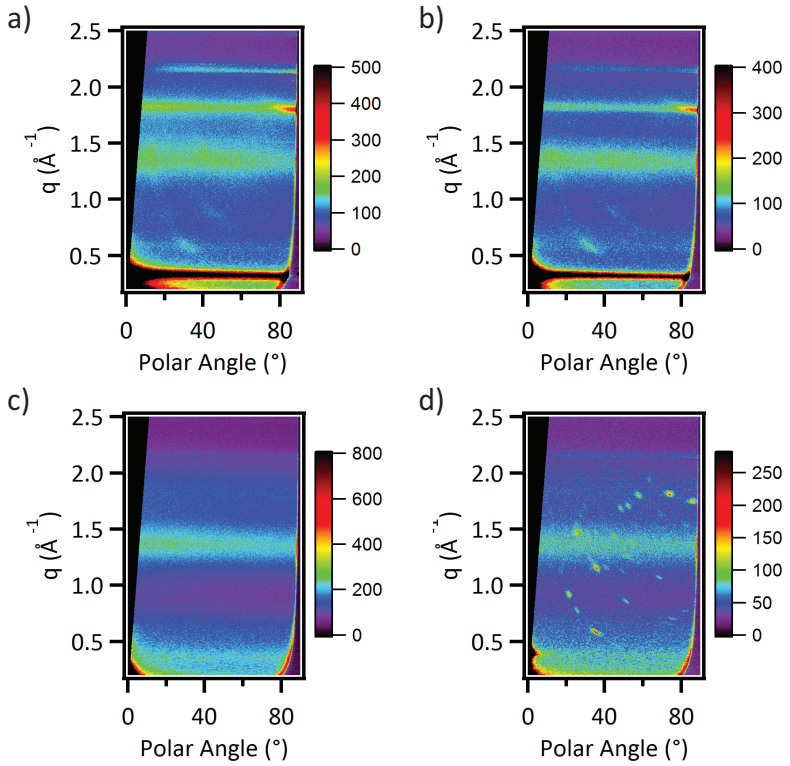

Figure A.9: GIWAXS sector plots of BHJ films of (a) *d*-DTS(PTTh$_2$)$_2$:PC$_{71}$BM, (b) *d*-DTS(PTTh$_2$)$_2$:PC$_{71}$BM annealed at 80°C, (c) *d*-CDT(PTTh$_2$)$_2$:PC$_{71}$BM, and (d) *d*-CDT(PTTh$_2$)$_2$:PC$_{71}$BM annealed at 80°C. All films were on glass/ITO/MoO$_x$ substrates.

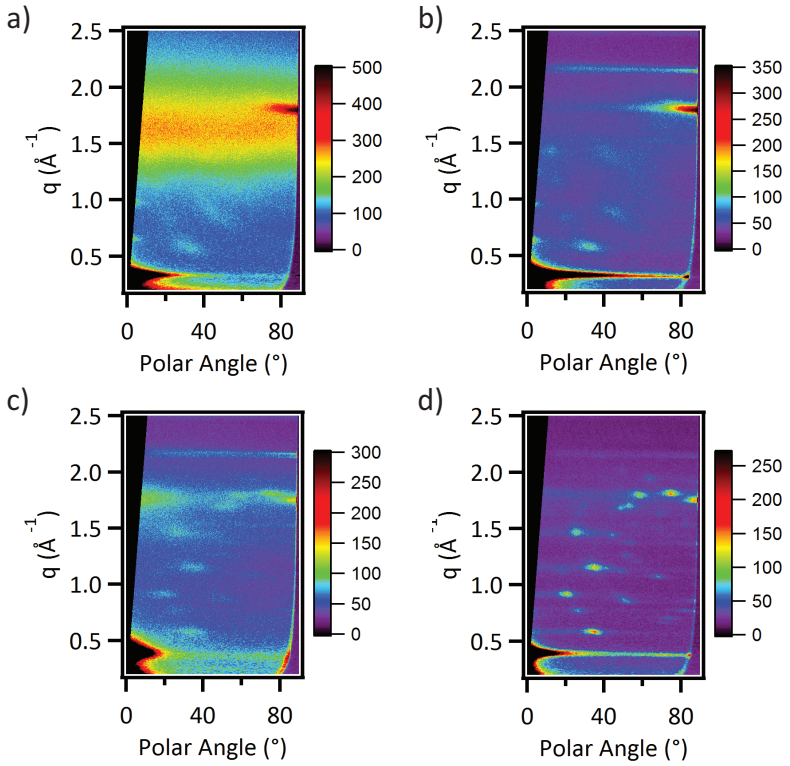

Figure A.10: GIWAXS sector plots of pristine films of (a) *d*-DTS(PTTh$_2$)$_2$, (b) *d*-DTS(PTTh$_2$)$_2$ annealed at 80°C, (c) *d*-CDT(PTTh$_2$)$_2$, and (d) *d*-CDT-(PTTh$_2$)$_2$ annealed at 80°C. All films were on glass/ITO/MoO$_x$ substrates.

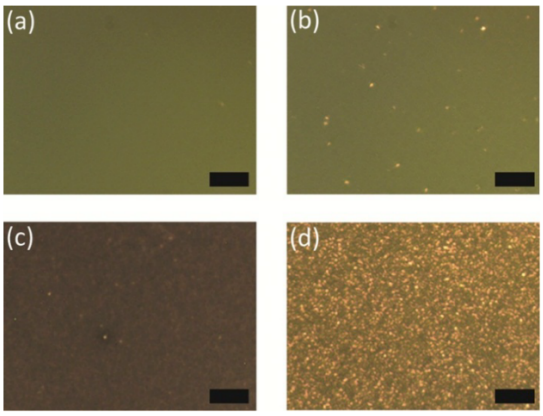

Figure A.11: Polarized optical microscope images of (a) an as cast *d*-DTS-$(PTTh_2)_2$:$PC_{71}BM$ film, (b) *d*-DTS$(PTTh_2)_2$:$PC_{71}BM$ annealed at 80°C for 10 min, (c) an as cast *d*-CDT$(PTTh_2)_2$:$PC_{71}BM$ film, and (d) a *d*-CDT-$(PTTh_2)_2$:$PC_{71}BM$ film annealed at 80°C for 10 min. All films were cast on glass/ITO/MoO_x substrates. The scale bar is 10 μm

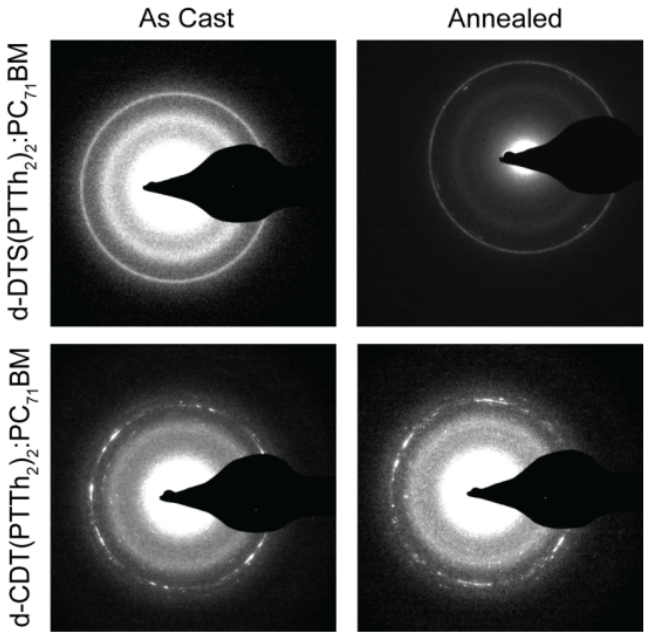

Figure A.12: Selected area electron diffraction (SAED) patterns of as cast and annealed blends of *d*-DTS$(PTTh_2)_2$:$PC_{71}BM$ and *d*-CDT$(PTTh_2)_2$:$PC_{71}BM$.

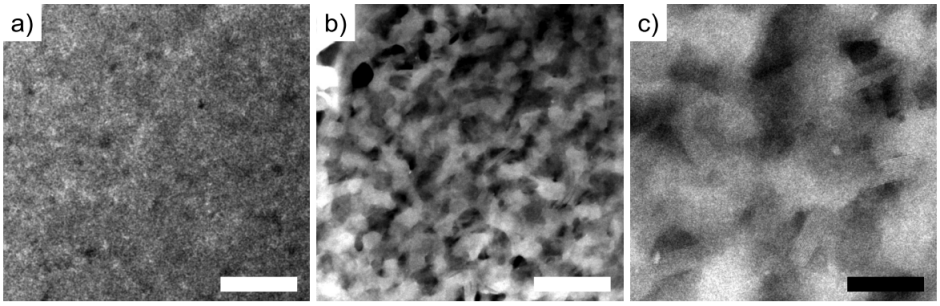

Figure A.13: STEM images of the a) as-cast and b) annealed *d*-DTS-$(PTTh_2)_2$:$PC_{71}BM$. A higher magnification view of the annealed film is shown in c). In this configuration, we are sensitive to both diffraction contrast and mass-thickness variations. The large structural changes from thermal annealing suggest surface roughening and the presence of voids and large crystals within the film. As shown in c), we are still able to observe lattice planes of q$\sim$0.31 $Å^{-1}$ from some of the larger crystals. The white (black) scale bar is 250 nm (90 nm).

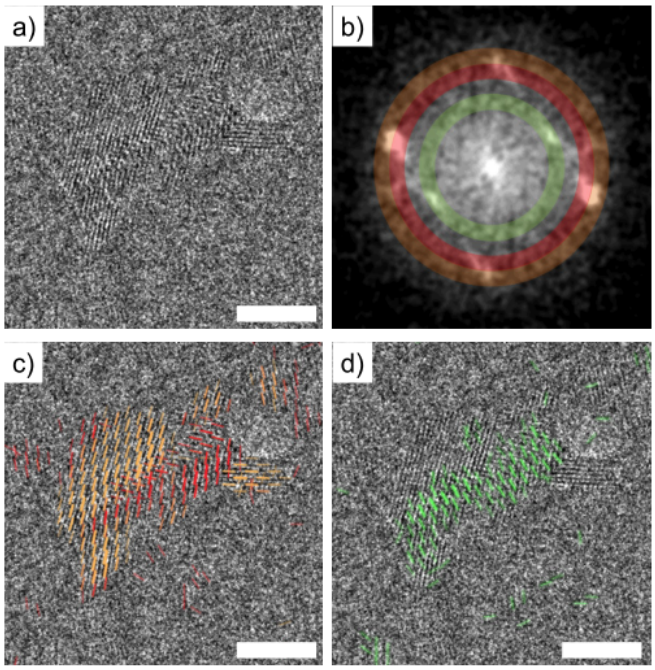

Figure A.14: HRTEM image of the as-cast *d*-CDT(PTTh$_2$)$_2$:PC$_{71}$BM BHJ film. The films appear to be highly ordered set of close lattice spacings and suggests the presence of a number of polymorphic structures. The raw image of an interesting region is shown in a). The Fourier transform of the same region is shown in b) along with colored, transparent rings centered around at q = 0.235, 0.305, and 0.360 Å^{-1} in green, red, and orange, respectively. Using these colors, lines are drawn perpendicular to the lattice planes in b) and c) giving a spatial map of the regions giving rise to the peaks observed in the Fourier transform.

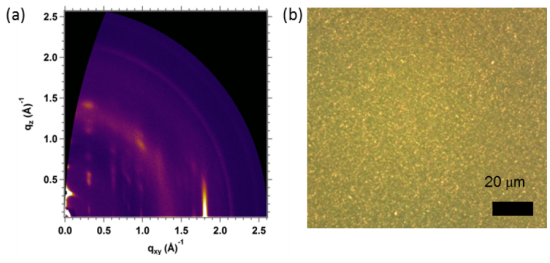

Figure A.15: (a) GIWAXS and (b) polarized optical microscope images of *d*-DTS(PTTh$_2$)$_2$:PC$_{71}$BM films annealed at 145°C.

Appendix B

Supporting Information for Chapter 6

B.1 Larger Exciton Diffusion Lengths and the Effectiveness of The Energy Cascade

In the previous sections, we simulated moderate exciton diffusion lengths (L_D = 5.6 nm). In order to confirm that energy transfer is still effective for materials with higher L_D, we simulated ECE for a representative selection of conditions described previously for L_D up to 26 nm (see Figure B.1). We conclude that even for systems with higher L_D, introducing the energy transfer cascades and roughened interfaces still leads to significantly improved ECE. Thus these remain viable strategies for improving exciton yield, even when exciton diffusion lengths are large.

A series of contour plots (Figure B.1) show the parameters for which very high ECE (> 0.9, blue regions on the plots) and moderately high ECE (> 0.7, green regions on the plots) can be achieved. Contour lines with high slopes indicate that diffusion has little effect on the ECE and is mostly due to other effects, while contour lines with low slopes indicate that improvement to ECE is strongly dependent on increasing L_D.

Without energy transfer present (Figure B.1a), the ECE for a flat interface increases with increasing L_D, but remains low overall for films thicker than $\sim$12 nm. When energy transfer is added for films with a flat interface and R_0^{DC} = 7.5 nm (Figure B.1b), the ECE is improved for all exciton diffusion lengths and thicknesses, with high ECE attainable for films up to $\sim$ 22 nm. However, the improvement due to increasing L_D is less pronounced (contour lines have a higher, nearly vertical slope) in the case with energy transfer included than the case with

only exciton diffusion. For the $D \rightarrow A \rightarrow C$ cascade with $R_0^{DA} = R_0^{AC} = 7.5$ nm (Figure B.1c), the ECE further increases, with high ECE possible for film thicknesses up to ~ 30 nm. With this scheme, the improvement due to increasing L_D, still remains small, with high-slope contour lines.

Without energy transfer present (Figure B.1d), the ECE for rough interfaces (A=d_D and L = 60 nm) increases even more with L_D than for the flat interface (the contour lines have a lower slope that approaches horizontal for thicker films) and also has overall higher ECE. Roughening the interface to A=d_D and L = 60 nm is particularly effective for all film thicknesses and exciton diffusion lengths (Figure B.1e & f, which have $R_0^{DC} = 5$ nm and $R_0^{DC} = 7.5$ nm, respectively). The energy transfer in the rough film and the increasing exciton diffusion lengths co-function to achieve very high ECE, even for 75 nm films. An L_D of 24.5 nm is required for 75 nm film to reach ECE = 0.9 when $R_0^{DC} = 5$ nm and an L_D of only 13.9 nm is required when $R_0^{DC} = 7.5$ nm. In fact ECE remains above 0.85 for all L_D and thicknesses simulated when $R_0^{DC} = 7.5$ nm. Thus we conclude that energy transfer remains a viable strategy even when exciton diffusion lengths are large.

For films thicker than 25 nm, increasing the L_D up to 26.5 nm along with using an energy transfer cascade schemes is not sufficient to achieve ECE > 0.9, although it does lead to significant improvement to the ECE. On the other hand, increasing roughness alone is also insufficient to achieve ECE > 0.9; the two strategies are needed together. Thus roughing the interface along with exciton diffusion and energy transfer would allow the solar cell to achieve large ECE.

B.2 Approximations for Exciton Collection Efficiency

B.2.1 ECE for Diffusion Only

When excitons move only by diffusion (energy self-transfer) within the donor material and do not energy transfer to the interface, we can estimate the ECE for a film of thickness L by solving the diffusion equation for the number of excitons collected after one exciton lifetime for a given starting position, then averaging over all exciton starting positions assuming a uniform distribution.

The diffusion equation for this situation is given by

$$\frac{\partial f(x,t)}{\partial t} = D\frac{\partial^2 f(x,t)}{\partial x^2} \tag{B.1}$$

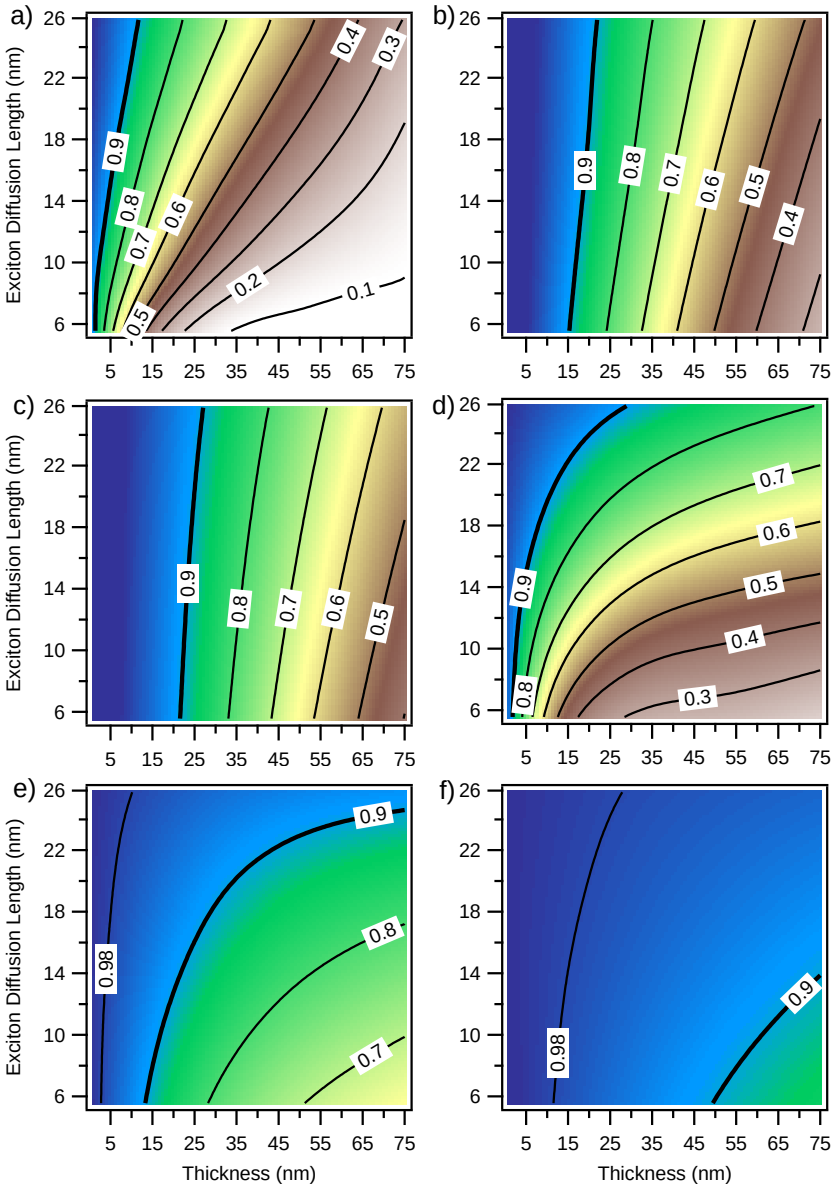

Figure B.1: Contour plots showing the exciton collection efficiency for varying exciton diffusion lengths and film thicknesses for a) flat interfaces with no energy transfer, b) flat interfaces with energy transfer to the interface with $R_0^{DC} = 7.5$ nm, c) flat interfaces with a $D \rightarrow A \rightarrow C$ energy cascade with $R_0^{DA} = R_0^{AC} = 7.5$, d), rough interfaces with no energy transfer e) rough interfaces with $R_0^{DC} = 5$ nm and A=50nm L=60nm, and f) and a rough interface with R_0^{DC} increased to 7.5.

with boundary conditions

$$\frac{\partial f(0,t)}{\partial x} = 0 \tag{B.2}$$

$$f(L,t) = 0 \tag{B.3}$$

for the edge of the film and the interface, respectively. For an exciton starting a position l in a film of thickness L, the initial position is a Dirac delta function centered at l

$$f(x,0) = \delta(x-l). \tag{B.4}$$

This partial differential equation can be solved by separation of variables using the boundary conditions, where the position-dependent part is given by $X(x) = C_n \cos(\sqrt{\lambda_n}x)$ and the time-dependent part is given by $T(t) = B_n \exp(-D\lambda_n t)$ where $\sqrt{\lambda_n} = \frac{\pi(2n+1)}{2L}$ for $n = 0, 1, 2, ...$ Then the general solution is

$$\sum_n A_n \cos(\sqrt{\lambda_n}x) \exp(-D\lambda_n t). \tag{B.5}$$

The particular solution is found using the power series solution in Eq. B.5 and comparing Fourier coefficients with the Dirac delta function.

$$f(x,0) = \delta(x-l) = \sum_n A_n \cos(\sqrt{\lambda_n}x) \tag{B.6}$$

$$\int_0^L \delta(x-l) cos(\sqrt{\lambda_m}x) = \int_0^L \sum_n A_n \cos(\sqrt{\lambda_n}x) cos(\sqrt{\lambda_m}x) dx \tag{B.7}$$

Since the cosine basis functions are orthogonal,

$$\int_0^L \sum_n A_n \cos(\sqrt{\lambda_n}x) cos(\sqrt{\lambda_m}x) dx = \begin{cases} \frac{A_n L}{2} & \text{if } m = n \\ 0 & \text{if } m \neq n \end{cases} \tag{B.8}$$

so the coefficient for the sum in Eq. B.5 is

$$A_n = \frac{2}{L} \cos(\sqrt{\lambda_n} l). \tag{B.9}$$

Integrating from 0 to L over x gives the fraction of excitons remaining and then we can integrate over l to find the average over starting position.

$$\int_0^L \int_0^L f(x,t)dxdl = \sum_n \frac{8}{\pi^2(2n+1)^2} \exp\left(\frac{-Dt}{L^2}\frac{\pi^2(2n+1)^2}{4}\right) \tag{B.10}$$

The average ECE as a function of film thickness, L, and exciton diffusion length, $L_D = \sqrt{Dt}$, is

$$ECE = 1 - \sum_n \frac{8}{\pi^2(2n+1)^2} \exp\left(\frac{-L_D^2}{L^2}\frac{\pi^2(2n+1)^2}{4}\right) \tag{B.11}$$

which can easily be approximated numerically because it converges rapidly due to the exponential.

B.2.2 ECE for Energy-Transfer Only

If we treat only the energy transfer and assume no exciton diffusion, then we can estimate the ECE using the analytical solution of energy transfer from a point to a slab.

The Förster transfer rate for point-to-point transfer is given by

$$k_F = \tau^{-1}\left(\frac{R_0}{r}\right)^6 \tag{B.12}$$

and for transfer from a point-donor to an infinite slab of acceptors is given by

$$k'_F = \left(\frac{\pi C_A R_0^6}{6\tau x^3}\right) \tag{B.13}$$

(see next section) where C_A is the concentration of acceptors in the slab and x is the distance of the donor to the near face of the slab. The exciton collection efficiency for an exciton is given by

$$ECE = \frac{k_F}{\tau^{-1} + k_F}. \tag{B.14}$$

The average exciton transfer efficiency for a slice of donors of width, w, is given by

$$ECE(w) = \frac{\int ECE dx}{\int dx} = \frac{1}{w}\int_0^w \frac{k_F}{\tau^{-1} + k_F} dx \tag{B.15}$$

so substituting Eq. B.13 into Eq. B.15 gives

$$ECE(w) = \frac{1}{w}\int_0^w \frac{A^3x^{-3}}{1+A^3x^{-3}}dx \tag{B.16}$$

where $A = \left(\frac{\pi C_A R_0^6}{6}\right)^{(1/3)}$. Thus the ECE as a function of donor layer thickness based only on energy transfer from a point to an infinite slab is:

$$\begin{aligned} ECE(w) = \frac{A}{6w}\Bigg(&2\sqrt{3}\tan^{-1}\left(\frac{1}{\sqrt{3}}\right) - 2\sqrt{3}\tan^{-1}\left(\frac{A-2w}{\sqrt{3}A}\right) \\ &+\ln(A^2-2Aw+w^2) - \ln(A^2-Aw+w^2)\Big)\,. \end{aligned} \tag{B.17}$$

Similarly for a point to a plane using the rate expression given in the next section, ECE will be

$$\begin{aligned} ECE(w) = \frac{B}{4\sqrt{2}w}\Bigg(&2\tan^{-1}\left(1+\frac{\sqrt{2}w}{B}\right) - 2\tan^{-1}\left(1-\frac{\sqrt{2}w}{B}\right) \\ &+\ln(w^2+\sqrt{2}Bw+B^2) - \ln(w^2-\sqrt{2}Bw+B^2)\Big) \end{aligned} \tag{B.18}$$

where $B = \left(\frac{\pi C_A R_0^6}{2}\right)^{(1/4)}$ and C_A is the two-dimensional concentration of acceptors on the plane.

B.3 Rates of Energy Transfer in Different Geometries

B.3.1 Rate of energy transfer from a point to a plane and a slab

The rate for transfer from a point to a point is given by

$$k_{\text{point-to-point}} = \tau^{-1}\left(\frac{R_0}{r}\right)^6 \tag{B.19}$$

Integrating over a plane, the rate becomes

$$\begin{aligned} k_{\text{point-to-plane}} &= \int_0^{2\pi} \int_0^{\infty} k_{\text{point-to-point}} R dR d\theta \\ &= C_A R_0^6 \tau^{-1} \int_0^{2\pi} \int_0^{\infty} \left(\frac{1}{(R^2 + x^2)^3} \right) R dR d\theta \end{aligned}$$

$$k_{\text{point-to-plane}} = \frac{\pi C_A R_0^6}{2x^4} \tau^{-1} \tag{B.20}$$

where C_A is the two-dimensional concentration of acceptors. For a point to a slab of thickness L the rate is calculated by

$$\begin{aligned} k_{\text{point-to-slab}} &= \int_0^{L} k_{\text{point-to-plane}} dz \\ &= \frac{\pi C'_A R_0^6}{2} \tau^{-1} \int_0^{L} \left(\frac{1}{(x+z)^4} \right) dz \\ &= \frac{\pi C'_A R_0^6}{6} \tau^{-1} \left(\frac{1}{x^3} - \frac{1}{(x+L^3)} \right) \end{aligned}$$

and for an infinite slab, $L \to \infty$ and the rate becomes

$$k_{\text{point-to-slab}} = \frac{\pi C'_A R_0^6}{6x^3} \tau^{-1} \tag{B.21}$$

where C'_A is now the three-dimensional concentration of acceptors.

B.3.2 Rate of energy transfer from a point to a plane with dipole alignment

For the case with dipole alignment, we no longer assume $\kappa^2 = 2/3$. In order to keep comparable R_0, we redefine

$$k'_{\text{point-to-point}} = \frac{3}{2} \kappa^2 \tau^{-1} \left(\frac{R_0}{r} \right)^6 \tag{B.22}$$

and κ is given by $\mu_{\mathbf{D}} \cdot \mu_{\mathbf{A}} - 3(\mu_{\mathbf{D}} \cdot \mathbf{R_{DA}})(\mu_{\mathbf{A}} \cdot \mathbf{R_{DA}})$ where $\mu_{\mathbf{D}}$ is the unit vector in the direction of the donor dipole, $\mu_{\mathbf{A}}$ is the unit vector in the direction of

the acceptor dipole, and $\mathbf{R_{DA}}$ is the unit vector pointing from the donor to the acceptor.

The formula for dot products in 3 dimensions is given by

$$\mathbf{v_1} \cdot \mathbf{v_2} = \sin\phi_1 \sin\phi_2 \cos(\theta_1 - \theta_2) + \cos\phi_1 \cos\phi_2 \tag{B.23}$$

where ϕ is the angle of the vector off of the z-axis and θ is the angle off of the x-axis.

For the case where the donor and acceptor dipoles are aligned along the normal vector from the point to the plane. Then $\phi_A = \phi_D = 0$, $\theta_A = \theta_D = 0$, ϕ_R is given by $tan^{-1}(x/R)$, and $\theta_R = \theta$. Then κ becomes $1 - 3\cos^2(\phi_R) = \frac{x-2R}{x+R}$.

Then substituting for κ and integrating over the plane gives

$$\begin{aligned}
k_{\text{point-to-plane}\parallel} &= \int_0^{2\pi} \int_0^{\infty} k_{\text{point-to-point}\parallel} R dR d\theta \\
&= 3/2 R_0^6 \tau^{-1} \int_0^{2\pi} \int_0^{\infty} \left(\frac{\left(\frac{x-2R}{x+R}\right)^2}{(R^2+x^2)^3} \right) R dR d\theta \\
&= \frac{15\pi(3\pi-8) C_A R_0^6}{32 x^4} \tau^{-1} \\
&= 2.098 \frac{C_A R_0^6}{x^4} \tau^{-1}
\end{aligned}$$

For the case where the acceptor dipoles are aligned along the normal vector from the point to the plane, but the donor dipoles are aligned parallel to the plane. Then $\phi_A = 0$, $\theta_A = 0$, $\phi_D = \pi/2$, $\theta_D = 0$, ϕ_R is given by $tan^{-1}(x/R)$, and $\theta_R = \theta$. Then κ becomes $-3\cos\phi_R \sin\phi_R \cos\theta_R = -3\frac{x}{R}\frac{1}{(x/R)^2+1}\cos\theta_R$

Then substituting for κ and integrating over the plane gives

$$\begin{aligned}
k_{\text{point-to-plane}\perp} &= \int_0^{2\pi} \int_0^{\infty} k_{\text{point-to-point}\perp} R dR d\theta \\
&= 6 R_0^6 \tau^{-1} \int_0^{2\pi} \int_0^{\infty} \left(\frac{\left(\frac{x}{R}\frac{1}{(x/R)^2+1}\cos\theta_R\right)^2}{(R^2+x^2)^3} \right) R dR d\theta \\
&= \frac{9 C_A R_0^6}{16 x^4} \tau^{-1} \\
&= 0.5625 \frac{C_A R_0^6}{x^4} \tau^{-1}
\end{aligned}$$

B.4 Förster Energy Transfer Radius for Transfer to CT-States

The Förster transfer radius for transfer from a donor polymer to the donor-PCBM charge transfer state, R_0^{D-CT}, was calculated using absorption and emission data obtained from the literature.[199,202,203] The absorption for the CT states was taken from the literature Marcus theory fits (Eq. B.24) to photothermal deflection spectroscopy and EQE data[199] and is shown along with the PL emission data for APFO3,[210] MDMO-PVV,[211,212] and P3HT[202] data in Figure B.2.

$$\sigma(E) = \frac{f}{E\sqrt{4\pi E_\lambda kT}} \exp\left(\frac{-(E_{CT} + E_\lambda - E)^2}{4E_\lambda kT}\right) \tag{B.24}$$

The extinction coefficient of these charge transfer states is unknown, but the extinction coefficient of the BP-PCBNB CT state, a small molecule donor - fullerene derivative acceptor pair, has been measured as ∼2500 L mol^{-1} cm^{-1}. Therefore we use this value to approximate the extinction coefficient for the polymer-PCBM CT states. Because of the one sixth dependence on extinction coefficient in Eq. B.24, an order of magnitude estimate for its value should be sufficient for a reasonable estimate of R_0^{D-CT}. The PL quantum yields are ∼30% for APFO3[213] and 2% for P3HT.[204] The orientation factor was set to $\kappa^2 = 2/3$ and the refractive index to $n = 1.5$. The calculated Förster transfer radii are $R_0^{APFO3-CT} = 1.9$ nm and $R_0^{P3HT-CT} = 1.1$ nm. The Förster transfer radius is largest for APFO3-PCBM CT state because the APFO3 fluorescence has the best overlap with the CT state absorbance. For P3HT (and MDMO-PPV), the CT state absorbance is actually at lower energy than the peak fluorescence, leading to a smaller spectral overlap and thus a smaller integrand in Eq. B.24. Pairing these polymers with an acceptor with a higher LUMO would likely increase the CT state energy because it is related to the HOMO$_{donor}$ and LUMO$_{acceptor}$ offset and therefore improve R_0^{D-CT}. R_0^{D-CT} can also be improved by increasing the donor fluorescence quantum yield, ϕ_D, or the CT state molar extinction coefficient (Figure B.3).

B.4.1 Effects of Dipole Alignment on Energy Transfer to CT States

In addition to the oscillator strength, quantum yield, and spectral overlap, one would need to consider the dipole alignment of the CT states relative to the dipoles of the donors in the film because the equation for the Förster radius depends on the orientational factor, κ^2, which is given by $[\mu_\mathbf{D} \cdot \mu_\mathbf{A} - 3(\mu_\mathbf{D} \cdot \mathbf{R_{DA}})(\mu_\mathbf{A} \cdot \mathbf{R_{DA}})]^2$

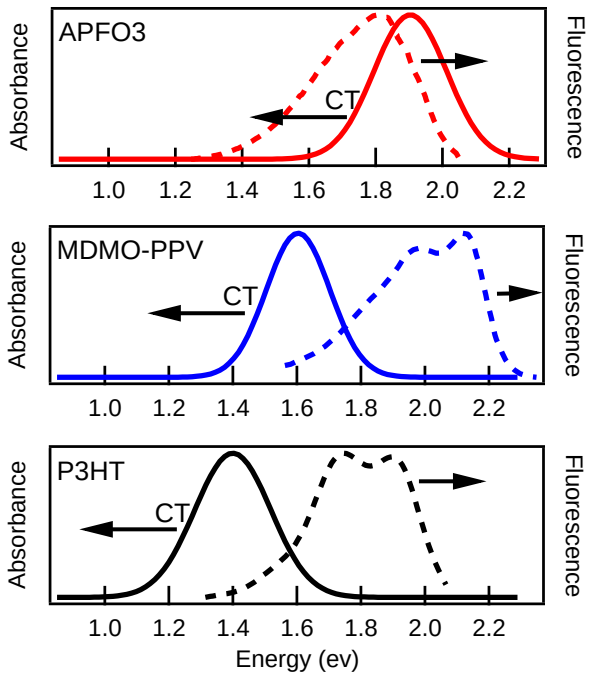

Figure B.2: The CT absorption[199] (solid) and PL emission (dashed) spectra of APFO3[210] (red), MDMO-PVV[212] (blue), and P3HT[202] (black) compiled from the literature; used for calculating the Förster transfer radius from P3HT. The charge transfer state spectra are from Eq. B.24 using that parameters given by Vandewal et al.[199]

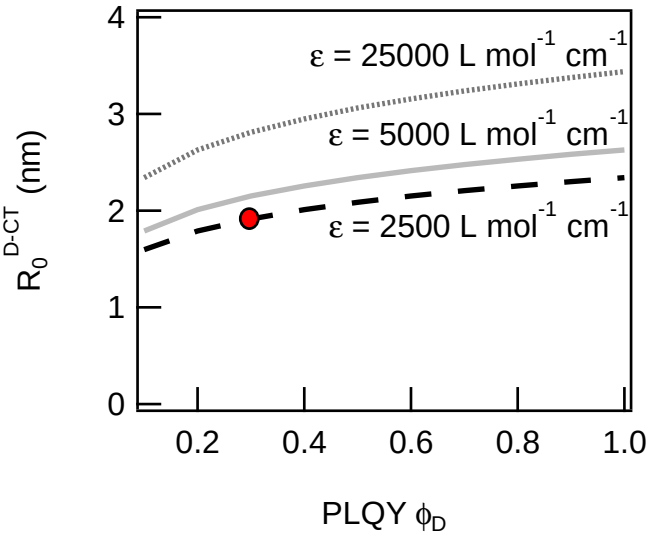

Figure B.3: The values of R_0^{D-CT} based on APFO3 as a function of fluorescence quantum yield for different molar extinction coefficients. The red circle show the actual value for APFO3/PCBM (1.9 nm).

where $\mu_{\mathbf{D}}$ is the unit vector in the direction of the donor dipole, $\mu_{\mathbf{A}}$ is the unit vector in the direction of the acceptor dipole, and $\mathbf{R_{DA}}$ is the unit vector pointing from the donor to the acceptor.[130,214] One would expect the CT state dipole to point in the direction normal to the interface (across the interface from the donor to the acceptor, Figure B.4b). The orientation of the donor dipole is dictated by the alignment of the donor relative to the interface, which can be either face-on or edge-on. For conjugated donor molecules oriented face-on to the interface, the donor dipole should be parallel to the plane of the interface (either along the short or long axis of the molecule, but pointing in the plane of conjugation) or for donor molecules oriented edge-on to the interface the donor dipole could be pointing either parallel or perpendicular to the plane of the interface. If the donor dipole is perpendicular to the interface, it will point in the same direction as the CT dipole and also along the direction from the donor to the CT state, so the value of κ^2 should be large. If it points in the plane of the interface, it will be perpendicular to the CT state dipole and the direction from the donor to the CT state so the value of κ^2 will be smaller.

For a simple estimate of how much of an effect the different dipole alignments will have on energy transfer to CT states, we calculated the rate of energy transfer for a point to a plane with the donor dipole aligned parallel and perpendicular to the plane of the interface (Figure B.4b). For the perpendicular dipoles, the rate

is

$$k_{\text{point-to-plane}\perp} = 0.563\frac{R_0^6 C_A}{x^4}\tau^{-1} \tag{B.25}$$

and for the parallel dipoles it is

$$k_{\text{point-to-plane}\parallel} = 2.098\frac{R_0^6 C_A}{x^4}\tau^{-1} \tag{B.26}$$

(see above for calculations). Both of these rates are higher than the rate for randomly rotating dipoles shown in Eq. B.20, which has an identical form to Eqs. B.25 and B.26, but has a coefficient of 1/2. This means that even for donor dipoles that are badly aligned for energy transfer to the nearest CT state (dipoles are perpendicular which means κ^2 will be zero for nearest-neighbors), the energy transfer rate averaged over the entire plane should still be higher than our simulation results predict due to our rapidly rotating dipole approximation.

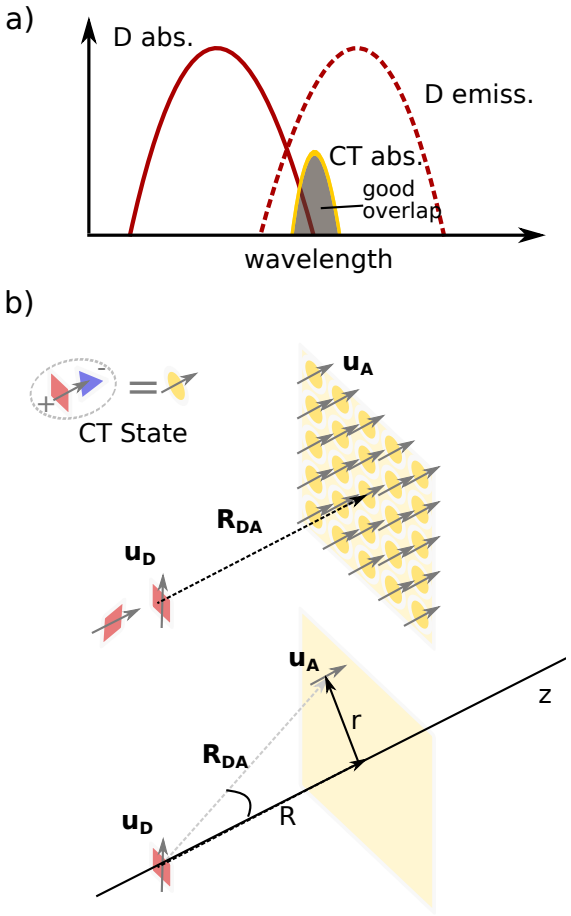

Figure B.4: a) The overlap between the donor emission and CT state absorption. The better the overlap, the larger R_0 will be. b) The possible dipole alignment of the donors and CT states. CT dipoles point from the donor to the acceptor (approximately in the direction normal to the plane). The donor dipole direction will depend on the molecular orientation, but the extremes are either aligned parallel or perpendicular to the CT dipole.